Fall 12-21-2018

Remote Sensing of Icebergs in Greenland's Fjords and Coastal Waters

Jessica Scheick
University of Maine, jbscheick@gmail.com

REMOTE SENSING OF ICEBERGS IN GREENLAND'S FJORDS AND COASTAL WATERS

By

Jessica Scheick

A.B., Bryn Mawr College, 2009

A DISSERTATION

Submitted in Partial Fulfillment of the

Requirements for the Degree of

Doctor of Philosophy

(in Earth and Climate Sciences)

The Graduate School

The University of Maine

December 2018

Advisory Committee:

Gordon Hamilton (deceased), Associate Professor in the School of Earth and Climate Sciences, Advisor

Ellyn Enderlin, Research Assistant Professor in the School of Earth and Climate Sciences, Advisor

James Fastook, Professor in Computer Science

Peter Koons, Professor in the School of Earth and Climate Sciences

Leigh Stearns, Associate Professor in the Department of Geology, University of Kansas

Huijie Xu, Professor in the School of Marine Sciences

REMOTE SENSING OF ICEBERGS IN GREENLAND'S FJORDS AND COASTAL WATERS

By Jessica Scheick

Dissertation Advisors: Drs. Gordon Hamilton and Ellyn Enderlin

An Abstract of the Dissertation Presented
in Partial Fulfillment of the Requirements for the
Degree of Doctor of Philosophy
(in Earth and Climate Sciences)
December 2018

Increases in ocean water temperature are implicated in driving recent accelerated rates of mass loss from the Greenland Ice Sheet. Icebergs provide a key tool for gaining insight into ice–ocean interactions and until recently have been relatively understudied. Here we develop several methods that exploit icebergs visible in optical satellite imagery to provide insight on the ice–ocean environment and explore how iceberg datasets can be used to examine the physics of iceberg decay and parent glacier properties. First, a semi-automated algorithm, which includes a machine learning-based cloud mask, is applied to six years (2000–2002 and 2013–2015) of the Landsat archive to derive iceberg size distributions for Disko Bay. These data show an increase in the total number of icebergs and suggest a change in the shape of the iceberg size distribution, concurrent with a shift in the dominant calving style of Sermeq Kujalleq (Jakobshavn Isbræ), their parent glacier. Second, bathymetry is qualitatively and quantitatively inferred using icebergs as drifters; regions of iceberg drifting and stranding indicate relative bathymetric lows and highs, respectively. To quantify water depth in shallow regions, iceberg draft is

inferred from iceberg freeboard under the assumption of hydrostatic equilibrium where very high-resolution stereo image pairs of icebergs are available to construct digital elevation models. Although this results in water depths with relatively large uncertainties, the method provides valuable quantitative data in regions where bathymetric observations are unavailable, improving our understanding of sill locations and the consequent ability of warm ocean waters to reach glacier termini. Third, we use the iceberg datasets derived using the previously described methods to probe the spatial patterns of iceberg size distributions. Rigorous discrimination between power law and lognormal size distributions is challenging, but our datasets corroborate the idea that as icebergs move farther from the parent glacier and the primary control on iceberg size transitions from fracture to melting, their size distribution shifts from power law to lognormal. Overall, our analysis suggests that future thorough investigations of iceberg size distributions will serve as a valuable tool to gain insights into the physics of iceberg decay and properties of the parent glacier.

REMOTE SENSING OF ICEBERGS IN GREENLAND'S FJORDS AND COASTAL WATERS

By Jessica Scheick

Dissertation Advisors: Drs. Gordon Hamilton and Ellyn Enderlin

A Lay Abstract of the Dissertation Presented
in Partial Fulfillment of the Requirements for the
Degree of Doctor of Philosophy
(in Earth and Climate Sciences)
December 2018

Keywords: icebergs, ice–ocean interactions, remote sensing, optical imagery, iceberg size distributions, cloud masking, bathymetry, digital elevation models

Icebergs form when pieces of ice break off of glaciers that end in the ocean. My research, presented here, focuses on icebergs because they provide an important link between these glaciers and the ocean. Specifically, my work develops tools that enable us to better use observations of icebergs to learn things about the ice–ocean environment. To create my datasets, I use optical satellite imagery, which is essentially photos taken by satellites. Here, I present different types of information we can get by looking at icebergs from space and discuss what this information tells us about how icebergs break up and melt. First, I develop a piece of computer code that outlines icebergs in optical satellite imagery, allowing us to determine the size and number of icebergs present in a location at the time the image was taken. A comparison between the early 2000s and mid 2010s shows the number of icebergs increased between those periods, in agreement with observations of local fishermen

who lamented increased difficulty navigating around icebergs. Second, I use icebergs to estimate water depth by calculating how much of each iceberg was below the ocean surface based on how much of the iceberg we could see above the ocean surface. Where an iceberg is stuck in one place, there is likely an underwater high point (e.g. sill), which can block warm waters located offshore from reaching the end of a glacier and causing more melting. Last, I explore the differences in iceberg sizes depending on their location and what those differences can tell us about changes in iceberg formation, breakup, and melting. Ultimately, these iceberg datasets allow us to improve our understanding of how the ocean and glaciers interact, including the influence of rising ocean temperatures on the melting of glaciers that end in the ocean and their consequent contributions to rates of sea level rise and changes in ocean circulation.

DEDICATION

This work is dedicated in fond memory to Dr. Gordon S. Hamilton, whose love for life, learning, and his field of study were infectious and readily shared and whose advice applied both in and out of a canoe:

Whatever happens, just keep your paddle in the water and keep paddling.

ACKNOWLEDGEMENTS

First and foremost, I would like to thank my advisors, Gordon Hamilton and Ellyn Enderlin. Thanks to Gordon for taking me on as a graduate student and fostering my growth as a glaciologist. Your friendship, conversation, insight, and mentorship are greatly missed. Thanks to Ellyn Enderlin for agreeing to take on the role of advisor so that I could complete my degree. I appreciate your honesty, friendship, support, and our many interesting conversations about my research.

My earning of this degree would not have been possible without the help of many others. My committee members provided helpful feedback and instruction, both one-on-one and collectively, asking difficult and insightful questions about my work. Thank you to Dr. Catherine Riihimaki for fostering my initial interests in glaciology and continuing to support my academic and personal growth. Many thanks to Dr. Jakob Abermann for his guidance, support, and ever-readiness to go for a hike or talk glaciology (or not) over a pint. I am indebted as well to the many others at the University of Maine and around the world who provided guidance, insight, and stimulating conversation and questions about ice–ocean interactions, remote sensing, data analysis, coding, and life in general.

I would be remiss to not acknowledge the many people whose friendship and support have kept me going both in and out of the University setting. My partner, Noah, who is ever ready with a kind word of encouragement. My family, for pushing me to follow my dreams and reminding me that no challenge is too big. My many communities, for providing fun and creative outlets and supportive spaces. My friends, near and far, graduate and non. Deborah, Diana, Mel, John, Lynn, Tom, Gail, Liz, Claire, Sonja, and many others – you've all helped make the [bumpy] journey to a PhD a better experience. And thank you to my fellow glaciology and remote sensing groupmates and the many UMaine graduate students and faculty with whom I have had the pleasure of interacting.

For the work presented in Chapter 2, I thank Jakob Abermann, Eva Mätzler, and the rest of Asiaq, Greenland Survey, for assisting with project development and insightful discussions on iceberg detection and icebergs along the west coast of Greenland. I also thank the many marine operators and other residents of Nuuk and Ilulissat who provided information on iceberg hazards in Disko Bay and helped shape the goals of this project. For the work presented in Chapter 3, I thank Emily Miller for all her work identifying stranded icebergs and collecting and processing imagery to derive the bathymetry estimates. I thank Carl Gladish and Josh Willis for providing bathymetry and ocean density datasets (originally collected by *Schumann et al.* (2011) and *OMG Mission* (2016a)). I also thank the OMG science team for helpful conversations and feedback in contextualizing the work. For the work presented in Chapter 4, I thank Sonja Birthisel and Andrei Kahlil for helpful discussions on statistics. I thank Ellyn Enderlin for providing iceberg datasets from *Enderlin et al.* (2016) for inclusion in my analyses in Chapters 3 and 4.

Funding for this work comes from NASA Headquarters under the NASA Earth and Space Science Fellowship Program (grant NNX15AP08H), the US National Science Foundation's IGERT Program (grant DGE-1144423, Adaptation to Abrupt Climate Change), NASA's Jet Propulsion Lab under Oceans Melting Greenland (subcontract 1578374), the Maine Space Grant Consortium, and the University of Maine Graduate Student Government. Additional travel support came from the International Arctic Science Committee, the International Glaciological Society, and Geohackweek. Satellite imagery was provided courtesy of the U.S. Geological Survey (and European Space Agency) for Landsat and Sentinel imagery and the Polar Geospatial Center (supported by NSF-OPP awards 1043681 and 1559691) for Digital Globe, Inc. WorldView imagery used to create DEMs.

TABLE OF CONTENTS

LIST OF TABLES

LIST OF FIGURES

GLOSSARY

- **draft** – *of an iceberg*, the maximum depth of the iceberg below the waterline, measured from the water–air interface to the lowest point of the submerged portion of the iceberg.
- **dynamics** – *of a glacier*, the behavior or flow properties of a glacier, including velocity and fracture.
- **freeboard** – *of an iceberg*, the maximum height of the iceberg above the water–air interface, measured from the water to the highest elevation of the subaerial portion of the iceberg.
- **length** – *of an iceberg*, the longest subaerial dimension. Ideally measured in plan view but also collected by sextant from a ship. May be approximated as the longer axis of a best fit rectangle or ellipse fitted to an iceberg outline.
- **iceberg** – mass of ice in a marine or lacustrine environment, formed when a piece of a glacier or ice shelf breaks off (calves) into a body of water.
- **marine-terminating** – ending in the ocean, for example a glacier.
- **mass balance** – the difference between ice mass accumulation (e.g. snow) and loss (e.g. melting and calving).
- **mélange** – a dense, floating matrix of calved glacier ice and sea ice.
- **outlet glacier** – a glacier draining ice from a large ice body such as an ice sheet towards the ice mass' margins, generally topographically steered through a valley. This term can be combined with marine-terminating, as in "marine-terminating outlet glacier".

- **width** – *of an iceberg*, the shorter subaerial dimension taken perpendicular to the length. Ideally measured in plan view but also collected by sextant from a ship. May be approximated as the shorter axis of a best fit rectangle or ellipse fitted to an iceberg outline.

CHAPTER 1
INTRODUCTION

1.1 Ice–ocean Interactions

Over the last two decades, the response of the Greenland Ice Sheet to climate change has become increasingly pronounced. Negative annual mass balances have dominated since before the turn of the 21st century (e.g. *Rignot and Kanagaratnam*, 2006; *Van den Broeke et al.*, 2009; *Rignot et al.*, 2011; *Enderlin et al.*, 2014); currently, up to half of the mass loss is due to surface ablation, with the remainder due to changes in ice dynamics of outlet glaciers (*Van den Broeke et al.*, 2009; *Enderlin et al.*, 2014). The majority of Greenland's outlet glaciers terminate at marine boundaries, yet our understanding of the mechanisms controlling mass loss to the ocean remains incomplete, hindering our ability to predict future climate-related impacts on the ice sheet. Several of these mechanisms operate at the ice–ocean interface, where warm ocean waters come into contact with the land-based glacier ice (*Straneo et al.*, 2010) and where the presence of dense ice mélange and icebergs makes direct observation difficult.

Recent work has begun to illuminate the details of ice–ocean interactions in coastal fjords around Greenland, including the role of feedbacks between oceanographic controls and terminus dynamics. Among the new insights are constraints on terminus position change, calving behavior, iceberg size, drift, and decay, fjord circulation, oceanic heat transport, submarine melt rates, and freshwater sources and fluxes. The improved spatial and temporal resolution of remote sensing observations of the cryosphere over the course of the last decade, in combination with the application of increasingly complex computational methods to the satellite archive, provide the means to yield novel insights into ice–ocean interactions over a broad range of temporal and spatial scales. These applications

are particularly important for investigations of the ice–ocean interface, where direct observations are limited by resources, accessibility, and ice hazards. Here, rather than viewing icebergs as an impediment to observation, we develop methodology for probing icebergs observed in satellite imagery and explore the techniques' applications to provide insight into several important mechanisms regarding ice–ocean interactions.

1.2 Fjord Water Properties and Circulation

The implication of the ocean as a driver of Greenland mass loss and as an explanatory variable for understanding the varied responses of neighboring glaciers to similar forcings drove the research community to improve our understanding of fjord circulation and the interactions between marine glacier termini and their oceanic environment. Circulation in fjords containing marine-terminating glaciers is influenced by fjord geometry and changes seasonally as well as interannually in response to shifts in the dominant driving forces. Elucidating the drivers of fjord circulation in any given fjord is thus dependent on regional oceanic water mass properties, circulation patterns, and winds, as well as local freshwater fluxes (including runoff, sub- and englacial discharge, and submarine melt) and fjord geometry. These drivers force water mass stratification and buoyancy properties that ultimately influence fjord circulation and mixing (e.g. *Mortensen et al.*, 2011; *Straneo et al.*, 2011, 2012; *Sutherland et al.*, 2014a).

Many of Greenland's fjords are stably stratified, with relatively cold, fresh polar water (PW) overlying warmer, more saline Atlantic water (AW) of subtropical origin. In the proximity of glacier termini, these water masses are modified by both melt and runoff. The altered signatures of these water masses cannot be explained by melt modification alone, suggesting that buoyancy-driven mixing occurs along the glacier terminus (*Straneo et al.*, 2012). This glacially modified water is exported

both at the surface and at depth along the polar–subtropical water interface, and its layer thickness varies seasonally (*Mortensen et al.*, 2011; *Straneo et al.*, 2011).

The combination of fjord bathymetry (which influences what coastal water masses penetrate into fjords), water properties (such as salinity and heat content), and surface and sub/englacial freshwater runoff (including its height and buoyancy relative to the ambient fjord waters) influences the evolution of glacier terminus geometry (*Chauché et al.*, 2014), as illustrated by case studies from multiple Greenlandic fjords. In Petermann Fjord (Northwest Greenland), opportunistic surveys by *Johnson et al.* (2011) demonstrated that heat availability is not the rate limiter on submarine melting. More heat is available in the fjord than is needed to produce enough melt to explain observed freshwater flux rates. The authors posit that other factors, such as the depth of the mixed and surface layers relative to the base of the floating ice tongue, are also important. *Kjeldsen et al.* (2014), working in Godthåbsfjord (West Greenland), found that large subglacial discharge events due to rapid lake drainage temporarily altered the fjord circulation patterns downstream of the terminus. Specifically, the buoyant plume of discharge transported surface and intermediate waters downstream and entrained saline, deep waters, causing a temporary decrease in temperature followed by a several day increase in salinity before both returned to near their previous conditions. At the mouth of Sermilik Fjord (Southeast Greenland), winds were observed to depress the halocline with the resulting pressure gradient leading to an influx of warm subtropical waters into the fjord (*Straneo et al.*, 2010). A similar phenomenon was observed in Kangerdlugssuaq Fjord (*Christoffersen et al.*, 2011), also in East Greenland. However, in Ilulissat Isfjord (central West Greenland), the presence of a high sill was shown to block this type of intermediary circulation from renewing fjord waters, with the authors concluding that here basin renewal is instead driven by liquid freshwater entering the fjord at the Sermeq Kujalleq (Jakobshavn Isbræ) terminus (*Gladish et al.*, 2015).

Bathymetry plays a critical role in determining the fjord water masses able to reach the glacier terminus ice–ocean interface. In Southeast Greenland, the presence of cross-shelf troughs effectively channels warm AW in the Greenland Coastal Current across the shelf and into the fjord (*Straneo et al.*, 2010; *Christoffersen et al.*, 2011). In contrast, the presence of a high sill (i.e. water shallows to <200 m depth) in Ilulissat Isfjord effectively blocks the warmest, densest AW on the West Greenland continental shelf from entering the fjord (*Holland et al.*, 2008; *Schumann et al.*, 2012; *Gladish et al.*, 2015). The presence of multiple sills (water depths from ~170–280 m) within 48 km of one another in Godthåbsfjord, in combination with strong tidal currents, drives turbulent mixing and an intermediate baroclinic circulation that potentially serves as a local heat source within the fjord (*Mortensen et al.*, 2011). Taken together, these investigations demonstrate the importance of bathymetry, tides, freshwater inputs, stratification, AW–PW and ice–water interface depths, and external forcing on driving fjord circulation (*Carroll et al.*, 2017).

1.3 Calving

Glacier calving is the mechanical loss of ice at glacier termini and is an important mechanism of mass loss for the Greenland Ice Sheet (e.g. *Van den Broeke et al.*, 2009; *Enderlin et al.*, 2014). Broadly, calving results from the breaking off of subaerial overhanging slabs formed due to melting at and below the waterline, rifts formed and/or propagated by buoyancy forces, especially at the grounding line due to tides, and hydrofracturing due to the presence of meltwater on the glacier surface (e.g. *van der Veen*, 1998; *Bassis and Jacobs*, 2013; *O'Leary and Christoffersen*, 2013; *Murray et al.*, 2015; *Benn et al.*, 2017). Around Greenland, the calved blocks of ice range in both horizontal and vertical extent from relatively small pieces (<10 m in all dimensions) to large, horizontally extensive (10s of km in length and/or width) but relatively shallow ice islands to full thickness, several km long icebergs

(e.g. *Dowdeswell et al.*, 1992; *Aström et al.*, 2014; *Münchow et al.*, 2014; *Murray et al.*, 2015).

Calving occurs when the yield stress of the ice is exceeded, resulting in complete fracture, and consequently large blocks of ice break off and are transported away from the glacier terminus (*Bassis and Jacobs*, 2013). Through simulations of glacier calving, *Bassis and Jacobs* (2013) determined that calving is a two step process dependent on both the water depth and ice thickness. For glaciers with thicknesses close to or above 1,000 m, the closer the ice is to flotation, the more unstable the terminus and the higher the likelihood of calving. Once the ice block has become detached, however, sufficient water depth is required for the iceberg to be exported. Thus, owing to the combination of terminus thickness and water depth and the resulting stress regime, floating ice tongues will tend to calve large, tabular icebergs with widths greater than ice thickness while grounded termini will calve non-tabular icebergs with widths that are some fraction of ice thickness (*Bassis and Jacobs*, 2013; *Benn et al.*, 2017).

The rate of undercutting by submarine melting relative to the calving rate exerts control on the stress field at the glacier terminus, ultimately placing constraints on the size of calved icebergs and consequently amount of mass lost. Where undercutting rates exceed calving rates, high-magnitude calving events in which the calving length is much larger than the undercut length (the multiplier effect) occur (*O'Leary and Christoffersen*, 2013; *Benn et al.*, 2017). If calving rates match undercutting rates, more frequent, low-magnitude calving events dominate and calving lengths are close to the undercut length. However, even as our ability to accurately model and predict calving rates improves, the size of the icebergs calved is often a secondary concern to correctly approximating mass loss and relative terminus position in regional models of ice sheet response to forcings (*Benn et al.*, 2007). Thus, only localized, high resolution calving models are likely to provide

insight into iceberg size distributions in Greenland's coastal waterways (*Todd et al.*, 2018).

1.4 Icebergs

As outlet glaciers have retreated, thinned, and accelerated, the flux of icebergs to Greenland's fjords and coastal waterways has increased. In addition to their importance as the byproduct of glacier calving and thus primary measure of solid mass loss, icebergs in turn interact with and influence their environment in a number of important ways. First, unlike point sources of freshwater such as meltwater streams, rivers, and subglacial conduits, icebergs represent a distributed source of freshwater to the ocean (*Silva et al.*, 2006; *Mugford and Dowdeswell*, 2010; *Enderlin et al.*, 2016; *Moon et al.*, 2018). Depending on where these drifting icebergs melt, their freshwater may play an important role in fjord stratification (*Sutherland et al.*, 2014a), overturning circulation (*Bamber et al.*, 2012), and ecosystem structure (*Greene et al.*, 2008). Second, the physical characteristics of icebergs can provide important insights into the dynamics of the glaciers that produced them (*Bassis and Jacobs*, 2013) as well as the fjords in which they drift (*Sutherland et al.*, 2014b). Further, the number and physical dimensions of icebergs in a fjord or shelf area places a constraint on their potential freshwater flux (*Sutherland et al.*, 2014b; *Enderlin et al.*, 2016), with recent analyses suggesting that time series of iceberg melting can be used to infer variations in subsurface ocean conditions and ice–ocean interactions near glacier termini (*Enderlin et al.*, 2018; *Moon et al.*, 2018). Lastly, icebergs are a hazard to marine navigation and coastal and offshore infrastructure in the Arctic, where natural resource exploration and shipping have recently expanded (*Pizzolato et al.*, 2014). Despite these myriad physical, ecological, and socioeconomic settings in which icebergs play a role, Greenland's icebergs have not been the focus of extensive prior investigations.

Until very recently, the majority of iceberg studies focused on the Southern Ocean and the large tabular icebergs originating from Antarctica's ice shelves (e.g. *Orheim*, 1980; *Gladstone et al.*, 2001; *Romanov et al.*, 2011). Investigations of icebergs in Arctic coastal waters largely focused on icebergs of potential hazard to resource development and in shipping lanes. As a result of this end goal, these studies tended to examine icebergs that had already drifted into the Labrador Sea, often as far south as Newfoundland (*Hotzel and Miller*, 1983), by which point the iceberg decay process is well underway (e.g. *Kirkham et al.*, 2017; *Wagner et al.*, 2017) and environmental factors such as the Labrador sea surface temperature – in addition to Greenland mass balance – have begun to play a driving role in the number of icebergs observed (*Bigg et al.*, 2014). Only a limited number of studies have investigated icebergs in Arctic coastal waters close enough to their sources to examine the relationships between observed iceberg size distributions and their dependence on the timing of observations relative to calving events, iceberg location within a fjord, properties of the parent glacier (such as catchment size and flow speed), and fjord geometry (*Dowdeswell and Forsberg*, 1992; *Dowdeswell et al.*, 1992; *Bassis and Jacobs*, 2013; *Kirkham et al.*, 2017; *Sulak et al.*, 2017). The research presented herein expands upon this work, investigating icebergs from the time of calving until their entry into the open ocean.

1.4.1 Iceberg Geometries

The unique and complicated shapes of icebergs makes three dimensional descriptions of their shape and size non-trivial. However, icebergs are often described using a limited number of geometric parameters – with an emphasis on those that can be observed subaerially – which are useful for making broader observations about the size distributions of icebergs and how these change through space and time. For the purposes of our discussion, we consider several geometric

parameters for each iceberg, as illustrated in Figure 1.1. Historically, length was often measured as the longest waterline dimension because of the relative ease with which one could measure it from a ship using a sextant. Where observations are made from above, the literature provides little description for how iceberg dimensions are determined.

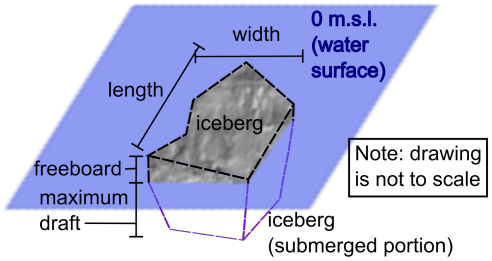

Figure 1.1: Conceptual iceberg diagram illustrating geographic parameters used to describe icebergs

Several options are available for computing iceberg dimensions, depending in part on what information is available. Iceberg plan-view geometry can be approximated as a best fit ellipse or rectangle, with length and width measured perpendicular to one another and length $\geq$ width. Where only the iceberg plan-view area is known (i.e. no outline is available), a circle or square is used to approximate length (=width). An exploration of the impacts of using these slightly different representations of iceberg shape is discussed in Section 4.2. The submarine length and width may be markedly different from the subaerial dimensions due to the presence of skirted geometries and differential rates of decay. However, these dimensions are difficult to measure without sonar and are thus not considered in more detail here.

In the vertical dimension, three related parameters are often described with different terminology. Iceberg height generally refers to the iceberg freeboard, or maximum height above the waterline. Iceberg draft or keel depth refers to the vertical distance between the waterline and the maximum iceberg depth. Here we

use the terms iceberg freeboard and draft, rather than height or keel depth. Iceberg thickness is the sum of iceberg freeboard and draft, though the point of maximum freeboard may not be vertically aligned with the maximum draft.

1.4.2 Iceberg Proportionality

The size and shape of an iceberg depends on its source and state of decay (i.e. age) as well as the physical environment within which it drifts. Immediately subsequent to calving, iceberg shape depends primarily on the ice thickness and strength of the parent glacier and the extent to which the terminus is grounded (*Benn et al.*, 2017). In order to not roll, an iceberg must have a large enough width relative to its draft that it is buoyantly stable and not prone to spontaneous capsize (*Burton et al.*, 2012; *Wagner et al.*, 2017). Iceberg draft is exceedingly difficult to measure for more than a few icebergs, particularly in a short amount of time; even with ship mounted sonar the underside of an iceberg usually cannot be imaged with a high degree of accuracy (*McGuire et al.*, 2016). Thus, relating iceberg geometric parameters has been explored for many decades, with an emphasis on means to infer iceberg draft based on subaerial geometry and thereby establish the potential damage an iceberg could cause to infrastructure and cables buried within or resting on the ocean floor. By the early 1980s, several studies had explored means for deriving the maximum draft of an iceberg. *El-Tahan and El-Tahan* (1982) summarized these investigations, noting that in some cases researchers were unable to establish clear relationships between iceberg draft and width, mass, or freeboard, while others provided evidence for generalizations that held true. Their work confirmed that draft–freeboard ratios depend on iceberg shape, with domed and tabular icebergs generally having larger ratios than pinnacled and drydock icebergs, an unsurprising result given the differences in mass distribution between these shapes. Notably, *El-Tahan and El-Tahan* (1982) establish a set of relationships from

their own and others' work in order to establish the draft minimum, maximum, and likely value based on several, rather than just one, subaerial dimensions and a series of curves fitted for each iceberg shape type. Specifically, the maximum draft is taken to be the smallest value of: 1) 10.5∗freeboard; 2) length; 3) 1.5∗width; 4) 230 m (*El-Tahan and Davis*, 1982 in *El-Tahan and El-Tahan*, 1982, for icebergs in Disko Bay); 5) the upper limit of the mass–draft plot (though the authors do not clearly present their means for computing iceberg mass). *Hotzel and Miller* (1983) compute iceberg draft as $3.781 * \text{length}^{0.63}$, a relationship derived from a dataset of measured areas and inferred drafts collected by the International Ice Patrol (IIP) on the Grand Banks, where length is taken to be twice the radius of a characteristic circle describing the iceberg area. A more recent investigation by *Enderlin et al.* (2016) similarly relates the width and thickness of icebergs. Therein, width is also taken as twice the radius of a characteristic circle with an area equivalent to that of the iceberg polygon outlined in high-resolution satellite imagery. Thickness, however, is computed based on freeboards extracted from digital elevation models (DEMs) of each iceberg and the assumption of hydrostatic equilibrium (this method is described in more detail in Chapter 3). They find, in agreement with earlier investigations, that the thickness–width relationship depends on iceberg shape, and thus varies regionally. For Ilulissat Isfjord (Sermilik Fjord), width is 2.03(1.93)∗thickness, or 2.31(2.20)∗draft. An investigation of iceberg properties by *Sulak et al.* (2017) illustrates the influence of assumptions about the submarine iceberg shape on volume, draft, and length–draft ratio (their Table 2). For example, for icebergs within Sermilik (Rink) Fjords, the length–draft ratio means were 1.48 (1.51) for a block-shaped iceberg and 0.71 (0.71) for cone shaped icebergs.

1.5 Remote Sensing of the Cryosphere

The value of *in situ* observations of the cryosphere cannot be overstated. Direct observations are crucial for providing high temporal and spatial resolution datasets that allow us to generate an intimate understanding of the dynamics of an environment. However, particularly in the polar regions, these observations are quite time and resource intensive – and sometimes too dangerous – to collect. Additionally, the uniqueness of each glacier and fjord requires a broader set of observations in order to effectively apply the conceptual models built from higher resolution observations. Remote sensing thus fills a critical gap in enabling longer term investigations of the cryosphere and earth systems in general. The broad umbrella of "remote sensing" includes information collected by some type of sensor installed on any remotely located platform. Sensors can be active (i.e. emitting and recording a signal) or passive (i.e. only recording a signal) and may record sound, light (including and beyond the visible spectrum), and/or vibrations. Sensor platforms include satellites, airplanes, ships, drones, and sleds. Here, we refer specifically to satellite remote sensing and focus almost exclusively on the use of data collected by optical sensors installed on those satellites.

Imagery from optical sensors has long played an important role in glaciology. Optical imagery has been used to investigate numerous components of the crysophere at a spatial scale that would not be possible with only ground based measurements (*Bindschadler*, 1998; *König et al.*, 2001). Imagery from optical sensors has been used to determine glacier and ice sheet velocity, identify glacier terminus position, determine snow and glacier locations and extent, develop global glacier ice inventories (e.g. Global Land Ice Measurements from Space; GLIMS), locate and infer the depth of surface melt ponds, infer subglacial discharge in plumes, and track the changes of these parameters through time (e.g. *Scambos et al.*, 1992; *Krimmel and Meier*, 1975; *Dozier*, 1989; *Raup et al.*, 2000; *Sneed and*

Hamilton, 2007; *Chu et al.*, 2009, respectively). From some of the earliest images returned in the 1970s by the Multispectral Scanner (MSS) on board the Landsat 1 satellite (originally called the Earth Resources Technology Satellite, or ERTS), with a pixel resolution of 80 m and repeat time of 18 days, there are now platforms capable of delivering imagery with sub-meter pixel resolution and repeat intervals of, on average, 3–5 days. However, despite all of the recent advances in technology that provide such high spatial resolution and improve temporal data availability, one of the biggest strengths of the optical satellite record – particularly the Landsat suite of sensors – lies in its rich archive spanning a period of unprecedented changes across Greenland. Since the 1990s, the Greenland Ice Sheet has undergone a number of massive changes that include the thinning, acceleration, and retreat of many glacier termini, including the loss of many of the ice sheet's floating ice tongues (e.g. *Joughin et al.*, 2004; *Moon and Joughin*, 2008; *McFadden et al.*, 2011), as well as an increase in the development of melt ponds and channels on the surface of the ice sheet (e.g. *Echelmeyer et al.*, 1991). Optical imagery going back to the 1980s has been crucial in allowing the cryospheric community to be aware of and track many of these changes.

Despite the myriad and important uses for optical satellite imagery described, optical sensors suffer from some important limitations, particularly for work in the Arctic. Since optical sensors are passive, they rely on energy output from the sun and reflected off the earth's surface for the collection of imagery. Thus, during winter, data is unavailable for the polar regions, limiting analyses to the summer season. Second, the sensors detect whatever the light is first reflected off of; clouds are highly reflective and common in the Arctic, often obscuring part or all of the land surface below, limiting the temporal resolution and spatial coverage of useable data. Further, clouds are difficult to distinguish from the underlying snow and ice, which share similar spectral properties. Many of these limitations pose particular

challenges to the development of automated methods, as demonstrated and discussed in Chapter 2.

The individual satellite datasets used in this research, as well as their strengths and weaknesses relative to each application, are described briefly within the chapter in which they are used. The work described herein focuses primarily on datasets derived using imagery collected by the sensors on board the Landsat and WorldView satellite platforms, although some data from Sentinel-2 are also referenced. Landsat imagery was selected as a primary resource because of its extensive temporal archive dating back to 1972 and its relatively high spatial resolution (30–120 m for most bands, with a 15 m panchromatic band since 1999) and around sixteen day repeat interval. The WorldView satellites carry multiple sensors which are capable of collecting stereo image pairs. These image pairs were used to construct DEMs, thereby providing the third dimension. However, the combination of datasets from multiple platforms was key for the tracking of icebergs described in Chapter 3.

1.6 Dissertation Objectives

The overarching aim of this work is to improve our understanding of ice–ocean interactions in Greenland's fjords and coastal waters using spaceborne observations of icebergs. This dissertation focuses on three main objectives:

- Quantify the size and distribution characteristics of icebergs in Disko Bay over the last ~20 years using the Landsat archive of optical satellite imagery.
- Infer bathymetry of Greenland's major glacial fjords based on iceberg freeboards (and hence drafts) extracted from DEMs derived from very high-resolution stereo satellite images.
- Gain insight into the physics of iceberg decay through an investigation of the spatial patterns of iceberg size distributions from calving front to open ocean.

To accomplish these objectives, two major methods development projects were undertaken, including their validation and application. Specifically, new remote sensing-based methodologies were developed to delineate icebergs and infer relative and actual fjord bathymetry. Then, temporal and spatial analyses of the datasets derived using these methods were conducted to investigate the changes in iceberg size distribution through time and with increasing distance from the parent glacier.

1.7 Outline of Chapters

Chapters 1 and 5 are the introduction and conclusion, respectively, of this dissertation. Chapters 2 and 3 were written to be standalone manuscripts and are currently in various stages of preparation, submission, and peer review. Chapter 4 provides supplementary material for the prior two chapters and explores potential limitations of and future applications for the datasets derived using these new methods.

1.7.1 Chapter 2

Icebergs provide a critical link between marine glacier termini and the ocean, yet our understanding of their size and spatial distribution remains limited temporally and spatially. Here we present a semi-automated computer algorithm that delineates icebergs in optical imagery from the Landsat suite of sensors, including a step that eliminates clouds, thereby increasing our temporal resolution by enabling the use of cloudy images. The algorithm is applied to six years (2000–2002 and 2013–2015) of the Landsat archive for Disko Bay, West Greenland. Iceberg size distributions changed markedly between the two periods, showing an increase in the total number of icebergs – particularly icebergs less than 1,800 m^2 in planar area – concurrent with the loss of the floating ice tongue and consequent changes in calving style of the iceberg parent glacier, Sermeq Kujalleq. A slightly

modified version of this chapter is currently in review in a peer-reviewed journal, with portions of Chapter 4 included as supplementary material.

1.7.2 Chapter 3

Bathymetry exerts a crucial control on the ability of warm ocean water masses to reach marine glacier termini. However, collecting bathymetry measurements is time and resource intensive, limiting our ability to improve bathymetry maps in new regions or where glacier retreat has exposed previously unmapped portions of the bed. As a result, the presence or absence of bathymetric high points (e.g. sills) and the water depths in these locations remains unknown. This hinders our ability to model the future impacts of a warming ocean on the Greenland Ice Sheet mass balance. Here we develop a remote sensing approach to qualitatively infer fjord bathymetry and quantify water depths in shallow regions using DEMs of icebergs. We compare the quantitative water depth estimates to measured bathymetry to validate the method. A slightly modified version of this chapter is currently in review in a peer-reviewed journal.

1.7.3 Chapter 4

Icebergs decay through a variety of melt and mechanical processes. The rate and relative importance of these decay mechanisms in turn influences the iceberg's geometry and the range of geometries (i.e. iceberg size distribution) present within a specified geographical area. Here we assess the impacts of our assumptions about iceberg geometry on the data presented in Chapter 3 and investigate changes in iceberg size distributions with increasing distance from their source. To do this, we combine the datasets derived in previous chapters for icebergs calved from Sermeq Kujalleq and divide the data spatially into bins of increasing distance from the calving front before determining the best statistical model to explain the shape of the data and explore its relationship to the physical processes of iceberg decay.

1.7.4 Chapter 5

This section concludes the dissertation, drawing together the ideas presented. Future avenues for research that build on the data, methods, and analysis presented here are also discussed.

CHAPTER 2
SEMI-AUTOMATED ICEBERG DETECTION

2.1 Introduction

Over the last two decades, as Greenland's marine-terminating outlet glaciers have retreated, thinned, and accelerated, the flux of icebergs to Greenland's fjords and coastal waterways has increased. Until recently, these icebergs remained a relatively little studied phenomena despite their physical, ecological, and socioeconomic importance.

Arguably the most important location to study icebergs around Greenland is along the central west coast (Figure 2.1). As these icebergs transit through the Labrador Sea into the shipping lanes of the North Atlantic (e.g. *Bigg et al.*, 1997), their meltwater has the potential to disrupt the formation of North Atlantic Deep Water (NADW) (*Fichefet et al.*, 2003). Icebergs in Disko Bay are primarily sourced from Sermeq Kujalleq (Jakobshavn Isbræ), which is the most prolific producer of icebergs in Greenland (*Enderlin et al.*, 2014). Icebergs calve into the deep Ilulissat (Jakobshavn) Isfjord and traverse the ~60 km long fjord until it empties into Disko Bay. At the mouth of the fjord, a large bedrock sill shallows the water from close to 800 m in the fjord to about 200 m at the entrance to the bay (*Schumann et al.*, 2012; *Gladish et al.*, 2015), creating a chokepoint where large (>200 m deep) icebergs become stranded. As such, the sill acts as an iceberg filter, restricting the size and number of icebergs entering Disko Bay.

North of the fjord mouth, along the eastern shore of the bay, sits the town of Ilulissat. Residents here depend heavily on fishing and tourism, so navigability of Disko Bay's iceberg laden waters is of critical importance to their livelihoods. Anecdotal evidence suggests that the number and size distribution of icebergs present in Disko Bay has changed in recent decades as Sermeq Kujalleq has thinned

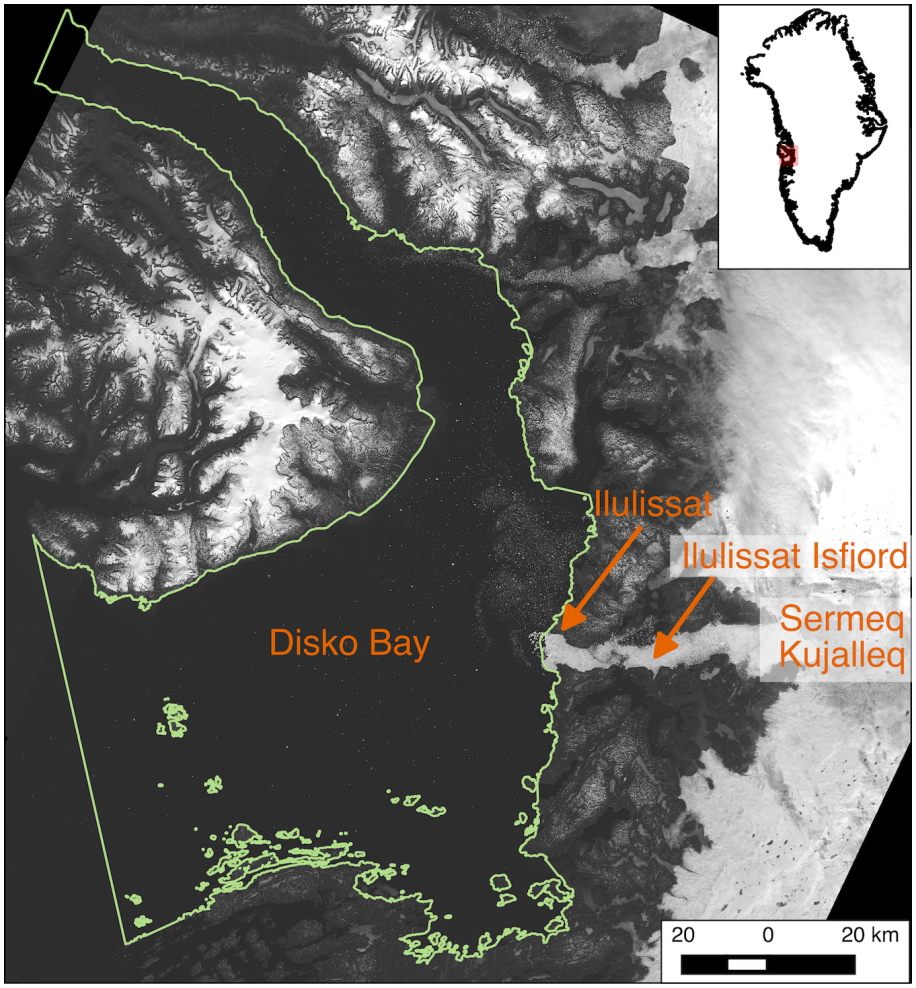

Figure 2.1: Location of Disko Bay, the study region, in West Greenland. Features of note include Sermeq Kujalleq (i.e. the iceberg source), Ilulissat Isfjord, the town of Ilulissat, and the study region of interest (ROI, green outline). Background is a mosaic of Landsat 8 panchromatic images from summer 2015.

and retreated. Specifically, marine navigators and fishermen noted that in more recent years, relative to the turn of the century, the bay is frequently covered with a large number of small icebergs, making navigation and fishing difficult. However, to date there is no comprehensive analysis of temporal variations in iceberg size distributions in Disko Bay or elsewhere around Greenland. A primary reason for the dearth of iceberg size distribution data is that at any given point in time there may be tens of thousands of icebergs in a fjord or bay (*Enderlin et al.*, 2016). This large number of icebergs, combined with limitations imposed by the resolution of satellite

imagery, pose a challenge to manual iceberg identification using satellite images. Iceberg detection and size characterization is further hindered by the presence of clouds in visible to near infrared satellite imagery. Excluding images with partial cloud cover would considerably limit the temporal resolution of any derived dataset, resulting in potential aliasing of changes in iceberg size distributions over time. Therefore, efficient mapping of icebergs mandates that clouds are automatically distinguished from snow and ice in satellite images (i.e. automated cloud masking).

The primary challenge in mapping clouds in satellite images is that clouds and snow/ice share similar spectral properties, including a large portion of the electromagnetic spectrum that is typically sensed by satellite platforms. Clouds and snow/ice are especially similar in the visible wavelengths (highly reflective) and thermal wavelengths (cold), properties that often allow clouds to be readily distinguished from relatively warm and dark-colored land surfaces. A number of different cloud detection schemes exist, including a few designed specifically for the Landsat sensors (e.g. *Irish et al.*, 2006; *Oreopoulos et al.*, 2011; *Kustiyo et al.*, 2012; *Zhu and Woodcock*, 2012; *Foga et al.*, 2017). Common approaches for detecting clouds in optical imagery include band thresholding, both of individual bands and combinations of bands, in order to exploit differences in the spectral properties of the different media (e.g. *Racoviteanu et al.*, 2009). Often, several thresholding approaches are combined and/or advanced computing and image analysis techniques are utilized to achieve the best results (e.g. *Hall et al.*, 1995; *Riggs and Hall*, 2002; *Scaramuzza et al.*, 2012; *Zhu and Woodcock*, 2012). However, the existing cloud masking approaches often fail to accurately differentiate clouds from ice and snow surfaces (*Oreopoulos et al.*, 2011; *Foga et al.*, 2017), including or excluding both clouds and snow/ice simultaneously. *Dozier* (1989), *Riggs and Hall* (2002), *Irish et al.* (2006), *Jedlovec* (2009), and many others provide insight on various approaches to generating cloud masks for optical satellite images, including

advanced image analysis techniques based on machine learning (*Lee et al.*, 1990; *Scaramuzza et al.*, 2012; *Hughes and Hayes*, 2014) and edge detection (*Zhu and Woodcock*, 2012).

To address the need for an iceberg dataset that captures changes in iceberg size distributions over time, we developed a Landsat-based semi-automated iceberg delineation algorithm that incorporates a machine learning-based cloud mask. Here we present details of the algorithm and results from Disko Bay, West Greenland, to demonstrate the utility of the algorithm to explore temporal changes in iceberg size distributions commensurate with glacier change. Because icebergs pose a considerable hazard for marine navigation, the method we present in Section 2.2 was developed so that it can be implemented locally on a standard computer and in near real-time, subsequent to the one-time development of appropriate regional input files. We evaluate our algorithm's performance by means of qualitative and quantitative analyses of data from Disko Bay and Kangerlussuup Sermia Fjord; specifically, the cloud mask is validated through manual analysis and evaluation of model output confusion matrices for Disko Bay, and iceberg detection is validated using an independent application in Kangerlussuup Sermia Fjord (Sections 2.3.1–2.3.2). Finally, we compare changes in iceberg size distributions between the 2000–2002 and 2013–2015 time periods to explore the use of iceberg size distribution time series as a means to infer changes in glacier dynamics (Section 2.4).

2.2 Methods

2.2.1 Location Selection

Due to the large number of icebergs present in Disko Bay (Figure 2.1), the pronounced changes in iceberg calving style and volume from the primary iceberg source (Sermeq Kujalleq) (e.g. *Amundson et al.*, 2008; *Joughin et al.*, 2008; *Cassotto et al.*, 2015, and references therein), and the importance of icebergs to the local

communities, we identified a pressing need for an easy to implement semi-automated approach to delineate icebergs in both cloud-free and partially cloud-covered Landsat imagery of this region. Automated optical approaches, such as that used below, rely on the contrast between bright iceberg surfaces and the comparatively dark water surrounding them. Thus, they are unable to distinguish individual icebergs that are tightly packed. To avoid problems associated with automated detection of icebergs surrounded by sea/brash ice or dammed by icebergs stranded on the sill at the mouth of Ilulissat Isfjord, we focused our study on the area seaward of the sill. The exclusion of the fjord mouth enabled us to avoid detections of erroneously large "icebergs" that were actually a combination of multiple icebergs stranded close together.

2.2.2 Imagery Selection

Changes in the style, and likely size and volume, of icebergs calved from Sermeq Kujalleq initiated in the late 1990s and continued throughout the 2000s as the glacier's terminus retreated and its geometry evolved (*Amundson et al.*, 2008; *Joughin et al.*, 2008). In order to capture these changes and test the utility of iceberg size distribution time series for quantifying dynamic change, we focused our method development and application on Landsat images. The MODIS constellation also covers our time period of interest, but it has relatively coarse spatial resolution (minimum 250 m for MODIS versus 15 m for Landsat), thereby limiting the minimum size of icebergs we could possibly detect (minimum area of 225 m^2 for Landsat versus 62,500 m^2 for MODIS). Radar datasets that cover our time period of interest are limited, and those that are available suffer from the same spatial resolution limitations as MODIS. Given our interest in changing iceberg size distributions and the relatively small iceberg sizes found in lulissat Isfjord (*Enderlin et al.*, 2016), we considered only the Landsat suite of sensors and focused on the

derivation of a semi-automated algorithm that works across the archive. The results presented herein were derived from the ETM+, OLI, and TIRS sensors; images from 2000–2002 were collected by Landsat 7 (ETM+) while images from 2013–2015 were collected by Landsat 8 (OLI and TIRS). Both Landsat 7 and 8 have a panchromatic band with a spatial resolution of 15 m, visible through short-wave infrared (SWIR) bands at 30 m spatial resolution, and thermal bands with 60–100 m (Landsat 7 and 8, respectively) spatial resolution. For processing steps that simultaneously utilized multiple bands of different native resolutions, such as in the cloud masking step, scenes were upsampled to the highest resolution of any of the input bands. For example, the cloud mask was generated at 30 m pixel resolution, then each mask pixel was parsed into four 15 m by 15 m pixels that each have the same value as the parent pixel. The potential impacts of this resampling are discussed below.

Pre-collection Landsat scenes were downloaded from the USGS EarthExplorer website (earthexplorer.usgs.gov). We used Landsat scenes spanning path numbers 10–11 and row numbers 11–12 because they provided the most complete coverage of Disko Bay. Mosaicking of multiple scenes collected during the same pass maximized coverage. The relatively high latitude of Disko Bay (~68.5–70° North) provided the advantage of a satellite repeat interval better than the 16 day standard repeat time for Landsat with the concurrent disadvantage of limiting our analysis seasonally. To minimize inclusion of springtime scenes that contained extensive sea ice (*Cassotto et al.*, 2015), even during periods of sufficient solar illumination (February–October), we used only scenes with collection dates from May to October. Based on these parameters, the number of image acquisition dates per year ranged from 11–12 for Landsat 7 (2000–2002 period) and 16–24 for Landsat 8 (2013–2015 period). Although we developed a cloud masking procedure to enable the use of Landsat scenes containing partial cloud cover, the generation of the cloud mask takes ~5 minutes compared to the 30–60 seconds it takes to visually inspect

each scene and exclude it from download. Thus, we manually screened scenes to exclude those with such extensive cloud or sea ice cover that icebergs could not easily be distinguished. We opted for manual screening rather than relying on the automatically generated percent cloud cover included in the Landsat metadata and available as a filter criterion because it applies to the entire scene, which includes both land and marine environments that frequently have different cloud conditions. Approximately 70% of the available images contained manually-identifiable icebergs, providing 9–14 (median 10) usable image swaths for a given year.

2.2.3 Algorithm

A schematic of the procedure to detect icebergs in both cloud-free and partially cloudy Landsat scenes is shown in Figure 2.2 and described in detail below.

2.2.3.1 Cloud Masking

In order to accurately map icebergs, clouds must first be masked out of the Landsat scenes. We tested ratio- and machine learning-based cloud masking techniques, as described in the following paragraphs, ultimately deriving a computationally simple, machine learning-based approach. Example applications of each method to an August 2013 Landsat scene (Figure 2.3a) are shown in panels b–e of Figure 2.3.

We tested a number of band ratio and other threshold-based approaches to automatically discriminate snow/ice from clouds. Here we present only the most common approaches for the sake of brevity since none of the ratio-based methods were used in the final algorithm. These examples capture the essence of the challenge in differentiating icebergs and clouds in optical satellite imagery, illustrating the problems encountered with all tested threshold-based methods.

Cloud identification is often accomplished by thresholding of normalized indices, ratios, and/or reflectance values that exploit the high reflectivity of clouds in certain

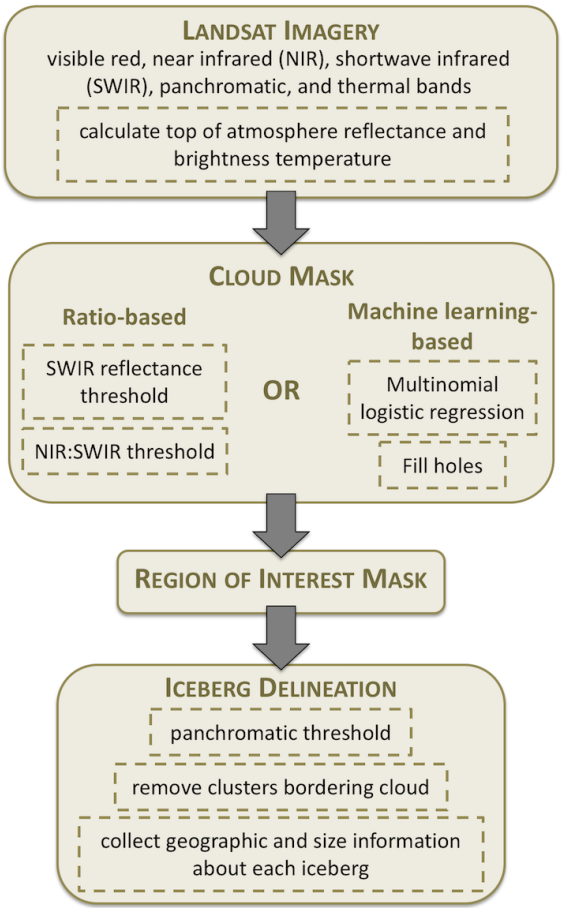

Figure 2.2: Schematic illustration of the steps of the semi-automated iceberg delineation algorithm.

wavelengths of the electromagnetic spectrum. One approach is to identify clouds simply by applying a threshold to reflectance values in the SWIR part of the spectrum (centered at roughly 1.6 µm) (e.g. *Warren*, 1982; *Dozier*, 1989; *Riggs and Hall*, 2002). Another approach uses a ratio of the visible red and SWIR bands (wavelengths centered at roughly 0.66 and 1.6 µm, respectively) (*Racoviteanu et al.*, 2009). In an effort to further exploit the spectral differences between clouds and snow/ice in these two bands, we computed a normalized index of the two bands (red–SWIR normalized index) (Figure 2.3b). We also tested a ratio of the near-infrared (NIR) to SWIR bands (centered at roughly 0.8 and 1.6 µm,

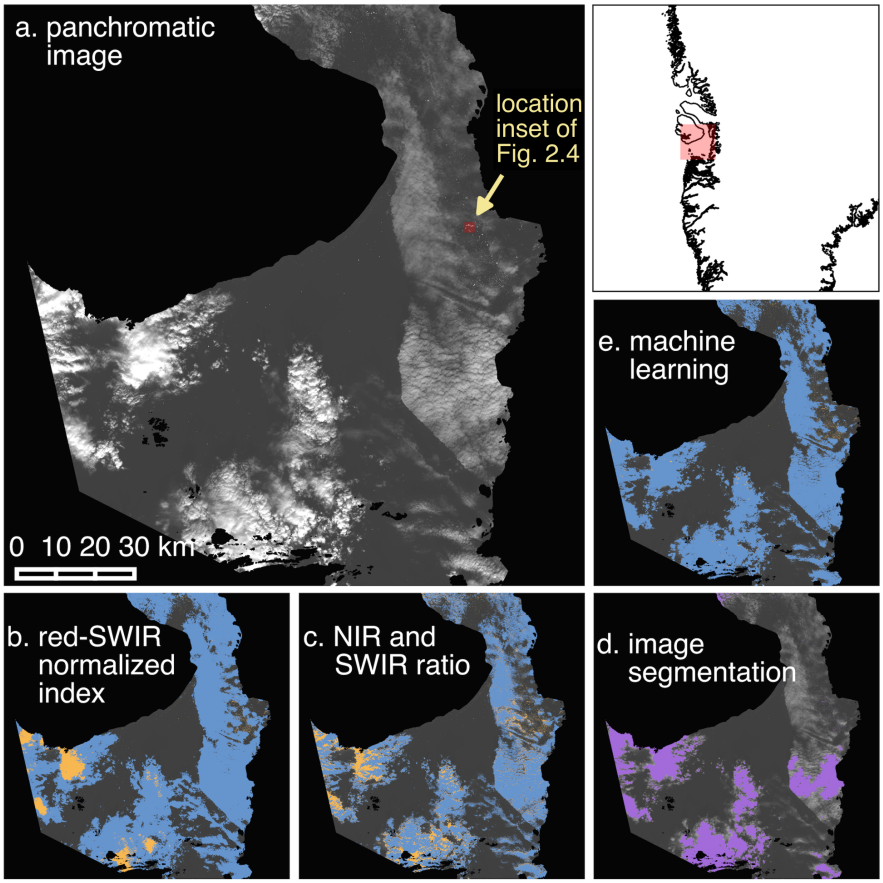

Figure 2.3: Comparison of multiple cloud masking and iceberg delineation techniques. a) Panchromatic (Landsat 8 band 8) scene of Disko Bay from 31 August 2013 showing multiple cloud types. b–c) Cloud mask (blue) generated using red–SWIR normalized index thresholding and NIR:SWIR ratio combined with SWIR reflectance band thresholding, respectively. Everything above the iceberg delineation threshold after cloud masking is shown in orange. d) Icebergs and clouds are detected simultaneously using image segmentation (purple). e) As in (b–c) for the machine learning-based cloud mask.

respectively), ultimately generating a ratio-based cloud mask using a combination of the NIR:SWIR ratio and SWIR reflectance (Figure 2.3c).

In an effort to capitalize on the textural differences between clouds and icebergs, rather than relying solely on spectral differences, we tested methods that rely on edge detection to identify features or classify images into segments (i.e. segmentation). If successful, these methods could potentially enable the effective identification of icebergs regardless of cloud presence (i.e. only icebergs would be

detected), eliminating the need for a cloud masking step. Edge detection uses gradients in reflectance between a pixel and its neighbors to identify transitions in brightness that often occur at the edges of distinct objects. The derived edge maps can then be processed using feature detection or segmentation methods to identify different features. Feature detection uses the edge map to isolate and identify objects with certain types of edge characteristics (e.g. fuzzy, gradual edges of clouds or sharp edges of icebergs). Segmentation starts with a series of "seeds", or small groups of pixels, building out from each seed until an edge is reached. The number, size, and location of the seeds may be determined automatically, randomly, or manually, with the resulting segmented objects dependent on the number and distribution of seeds. We derived an edge map for a panchromatic Landsat image from August 2013 and tested both feature detection (not shown) and segmentation methods (Figure 2.3d). The seeds for segmentation were determined automatically from the original panchromatic image.

Finally, we applied a machine learning technique called multinomial logistic regression to construct cloud masks. Multinomial logistic regression is a machine learning technique wherein a classified training set is provided as input and the computer generates a series of functions to relate the image pixel values and their classifications. Then, the model is run on validation datasets and the computer predicted values are compared to the actual values. To use multinomial logistic regression to create a cloud mask, we first had to train the computer model. We manually classified groups of pixels across six scenes with different cloud types. We classified the pixel clusters as either open water, opaque cloud, thin cloud with water underneath, thin cloud with iceberg underneath, or iceberg through clear sky. We extracted the top of atmosphere (TOA) reflectances and brightness temperatures for each classified pixel in the visible, NIR, SWIR, and thermal wavelengths. We combined these spectral signatures and associated classifications to

create training and validation datasets. Pixels from two scenes, one from each Landsat 7 and 8, were kept separate as a secondary validation dataset, while pixels from the remaining four scenes were randomly split into training and validation sets.

We trained and implemented our multinomial logistic regression model using the Python machine learning scikit-learn library (*Pedregosa et al.*, 2011). The generation of models using multiple combinations of bands enabled optimization of the model for accuracy and computational requirements while minimizing the number of bands involved in masking. Band combinations tested included TOA reflectance/brightness temperature of: 1) red, NIR, and SWIR; 2) red, NIR, SWIR, and thermal; 3) red, NIR, SWIR, thermal, and NIR–SWIR (wavelength centered at roughly ~1.63 µm); 4) red, NIR, SWIR, thermal, NIR–SWIR, and green wavelengths. We evaluated the model results for each combination of bands for accuracy and found that model performance was similar for all cases (95–97% precision). We eliminated the two options with the largest number of bands (options 3 and 4) to decrease computation requirements and based our final model selection on visual inspection of results. Specifically, we identified commonalities among the misclassified pixels and selected the model where incorrectly classified pixels could most easily be identified and reclassified automatically (e.g. regions of sensor saturation, as described below). The final model (option 2) used four spectral bands to classify pixels: TOA reflectance in the visible red, NIR, and SWIR bands (centered at roughly 0.66, 0.8, and 2.2 µm, respectively) and brightness temperature (centered at roughly 11.8 µm). Then, to improve the accuracy of the cloud mask over the central regions of very bright, white cumulus clouds where sensor saturation was common, groups of pixels smaller than a ten by ten square structuring element (300 m by 300 m) classified by the model as ice but completely surrounded by pixels classified as clouds were reclassified from ice to cloud and added to the cloud mask. The remainder of the classifications produced by the

model were designated non-cloud, and the cloud masks were morphologically opened (eroded and then dilated) using a cross shaped structuring element in order to remove small holes in the mask (Figure 2.3e).

The red, NIR, SWIR, and thermal bands used to create the cloud mask have a lower spatial resolution (30–100 m pixels) than the panchromatic band (15 m pixels) to which the mask was applied. Thus, we ignored potential mixed pixel effects and assumed that all higher-resolution pixels that fell within the cloud mask were clouds, resulting in a conservatively upsampled (i.e. 15 m resolution) cloud mask. For each scene, we applied the cloud mask to the panchromatic band prior to iceberg identification.

2.2.3.2 Land/Region of Interest Mask

To provide a consistent region for analysis that excludes potential land-fast ice and locations with persistent ice mélange, we generated a region of interest (ROI) mask that excludes regions within 100 m of the coastline and all fjords that enter the bay (Figure 2.1). Asiaq (*Asiaq, Greenland Survey*, 2014) provided the coastline shapefile used to identify the land boundaries. The ROI mask was applied subsequent to cloud mask application but prior to the iceberg delineation step (Figure 2.2).

2.2.3.3 Iceberg Delineation

Following application of the cloud and ROI masks to the TOA reflectance of the panchromatic band, the masked images were used to detect icebergs in the remaining open water regions. Icebergs were identified as pixels with reflectance values in the panchromatic band greater than 0.19. Given the stark contrast in brightness of icebergs from the surrounding water, the iceberg mapping results are fairly insensitive to the threshold value (Figure 2.4). However, manual inspection of iceberg masks produced using thresholds ranging from 0.17–0.21 indicated that a

threshold of 0.19 maximized the number of icebergs detected while limiting the number of false positive iceberg detections (i.e. identification of unmasked clouds, sea ice, or rough water as "icebergs"). The results of a quantitative analysis of iceberg size distributions extracted from one of our Landsat 8 scenes using iceberg identification thresholds ranging from 0.17–0.21 supports the qualitative inspection and is presented in Section 2.3.4. Although the multinomial logistic regression model used to detect clouds was also trained to classify ice pixels, we chose to identify icebergs as described herein because visual inspection showed that thresholding captured more of the icebergs and allowed us to optimize the performance of the model for cloud identification.

After thresholding, adjoining pixels were assumed to be part of the same iceberg and were clustered accordingly. Close visual inspection of the iceberg pixel clusters revealed that in some scenes the edges of clouds missed by the cloud mask were falsely identified as icebergs. Rather than remove the scene from the dataset for abundant false positives (see Section 2.2.4), pixel clusters that were identified as ice but that bordered cloud along >40% of the cluster's boundary were reclassified as clouds. The remaining clusters were classified as iceberg and outlined automatically by the computer, with each pixel or group of pixels stored as a unique iceberg polygon. To avoid inclusion of portions of icebergs within fjord mouths or along scene boundaries, the algorithm removed any iceberg polygon touching the ROI polygon or a scene edge. The analysis of iceberg parameters presented below uses the resulting shapefiles of iceberg polygons. Total ice area was computed for each shapefile and used in conjunction with the amount of cloud cover and total scene coverage within the ROI to compute an ice–open water ratio.

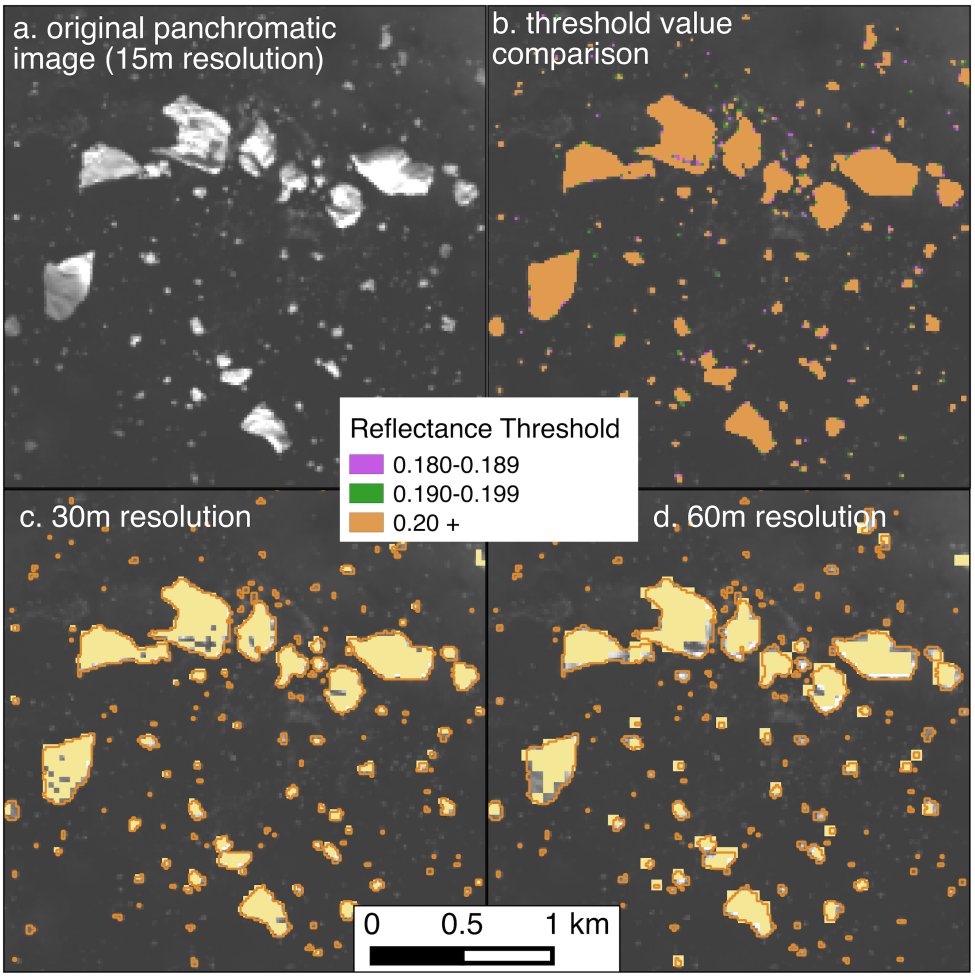

Figure 2.4: Influence of threshold choice and image resolution on algorithm performance. Location of panels is shown on Figure 2.3. a) Original panchromatic (Landsat 8 band 8) scene from 31 August 2013. b) The results of threshold sensitivity tests. Pixels identified as ice by the optimal threshold (0.19) are colored orange and green. c–d) Automated iceberg masks constructed with the optimal threshold (in yellow), but for 30 m resolution (c) and 60 m resolution (d) images. Orange lines in (c–d) show iceberg outlines derived from the 15 m resolution image.

2.2.4 Iceberg Detection Screening

The accuracy and reliability of iceberg detections was determined through semi-automated methods. Based on inspection of the time series of iceberg size distributions, scenes with an ice–open water ratio or maximum iceberg area greater than roughly the median plus one median absolute deviation (>0.008 or >2 km^2, respectively) were flagged as potential outliers, and we visually inspected scenes

with values exceeding these thresholds. For all scenes processed by the algorithm, we overlaid each iceberg shapefile on its corresponding panchromatic scene and visually inspected it at multiple spatial scales. QGIS (*QGIS Development Team*, 2017) provided the user interface for the inspection, which involved viewing the entire scene as well as taking a closer look at common problem areas such as along the borders of clouds or clusters of closely-spaced small icebergs.

We excluded some scenes from further analysis on the basis of this quantitative screening and manual inspection. Of the 65 scenes run, eleven were excluded at this point, leaving 54 scenes for the six years of our study, with 7–12 data points per year (mean: 9 acquisition dates per year). Reasons for scene exclusion at this stage included: 1) non-detection of large numbers of icebergs greater than one or two pixels in size; 2) large numbers of false positive detections of water, clouds, and/or sea ice as icebergs. With the exception of two scenes wherein sea ice or water resulted in false positive detections, wispy, semi-transparent cirrus clouds covered substantial portions of all of the scenes that were excluded on the basis of false detections. The presence of cirrus clouds was limited or nonexistent in all other cloudy scenes. Of the eleven scenes excluded during this step, six had values exceeding either the maximum iceberg size or ice–open water ratio thresholds. Thus, this inspection of results suggests that although there is no way to automatically screen for scenes with a large number of missed icebergs, the majority of results dominated by false positive signals can be detected and eliminated automatically through the use of ice coverage and iceberg size cutoffs.

2.3 Algorithm Outputs and Evaluation

We assessed the validity of our cloud masking and iceberg delineations using both qualitative and quantitative methods. We inspected and qualitatively evaluated the cloud masks throughout their generation and testing, while

quantitative analysis drove development of the final model used in the machine learning-based cloud mask. Comparison with previously published iceberg areas and iceberg size distributions enabled quantitative evaluation of the iceberg delineation portion of the algorithm.

2.3.1 Cloud Masks

Figure 2.3 shows results from application of our ratio-based cloud masks. The results produced using the red–SWIR normalized index were similar to those of the individual SWIR reflectance and red:SWIR tests (not shown). The performance of each ratio-based method to distinguish clouds from snow/ice varied widely with cloud type. In particular, very bright, white, fluffy cumulus clouds, which often had similar reflectance values as icebergs, resulted in abundant false identifications of clouds and/or icebergs. The combination of the NIR:SWIR ratio and SWIR reflectance to identify clouds improved the differentiation between clouds and snow/ice over either method alone and over other combinations of the ratio and threshold methods described above (Figure 2.3b–c) and was thus used as a point of comparison for the performance of our machine learning-based cloud mask. However, the ratio-based method suffered from the same problems as its components, making it ill-suited for unsupervised application to a large number of scenes with diverse cloud types. Further, for all ratio-based methods, we could not find a universal threshold that was sufficient for discriminating between clouds and icebergs in all scenes; the threshold value had to be tailored to each scene (*Jedlovec*, 2009), requiring extensive operator input and inspection.

The edge detection approaches to identify icebergs or clouds also proved inadequate (Figure 2.3d). The feature detection algorithm failed to identify icebergs (or clouds) and was too computationally intensive to run on a laptop, one of our design goals to ensure that the algorithm can be readily used by people outside of

the scientific community. Segmentation suffered from similar problems to the ratio-based approaches. In particular, segmentation of iceberg and cloud objects occurred simultaneously, providing no distinctions between clouds and icebergs. This result is unsurprising given that the segmentation map was seeded by applying a conservative reflectance threshold to the panchromatic band, which generally fails to differentiate clouds and ice/snow pixels. Manual seeding may have improved results but would require extensive user input for each scene. Random seeding is also not feasible because it would require dense enough coverage to include a seed in each iceberg and cloud segment (where clouds are present); this would likely lead to over-segmentation of the image. Given the poor performance of the edge detection methods for distinguishing clouds and ice, they were not pursued further.

The cloud mask we ultimately selected to include in our algorithm was that derived from the machine learning model (Figure 2.3e). Table 2.1 shows two confusion matrices, which demonstrate the performance of the model by comparing the model's predicted classifications with the manually derived actual classifications. Matrices are shown for two validation datasets, one from the randomly split training and validation dataset and the other one of the two validation datasets not included in the training dataset. Overall, the machine learning-based cloud mask most consistently and accurately discriminated between bright, white, puffy cumulus clouds and the bright snow/ice surfaces of icebergs without relying on the added step to reclassify small groups of pixels bordering clouds in order to construct an accurate map of cloud extent. The ratio-based cloud masks only reached comparable accuracy in mapping cloud extent when the cloud border reclassification step was added. Since this reclassification step relies on a semi-subjective threshold, reliance on its inclusion is not preferred. Manual inspection of the cloud masks also revealed that the ratio-based mask often classified significant amounts of open water as clouds, increasing the number of false negative iceberg detections and decreasing

		Training/Validation					2013-08-31				
		Model Predicted Classification									
		ice	*ice u.c.*	*water*	*water u.c.*	*cloud*	*ice*	*ice u.c.*	*water*	*water u.c.*	*cloud*
Actual Classification	*ice*	594	0	2	0	134	311	0	11	16	11
	ice u.c.	18	0	0	0	134	0	0	0	0	148
	water	0	0	8029	0	0	0	0	146597	0	0
	water u.c.	0	0	561	1211	371	0	0	4187	383	2490
	cloud	0	0	47	23	28762	19242	0	1	367	115936

u.c. = under cloud

Table 2.1: Confusion matrices for the machine learning-based cloud mask for multiple validation sets. The first (Training/Validation) shows the results of the validation dataset from the randomly sampled training/validation datasets made up of manually classified pixels from four scenes as outlined in the text. The second (2013-08-31) was generated from a Landsat scene collected 31 August 2013 and only used to validate the model.

the estimated open water area within the ROI. Given the superior performance of the multinomial logistic regression machine learning-based cloud mask among the methods we tested, we consider it to be the best cloud masking procedure for our analysis. An exhaustive testing of alternative machine learning-based approaches was beyond the scope of this investigation. However, our results indicate that machine learning provides a promising technique for future efforts towards improving cloud masks of optical imagery.

2.3.2 Total Iceberg Area

We evaluated algorithm performance by running the algorithm on several Landsat Collection scenes (20 August 2013, 7 August 2014, and 26 August 2015) covering Kangerlussuup Sermia Fjord, for which *Sulak et al.* (2017) previously established total iceberg areas. In order to match the methodology of *Sulak et al.* (2017) as closely as possible, we ran the algorithm as designed as well as with a higher reflectance threshold (0.28), without the land buffer, and without the step removing partial icebergs captured along the ROI and scene borders. The cloud mask was run in each case, even though *Sulak et al.* (2017) manually selected the

Threshold	*0.28*	*0.28*	*0.28*	*0.28*	*0.19*	*0.19*
Land Buffer	*no*	*no*	*yes*	*no*	*no*	*yes*
Border Rem.	*no*	*no*	*no*	*yes*	*no*	*yes*
Source	*Sulak**	*this study*	*this study*	*this study*	*this study*	*this study*
Date	**Area (m^2)**	**% dif.**	**% dif.**	**% dif.**	**% dif.**	**% dif.**
2013-08-20	1,240,000	4.9	6.5	6.1	-34.7	-24.2
2014-08-07	1,750,000	9.6	14.6	22.1	-71.9	-33.8
2015-08-26	1,350,000	-6.8	-5.2	-6.8	-52.6	-38.3

**Sulak et al.* (2017)

Table 2.2: Comparison of total iceberg areas for Kangerlussuup Sermia Fjord. Areas are shown as percent variation from *Sulak et al.* (2017) given choice of reflectance threshold, application of land buffer, and removal of partial icebergs included along the borders of a polygon defining the area of interest.

images as cloud-free. This resulted in very limited (<0.08% cloud cover over the area of interest), illustrating the good performance of our cloud mask.

Total iceberg areas for Kangerlussuup Sermia Fjord derived using our algorithm are in agreement with previously established values (Table 2.2) (*Sulak et al.*, 2017). Percent differences for total iceberg area vary by less than ten percent and are non-systematic. Our inability to precisely reproduce the total iceberg areas exactly can at least partially be explained by the potential differences in the ROI extent within the fjord, particularly near the glacier terminus but also at the fjord mouth. As expected, application of a buffer to land areas and removal of polygons intersecting our ROI polygon causes the percent error to become increasingly positive, because this step reduces the total ice area. Although the impact of these components of our algorithm on total ice area can reach up to 22.1% of the iceberg area calculated by *Sulak et al.* (2017), the absolute difference in ice area is quite small because the ice makes up such a small portion of the total area (the ice–open water ratio changes from 0.0045 to 0.0035).

Application of a lower reflectance threshold results in an apparent overestimation of iceberg area relative to *Sulak et al.* (2017). This is an interesting result given the lack of sensitivity to the threshold value that we observed for the

Disko Bay study site. We interpret the difference in optimal thresholds between study sites and the sensitivity of the Kangerlussuup Sermia Fjord study site to different thresholds as an indicator of the need for site-specific thresholds when calculating ice area. However, although the use of a uniform threshold across multiple study sites may bias estimates of ice-covered area, the number of detected icebergs is relatively insensitive to the choice of threshold, meaning that regional (i.e. not site-specific) thresholds should not substantially influence temporal variations in the number of detected icebergs or shape of the iceberg size distribution.

Unfortunately, there exist limited alternatives for further iceberg area validation. We tried comparing our results to a manually derived iceberg size distribution dataset, but even with the 15 m resolution of the Landsat panchromatic band mixed-pixels along the borders of icebergs made it difficult for experienced operators to confidently identify iceberg boundaries. This made it impossible to establish whether the objectivity of the quantitative threshold or the interpretation of the operator was "true" and "correct", resulting in a large mismatch in iceberg number and total area between the manually and automatically derived datasets, a problem that was exaggerated for icebergs less than ~10 pixels (2,250 m^2). Thus, high resolution datasets of iceberg sizes are needed for comparison with contemporaneous Landsat imagery to properly assess the limitations on using the archive to establish total iceberg area and iceberg size distributions through time, and we acknowledge the possibility that existing investigations using thresholding may be drastically misestimating iceberg numbers and total iceberg area.

2.3.3 Iceberg Size Distributions

Iceberg size distributions around Antarctica and Greenland have previously been characterized using both power law and lognormal distributions (e.g. *Tournadre et al.*, 2012; *Enderlin et al.*, 2016; *Kirkham et al.*, 2017; *Sulak et al.*,

2017). We tested power law, lognormal, exponential, and Weibull distributions using the Python powerlaw (*Alstott et al.*, 2014) library on two scene's size distributions and found that a power law distribution of the form $f(x) = x^{-\alpha}$, where α is the fit parameter or slope of the probability distribution in log-log space (Figure 2.5), weakly but consistently provided the best fit (see Section 4.3.2 for an explanation and evaluation of fit parameters).

Since our primary interest here is a consistent way to quantitatively describe the data and its variations through time, rather than necessarily capturing the exact shape of the distribution, we fit power law size distributions to each date's iceberg dataset using an x_{min} value of 1,800 m^2. This minimum iceberg size is equivalent to an eight pixel iceberg and was chosen because it provides a reasonable bound on the minimum size of iceberg the algorithm can confidently identify given the image resolution; this is especially true in regions of high iceberg density or when icebergs are visible through clouds. Further, this x_{min} value generally has a minimal fit uncertainty when compared with the fit uncertainties of other x_{min} values. We acknowledge that this relatively low x_{min} value likely influences the fit parameter values (*Clauset et al.*, 2009) but argue that it effectively limits data loss associated with the higher x_{min} values suggested by the software while minimizing the influence of large fluctuations in the smaller size fractions of icebergs. A detailed discussion of the challenges and limitations associated with rigorous fitting of heavy-tailed size distributions is provided in Sections 4.3.2 and 4.4.

2.3.4 Error Analysis

As demonstrated in Figures 2.4 and 2.5, satellite image-derived iceberg size distributions are fairly insensitive to the choice of the reflectance threshold used to identify icebergs in the cloud-masked scenes, provided the threshold value is tailored to the study site. Specifically, modification of the reflectance threshold by ~5%

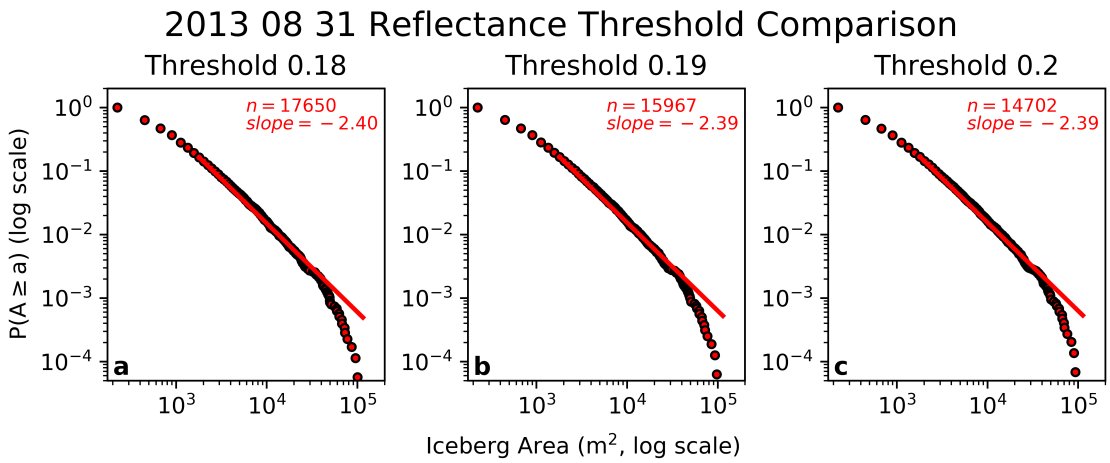

Figure 2.5: Iceberg size complimentary cumulative distribution functions for several different reflectance thresholds for the 31 August 2013 scene. Fitted power law curves (in log-log space) show characteristic decay of iceberg areas 1,800 m^2 and larger, as discussed in Section 2.3.3. n is the total number of icebergs detected, including those smaller than 1,800 m^2.

(~10%) to 0.18 and 0.20 (0.17 and 0.21) resulted in changes in the slope of the power law fits of <0.4% (<0.9%). Even large changes in threshold values (e.g. ~50%) resulted in comparatively small (<9%) changes in the fitted power law slope, although the uncertainties in ice coverage and number of icebergs (>50–100%) were close to the proportional changes in threshold. Manual inspection of the results from these large threshold variations shows the lower threshold resulted in an increase in the number of false negatives and the higher threshold resulted in an increase in the number of false positives from other noise in the image. Regardless, the small changes in slope even with large changes in the threshold value suggest that the fitted power law slope remains a robust metric to describe the size distribution.

The generation of scene mosaics and upsampling of lower resolution bands also introduces error into our analysis. Since Landsat scenes utilize the UTM projection, the generation of mosaics often requires reprojection of one scene so that the same UTM zone is used by both scenes in the mosaic. During mosaicking, pixel values in overlapping portions of the scenes are averaged. Due to coregistration errors, which

can skew the location of icebergs between scenes, pixel averaging has the potential to lead to both false positive and false negative iceberg identifications; iceberg pixel values may drop below the threshold used for iceberg detection, causing icebergs to be missed, or small icebergs may be double-counted. In line with previous studies, careful qualitative inspection of the overlapping region of several mosaics suggests that the geolocation errors are on the order of the pixel resolution (*Storey et al.*, 2014) and are sufficient for image mosaicking without compromising the detectability of icebergs or resulting in double counting of small icebergs. The impact of upsampling to match the highest spatial resolution bands is limited to the application of our cloud mask to the panchromatic image. Our iceberg size distributions are similar within a given time period regardless of the amount of cloud cover in a particular scene, suggesting that the upsampling of our cloud mask to match the spatial resolution of the panchromatic band does not affect our results.

2.4 Example Application and Discussion

Beginning in 1997, Sermeq Kujalleq underwent a period of rapid retreat, thinning, and acceleration that included the loss of a floating ice tongue in the early 2000s (e.g. *Joughin et al.*, 2004; *Luckman and Murray*, 2005; *Holland et al.*, 2008; *Bondzio et al.*, 2017). As the terminus of Sermeq Kujalleq transitioned from a persistent floating ice tongue to a terminus grounded in deeper water, the dominant calving style shifted from infrequent calving of tabular icebergs towards more frequent calving and overturning of full thickness icebergs and smaller partial-thickness icebergs (e.g. *Amundson et al.*, 2008; *Joughin et al.*, 2008; *Bassis and Jacobs*, 2013; *Cassotto et al.*, 2015). This change in calving style, and consequently calving energy (*Bassis and Jacobs*, 2013), produces icebergs with different geometries. Since iceberg decay is strongly controlled by iceberg geometry,

here we explored whether the change in Sermeq Kujalleq's calving could be inferred from a shift in iceberg size distributions over time.

We applied the semi-automated algorithm, using the machine learning-based cloud mask, to the Landsat archive for Disko Bay from 2000–2002 and 2013–2015 (Figure 2.6). We chose these year ranges to span the time period of greatest change in calving behavior of Sermeq Kujalleq (*Amundson et al.*, 2008; *Joughin et al.*, 2008) as well as avoid missing icebergs in whole or in part due to the striping caused by the SLC failure on Landsat 7. Although methods exist to "fill in" the missing data, these methods rely on landscape continuity through space or over time. The transient nature of icebergs means there is no reliable way to fill in the image gaps, thereby limiting the accuracy of an iceberg size dataset derived from this imagery.

Ice coverage is a function of the total ice-covered and open water areas relative to the observed area for that scene. We present ice coverage as an ice–open water ratio (Figure 2.6a) in order to account for differences in scene extent and cloud cover. The ice cover in Disko Bay has evolved in conjunction with the changes occurring at the terminus of Sermeq Kujalleq (Figure 2.6a). During the later time period (2013–2015), the range of ice–open water ratios is notably larger relative to the turn of the century (2000–2002).

Iceberg size distributions are represented by the slope of a fitted power law curve, as described in Section 2.3.3. The fitted power law slopes for our iceberg size distributions fall within the range -1.80 to -2.89, with a median of -2.12 (Figure 2.6b), in agreement with previously published values for iceberg size distributions in Greenland's fjords (-1.9 to -2.3 in *Enderlin et al.* (2016) and -1.62 to -2 in *Sulak et al.* (2017)). The fitted power law slopes have a mean goodness of fit error of 0.024 and an uncertainty of less than 0.4%, calculated as the change in slope value resulting from a ~5% change in the ice detection threshold value. Interestingly, the size distributions of icebergs in the bay suggest a small but

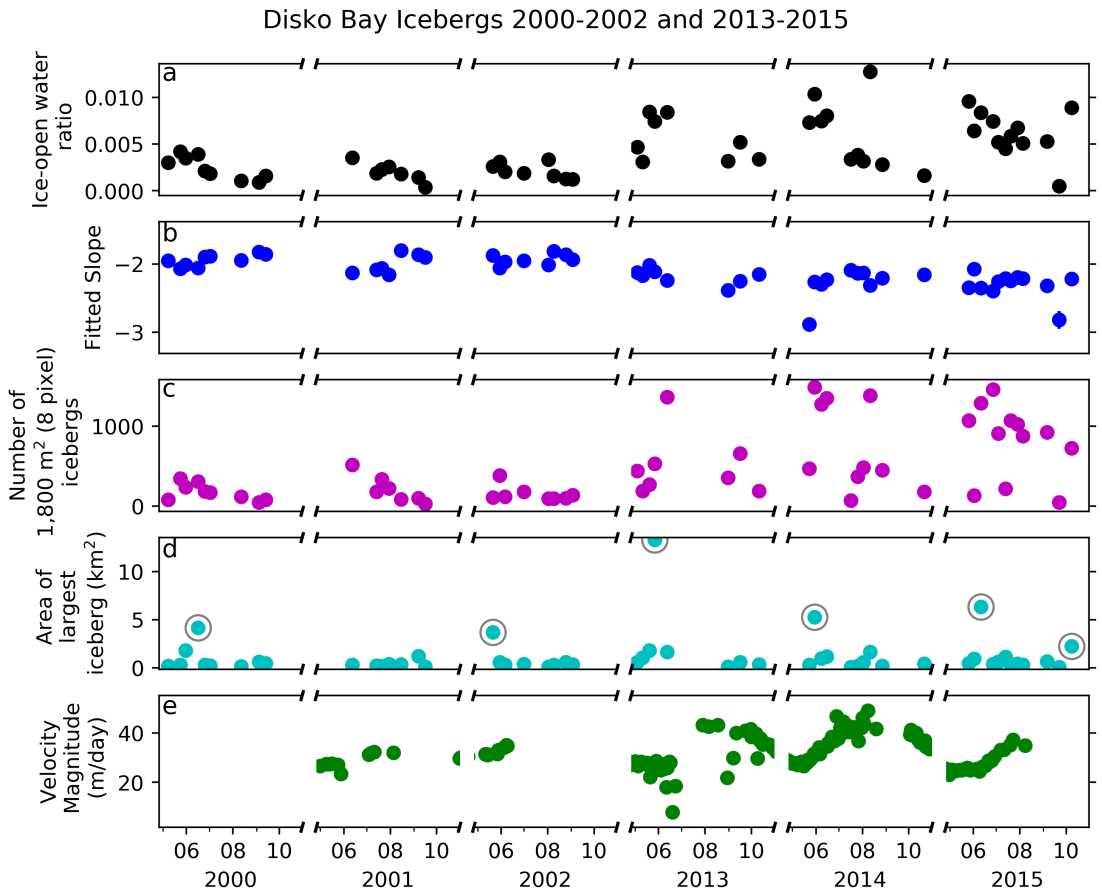

Figure 2.6: Iceberg data extracted from Landsat scenes spanning 2000–2002 and 2013–2015. a) Ice–open water ratio. b) The slope of the power law curve fit to the iceberg size distribution for each scene. Error bars showing the goodness of fit of the slope to the distribution are obscured by the symbol in almost all cases. c) Number of eight pixel (1,800 m^2) icebergs. d) Plan view area of the largest iceberg. Circled points are >2 km^2. e) Surface velocity magnitude 1 km upstream of the terminus.

significant decrease in slope values between the two time periods. For 2000–2002, the median slope was −1.96 (±0.03) while for 2013–2015 the median slope was −2.26 (±0.02). Although submarine melting of icebergs will also affect iceberg size distributions (*Kirkham et al.*, 2017), we hypothesize that temporal changes in submarine melting had little influence on the observed shift in iceberg size distributions for two reasons. First, subsurface ocean observations in Disko Bay suggest that the waters in the bay warmed in the late 1990s and have remained relatively warm since then (*Holland et al.*, 2008; *Gladish et al.*, 2015). Second,

oceanic warming will preferentially decrease the abundance of small icebergs due to their high surface area to volume ratios, with warmer near-surface water temperatures driving increased melt. This will effectively remove icebergs in the smallest size fractions and will likely manifest in iceberg size distributions as a shift from fitted power law to lognormal size distributions (*Kirkham et al.*, 2017). If we consider that the total volume of melt is a function of both the melt rate and time period, then we can look at changes in iceberg size distributions with distance from the source as an analog for changes in the magnitude of melting. As such, the shift towards a lognormal iceberg size distribution observed by *Kirkham et al.* (2017) suggests that any melt-driven changes in the size distribution would be counter to what we observe.

The observed changes in ice cover and slope of the size distribution are likely driven by the concurrent increase in the number and frequency of times that a large number of 1,800 m^2 (eight pixel) icebergs are present in the bay (Figure 2.6c). During 2000–2002, none of the scenes analyzed have >1,000 icebergs in the smallest size bin (1,800 m^2), whereas during 2013–2015 at least an eighth of the scenes have >1,000 small icebergs and over a third of scenes have >500 small icebergs. The increased presence of small icebergs between the 2000–2002 and 2013–2015 observation periods drives the steepening of the fitted power law slope (Figure 2.6b) and matches anecdotal evidence from boat captains operating in Disko Bay, who lamented the difficulty of navigating and setting long fishing lines in the mid 2010s due to the large number of small icebergs present in the bay. We interpret this change in the abundance of small icebergs in the bay as a consequence of the change in the dominant calving style of Sermeq Kujalleq. As the glacier's terminus geometry evolved from persistently-floating to seasonally-grounded (*Joughin et al.*, 2008), the associated increase in calving energy resulted in an increase in iceberg fragmentation and thus an increase in the number of smaller icebergs in Disko Bay.

The maximum size of icebergs detected in Disko Bay remained relatively constant during this time period (Figure 2.6d). Some icebergs >2 km^2 (approximately an order of magnitude larger than the maximum size of icebergs able to pass over the sill in Ilulissat Isfjord) were not excluded from our results because manual inspection (see Section 2.2.4) revealed that they are localized areas of potentially unnavigable sea ice that have little influence on the derived ice–open water ratio.

We compared the iceberg dataset to contemporaneous glacial datasets in order to further probe the potential connection between changes in the dynamics of Sermeq Kujalleq and the iceberg size distributions and ice cover in Disko Bay. Recent numerical modeling of calving dynamics by *Benn et al.* (2017) suggests that changes in calving style result from changes in the relative buoyancy of the glacier terminus. Relative buoyancy is defined as the water depth at the terminus relative to the water depth required for ice flotation (*Benn et al.*, 2017). To determine whether changes in relative buoyancy, and thus calving dynamics, could have driven the observed changes in iceberg sizes and ice cover in Disko Bay, we calculated the relative buoyancy of Sermeq Kujalleq's terminus during the early 2000s and mid 2010s. Specifically, we extracted ice surface elevation from pre-IceBridge (2001–2002; no data were available for 2000) (*Thomas and Studinger*, 2010) and WorldView image derived DEMs (2013–2015) (DEMs were created by the Polar Geospatial Center from DigitalGlobe, Inc. imagery) at a point located one kilometer upstream of the terminus. The water depth at each ice elevation point was taken as the depth of the bed given by BedMachine v3 (*Morlighem et al.*, 2017b). For each observation, the ice thickness was estimated assuming buoyancy. The ice surface elevation was multiplied by the density of sea water (1027.3 kg/m^3) and divided by the difference between the density of sea water and ice (900 kg/m^3). If the thickness of the presumed floating ice exceeded the bed depth, then the ice was considered

grounded and the ice thickness was instead calculated as the difference between the ice surface elevation and the bed depth. The water depth required for ice flotation was calculated following Equation 4 in *Benn et al.* (2017) and used as input for relative buoyancy estimates. Prior to 2002, minimum relative buoyancy values were ~2, well beyond the "super-buoyant" threshold of 1.1 suggested by *Benn et al.* (2017). From 2013–2015, relative buoyancy values were ~0.84, demonstrating that the terminus had shifted from a super-buoyant floating ice tongue to a fairly well grounded terminus (*Benn et al.*, 2017).

The change in terminus geometry since the early 2000s is also reflected in the record of near-terminus velocity for Sermeq Kujalleq. We extracted Landsat-derived surface velocities for 2001, 2002, and 2013–2015 from the Technische Universität Dresden Velocity Fields of Greenland Outlet Glaciers data product (*Rosenau et al.*, 2015) at the same locations as the ice thickness data above. The time series of velocities corresponding with our iceberg datasets are shown in Figure 2.6e. The time series clearly illustrates an increased seasonal signal in Sermeq Kujalleq's velocity (*Joughin et al.*, 2014) and is indicative of the glacier's increased responsiveness to changes in backstress at the terminus as a result of the loss of its floating ice tongue and corresponding change in calving style (*Joughin et al.*, 2012).

2.5 Conclusions

Icebergs are a key component of ice–ocean interactions, impacting fjord circulation and stratification, ecosystem structure, freshwater flux, and coastal navigation and infrastructure. Yet even as the flux of icebergs to Greenland's coastal waters has changed in recent decades, a limited number of studies investigate the size distribution of icebergs and the controls on these size distributions. Here we present a semi-automated approach to delineate icebergs in optical (Landsat) satellite images. To test the performance of the approach and

demonstrate its utility, we provide an example application to six years (2000–2002 and 2013–2015) of Landsat images for Disko Bay, West Greenland.

Differentiation of clouds and snow/ice in optical imagery is challenging given their similar spectral properties, and cloud masking often requires a large number of steps and/or advanced computing capabilities. To eliminate clouds from our scenes, we developed a computationally efficient cloud masking scheme using machine learning to identify clouds. A comparison of multiple cloud masks for the same scenes suggests that the machine learning-based cloud mask performs better than the commonly used ratio-based approaches to delineate clouds. Thus, we recommend that studies leverage similar machine learning-based cloud masking approaches in order to utilize Landsat scenes with partial cloud cover over glaciers and sea ice.

To construct an iceberg size distribution time series, we applied our semi-automated algorithm to a series of Landsat images from 2000–2002 and 2013–2015. After clouds and land were masked out of each scene using the machine learning-based cloud and ROI masks, the remaining portions of the TOA reflectance of the panchromatic band were thresholded to detect icebergs. Based on a comparison with previously published total ice area values for Kangerlussuup Sermia Fjord (*Sulak et al.*, 2017), we found that while the total ice area in that region was readily influenced by the choice of threshold value, in Disko Bay, the slope of the power law curve describing the iceberg size distributions was insensitive to the choice of threshold value.

Our iceberg size distribution time series shows that the size distributions of icebergs in Disko Bay underwent an important transition from the early 2000s (2000–2002) to the mid 2010s (2013–2015), concurrent with a transition in Sermeq Kujalleq's dominant calving style from low energy calving of tabular icebergs to high energy calving of full thickness icebergs. The change in calving style was driven

by a change in terminus geometry from that characterized by a persistently-floating ice tongue to a seasonally well-grounded terminus. Both decadal-scale change in the proximity of the glacier terminus to buoyancy and the seasonal velocity response of the glacier to terminus retreat, with an increase in velocity seasonality as the terminus becomes more grounded, support the change in calving style over this time period. This change in calving style was coincident with a pronounced increase in the number of small icebergs, a decrease in the power law slope describing the distribution of iceberg sizes, and an increase in the total ice cover in Disko Bay between 2000–2002 and 2013–2015. The temporal change in the number of small icebergs present supports anecdotal evidence from local marine navigators, who were adversely impacted by the shift. Based on these concurrent changes, we conclude that changes in calving style have an appreciable influence on iceberg size distributions. Expansion of this work to gain a better understanding of these changes is critical for navigation and predicting the spatio-temporal distribution of iceberg meltwater, which may influence the physical and biological properties of ocean water.

CHAPTER 3
INFERRING BATHYMETRY USING ICEBERGS

3.1 Introduction

Fjord bathymetry, in combination with oceanographic properties such as the depth of the boundary between the warm, salty, dense Atlantic water (AW) and comparatively cool, fresh polar water (PW), places a strong control on the ability of warm waters to enter fjords (*Rignot et al.*, 2012; *Straneo and Heimbach*, 2013). The presence of warm ocean water in glacial fjords exerts an important influence on the dynamics of marine-terminating outlet glaciers and thus the mass balance of the Greenland Ice Sheet (e.g. *Van den Broeke et al.*, 2009; *Vieli and Nick*, 2011; *Enderlin et al.*, 2014). Where heat transported in the subsurface AW on Greenland's continental shelf (*Holland et al.*, 2008; *Straneo et al.*, 2010; *Rignot et al.*, 2012; *Straneo and Heimbach*, 2013) enters fjords, it will enhance the submarine melting of floating ice tongues, ice mélange (a semi-rigid matrix of icebergs and sea ice), and grounded termini, ultimately leading to an increase in glacier mass loss through feedbacks associated with loss of frictional resistance generated at glacier termini and ice flow acceleration (e.g. *Benn et al.*, 2007; *Moon and Joughin*, 2008; *Joughin et al.*, 2008; *Nick et al.*, 2009; *McFadden et al.*, 2011; *Podrasky et al.*, 2014). However, despite the important influence of fjord bathymetry on glacier–ocean interactions and glacier mass balance, until recently our knowledge of fjord bathymetry was limited to a relatively small number of glaciers where observations had been acquired (*Morlighem et al.*, 2017a).

The resolution and spatial coverage of fjord bathymetry observations around Greenland is continually improving as the international scientific community collects new datasets (e.g. *Mortensen et al.*, 2011; *Schumann et al.*, 2012; *Fenty et al.*, 2016; *Rignot et al.*, 2016; *Morlighem et al.*, 2017a). Multiple freely available, gridded data

products now include coastal bathymetry constrained by available observations (e.g. IBCAO v3.0 (*Jakobsson et al.*, 2012), RTopo-2 (*Schaffer et al.*, 2016), and BedMachine v3 (*Morlighem et al.*, 2017b)). Recent efforts have focused on removing the physical impossibilities present in many compiled datasets through generation of realistic synthetic bathymetry and mass conservation constrained by observations (e.g. *Morlighem et al.*, 2017a; *Williams et al.*, 2017), with a focus along the coast and at glacier termini. Each new product and version improves upon those already available as additional surveys are conducted and spatial resolution is increased.

While these efforts are critical to providing realistic topographies, particularly in ice marginal areas, the bathymetry of portions of many of Greenland's glacial fjords remains unconstrained by observations. The presence of bathymetric sills that shallow water to <~200 m can effectively block warm AW located at depths of ~150–200 m from entering fjords and reaching glacier termini (e.g. *Holland et al.*, 2008; *Straneo et al.*, 2012; *Sutherland et al.*, 2014a). Thus, mapping of sills is critical for predicting the future magnitude of glacier response to oceanic warming (*Millan et al.*, 2018). However, data collected using field-based methods are time and resource intensive to obtain. Ship-based methods also rely on open water near glacier termini, which are often unnavigable due to the presence of closely packed icebergs and sea ice. Consequently, many fjords still lack the observations necessary to indicate the presence or absence of a sill.

Here we pursue a remote sensing approach that utilizes icebergs to expand upon the spatial coverage of fjord bathymetry datasets. Repeat satellite observations can be used to track iceberg motion over time. In deeper regions, iceberg motion is controlled largely by the ocean water currents at depth in the fjord (*Sutherland et al.*, 2014b; *FitzMaurice et al.*, 2016). Satellite observations of drifting icebergs can thus shed light on circulation patterns as well as minimum fjord depths. In contrast, the absence of motion suggests iceberg stranding and indicates the

presence of shallow waters (e.g. sills). In these shallow regions, the stranded iceberg drafts (i.e. keel depths) provide water depth maxima. Thus, observations of drifting and stranded icebergs enable the inference of qualitative bathymetry, and where iceberg drafts can be estimated, stranded icebergs can be used to place quantitative constraints on water depth. Here we describe how repeat satellite observations can be used to build qualitative bathymetry maps (Section 3.2.1). Then, we demonstrate the use of DEMs of icebergs constructed from very high-resolution stereo satellite image pairs to directly (Section 3.2.2.1) and indirectly (Section 3.2.2.2) infer bathymetry of shallow regions.

3.2 Methods

3.2.1 Qualitative Bathymetry and Study Sites

Icebergs were identified and their general movement patterns examined for four fjord systems as described below. These fjords were chosen because bathymetrc measurements were available to verify the qualitative, relative bathymetry estimates inferred from observations of iceberg motion. Panchromatic and color (red, green, and blue band composite) satellite images, collected by the sensors on board the Landsat, Sentinel, MODIS, and WorldView constellations, were viewed using the LandsatLook Viewer (landsatlook.usgs.gov), GloVis (glovis.usgs.gov), Danish Meteorological Institute (DMI) satellite images (ocean.dmi.dk), and DigitalGlobe (discover.digitalglobe.com) online viewers. For each fjord, icebergs were manually identified and, wherever possible, manually tracked across multiple images as they moved through the fjord.

Imagery was inspected until the operator felt confident identifying broad regions of iceberg drifting, stranding, and recirculating. We focused on images from the summer and fall, when sea ice was at a minimum. The number of images inspected varied depending on sea ice extent and cloud cover for a given year, but a minimum

of ten images were inspected for each location. In order to be considered "stranded", an iceberg was required to satisfy the following two criteria: 1) it occupied a semi-stationary position in numerous sequential images while other ice masses were seen freely moving around it; 2) it was free of sea ice and other ice debris to ensure that it was not simply immobilized by a matrix of floating ice. Regions of drifting were identified as areas that repeatedly cleared of icebergs quickly, regardless of iceberg size. Areas of recirculation were identified as locations where icebergs remained within a particular geographic area and were thus visible across multiple images but were clearly not fixed in the same location or rotating in place as a result of tidally driven fluctuations in water depth. The geographic extents of observed stranding, drifting, and recirculation areas were manually delineated as georeferenced polygons using QGIS (Figure 3.1) (*QGIS Development Team*, 2017).

We focused our efforts on four regions where large outlet glaciers calve icebergs with deep enough drafts to potentially become stranded in shallow waters at or above the depth of the AW–PW interface. To minimize bias introduced by previous knowledge of a region, one operator confirmed bathymetric data were available to validate our remote sensing estimates and another operator constructed the qualitative bathymetry maps prior to viewing any bathymetry products for the area. The qualitative maps were later overlain on the measured bathymetry to validate our hypothesis that iceberg drifting indicates deeper water while iceberg stranding indicates shallow waters (Figure 3.1). Three of the four regions investigated are located in West Greenland. Ilulissat Isfjord, which contains icebergs solely from Sermeq Kujalleq (Jakobshavn Isbræ), has a shallow sill that extends the width of the fjord where it enters Disko Bay (*Holland et al.*, 2008; *Schumann et al.*, 2012). In the Karrat Fjord system we focused on the fjord into which Rink Isbræ terminates, and in the Upernavik Fjord complex we focused our investigation on icebergs supplied by Naajarsuit Sermiat, several glacier termini (~40 km) north of

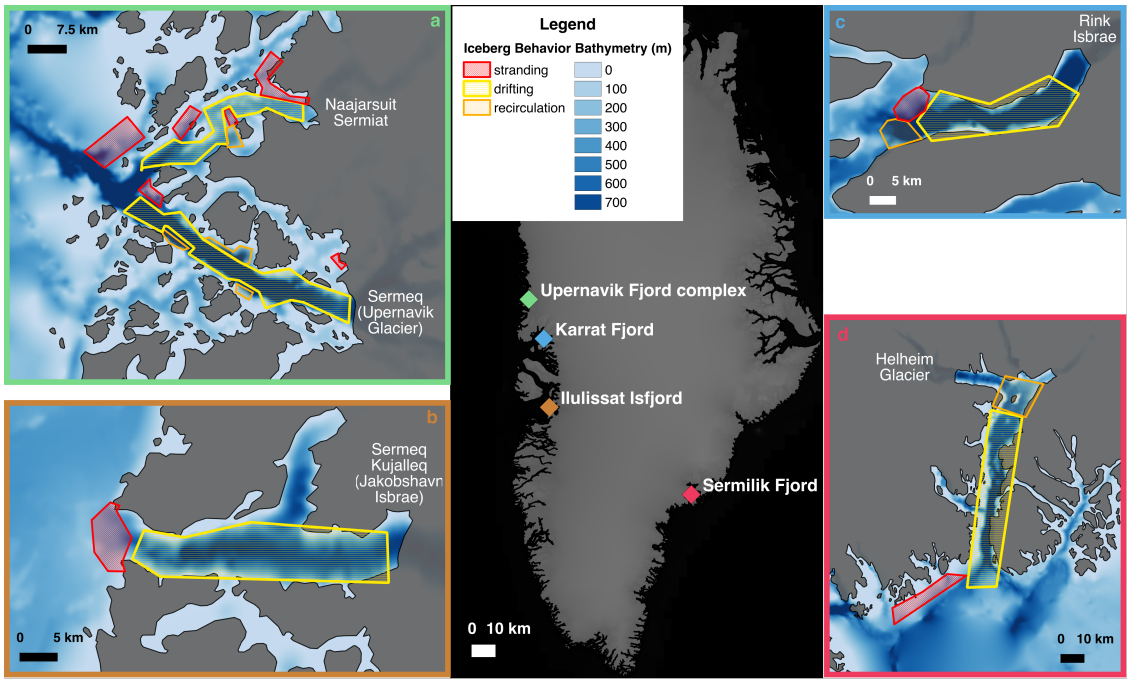

Figure 3.1: Qualitative bathymetry overlaid on BedMachine v3 bathymetry (*Morlighem et al.*, 2017b) for four locations around Greenland. Areas of stranding (red) and drifting (yellow) identified by iceberg movement correspond to bathymetric highs (light blue) and lows (dark blue), respectively. Areas with no outlines were not searched. Land is shown in grey. Glaciers supplying the majority of the icebergs in each fjord are labeled, with the location of each system identified in the center panel.

Sermeq (Upernavik Glacier). We refer to the fjord into which Naajarsuit Sermiat terminates as Naajarsuit Fjord. These two regions, Karrat and Upernavik/Naajarsuit, contain several shallow areas/partial sills but no distinct blocking feature across an entire fjord (*Rignot et al.*, 2016; *OMG Mission*, 2016b). Sermilik Fjord, the only site in East Greenland, contains icebergs calved primarily from Helheim Glacier and has no sill (*Straneo et al.*, 2010).

3.2.2 Quantifying Bathymetry in Regions of Iceberg Stranding

3.2.2.1 Water Depths Derived from Freeboards

The premise of our approach is that the draft of stranded icebergs grounded on bathymetric highs can be used to infer the water depth in each iceberg's location.

Iceberg draft depends on the iceberg's shape (*Hotzel and Miller*, 1983; *McKenna*, 2005), and ratios of iceberg draft to width vary (*Hotzel and Miller*, 1983; *Dowdeswell et al.*, 1992; *Bassis and Jacobs*, 2013; *Enderlin et al.*, 2016), making draft difficult to infer solely from measurements of surface dimensions. Here we infer iceberg drafts from freeboard observations assuming simplified submerged geometries (*Enderlin and Hamilton*, 2014).

Based on the results of the qualitative analysis, stranded icebergs were identified in WorldView stereo image pairs for two regions: Ilulissat Isfjord and Naajarsuit Fjord. These very high-resolution WorldView stereo satellite images were then used to construct ~2 m horizontal resolution DEMs with NASA's Ames Stereo Pipeline (ASP) software package (*Shean et al.*, 2016). To reduce computation time and resource requirements, DEMs were constructed for scene subsets containing only the stranded icebergs using ASP's stereo_gui command. Then, each DEM was adjusted to local sea level following the methods of *Enderlin and Hamilton* (2014). Specifically, a small subset of open water pixels near each iceberg was used to vertically shift the entire DEM so that open water was at an average elevation of 0 m. This adjustment inherently removes any potential DEM bias due to orbital uncertainty as well as offsets associated with the tidal height at the time of image acquisition relative to mean sea level (msl).

Each stranded iceberg was manually outlined in its respective DEM and the iceberg surface elevation with respect to water level (i.e. freeboard) was extracted for each DEM pixel within the iceberg outline. We assumed a simplified iceberg geometry with vertical walls following the iceberg's planar shape and a submerged bottom surface that was a pixel-by-pixel exaggerated reflection of freeboard determined using the assumption of hydrostatic equilibrium. Iceberg draft, d, was estimated from the freeboard observations, h, as

$$d = h\left(\frac{\rho_w}{\rho_w - \rho_i} - 1\right),$$

where ρ_i and ρ_w are the fjord-specific densities of ice and water, respectively. The fjord-specific density values used in our calculations are given below. In order to vertically coregister each iceberg draft relative to 0 msl of the local geoid and obtain the actual water depth at the time of observation, the modeled tidal height at the time of the DEM image pair acquisition was applied to each draft estimate. Tidal heights are from the Arctic Ocean Tide Inverse Model (AOTIM-5) (*Padman and Erofeeva*, 2004) for a site near each fjord's mouth, as in *Enderlin and Hamilton* (2014). Iceberg drafts, and thus water depths, were estimated using this approach for a total of 27 (10) stranded icebergs using seven (two) stereo image pairs for Ilulissat Isfjord (Naajarsuit Fjord).

The requirements and challenges of creating DEMs using ASP are discussed in more detail in *Enderlin and Hamilton* (2014) and *Shean et al.* (2016). The presence of large areas of open water around icebergs poses a challenge to the pattern matching employed by ASP, often resulting in DEMs with large areas of no data and spurious heights of tens of meters for some open water pixels. Each stranded iceberg DEM was inspected to confirm that enough of the iceberg was successfully mapped and the quality of the DEM high enough to provide a representative range of freeboard values as well as accurate sea level adjustments (typically 1–5 m after the influence of tidal height is removed). Areas used for sea level adjustment were carefully selected to avoid inclusion of spurious open water pixels. Inclusion of these pixels otherwise resulted in unrealistic sea level adjustments (>10 meters), consequently providing poor estimates of water depth.

The bathymetry derived from iceberg freeboards is subject to a number of sources of uncertainty. These can be broadly categorized as errors stemming from the vertical accuracy of the DEM and errors that result from the assumptions made in employing the method to derive water depth estimates. Systematic bias in iceberg freeboard due to uncertainty in the satellite position is effectively removed

during the local adjustment of open water pixels near each stranded iceberg. After accounting for the vertical adjustment due to tidal height using AOTIM-5, we found that the bias adjustments on iceberg DEMs ranged from 0.03–9.9 m and varied systematically by DEM. The largest mean residual for any of the DEMs was <3 m, with typical mean residual values of 0.5–1 m for a given DEM. Random errors due to mis-matching of pixels in the stereo images are reduced by ASP through erosion and mean difference to neighbors filtering applied to the pixel disparity map prior to point cloud generation (triangulation) (*Shean et al.*, 2016). Both *Enderlin and Hamilton* (2014) and *Shean et al.* (2016) estimated random uncertainty of vertically coregistered DEMs to be ~2–3 m.

Despite the automatic filtering done by ASP to minimize vertical errors, during manual inspection of the final DEMs we observed anomalous maxima values over or along the boundaries of portions of the input images that are highly reflective (Figure 3.2). These anomalously high freeboard values generally bordered no data portions of the DEM. Inspection of the good pixel map produced for the DEM sometimes identified these local maxima pixels as bad. To ensure that our draft estimates were not skewed by these "blunders" in pixel matching, we applied a three median absolute deviation (MAD) filter to the range of draft values for each iceberg. Manual inspection of the DEMs before and after application of the filter indicates that this simple filtering approach is effective, removing the majority of blunders while preserving the full range of more accurate elevations.

To determine the uncertainty on our bathymetry estimates, we propagated uncertainties in densities and freeboard through our draft calculations using standard error propagation techniques. Ice and ocean density vary spatially and temporally, and local measurements for these parameters are not available in all fjords around Greenland. The density of pure glacial ice is typically taken to be $917\,\mathrm{kg/m^3}$. Filling in of void space with meltwater would increase this value, while

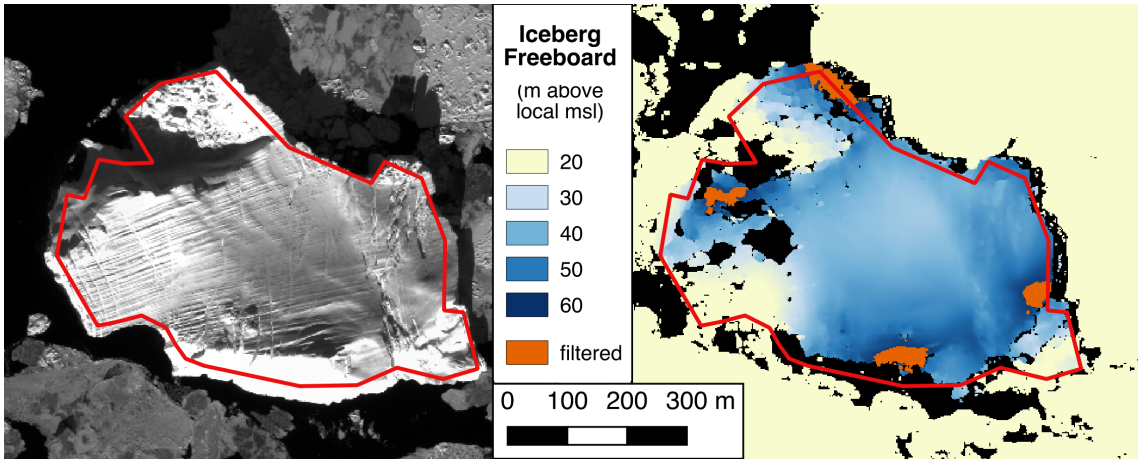

Figure 3.2: Maximum iceberg freeboards in DEMs. A panchromatic image (left panel, imagery © 2015 DigitalGlobe, Inc.) and DEM (right panel) of an iceberg stranded in Ilulissat Isfjord (image pair acquired 16 March 2015) show maximum iceberg freeboards tend to occur over and along the boundaries of highly reflective and no data regions. The iceberg is outlined (red) in both panels. In the panel showing the DEM, black indicates no data portions of the DEM while orange indicates high values filtered out by the three MAD filter. The freeboard elevations have been limited to a portion of their full range to highlight the maximum values.

increased iceberg fracturing and the presence of snow and firn would effectively lower it. Thus, following previous investigations, we used an ice density of $900\,\mathrm{kg/m^3}$ (*Enderlin and Hamilton*, 2014), which assumes a small amount of void space relative to solid ice. An associated uncertainty of $20\,\mathrm{kg/m^3}$ accounted for the unknown differences in ice density between icebergs due to differences in void space, fractures, composition, and refreezing. Ocean water density varies by location and depth and with time. Fjord-specific measured near-surface ocean densities plus or minus two sigma error (i.e. two standard deviations) of $1027.3 \pm 1.0\,\mathrm{kg/m^3}$ (*Gladish et al.*, 2015) and $1028.5 \pm 1.0\,\mathrm{kg/m^3}$ (*OMG Mission*, 2016a) were used for Ilulissat Isfjord and Naajarsuit Fjord, respectively.

The largest component of uncertainty in iceberg draft values stems from the influence of stranding on the validity of the assumption of hydrostatic equilibrium. For instance, where an iceberg stranded at high tide has its freeboard measured at low tide, the freeboard will be exaggerated relative to its value were the iceberg

floating, biasing our water depth estimates. In order to quantify the potential uncertainties stemming from deviations from hydrostatic equilibrium, we compared inferred water depths for the same iceberg stranded in Ilulissat Isfjord across two of our DEM dates (16 March and 25 April 2015). These data indicate that the water depth uncertainty introduced by deviations from hydrostatic equilibrium are on the order of 10 m (inferred water depths were 324 m and 313 m, at tidal heights of −0.64 m and −0.07 m, respectively). A portion of this difference is likely due to mass loss during the ~5.5 weeks between acquisition dates, suggesting that the potential water depth biases introduced by deviations from hydrostatic equilibrium are <10 m. Since we do not have repeat DEMs of all stranded icebergs, we calculated the tidal stage component of freeboard uncertainty for each iceberg using modeled tidal heights. Specifically, we determined upper and lower uncertainty bounds on freeboard equal to the difference between the modeled tidal height at the time of image acquisition and the nearest local maximum and minimum, respectively. Freeboard uncertainties ranged from 0.35 to 1.21 m (median: 0.72 m). Standard error propagation of these density and freeboard uncertainties ultimately provided constraints on our water depth (i.e. bathymetry) estimates, with uncertainties ranging from 10 to 63 m (median: 34 m). Because the magnitude of the component uncertainties varies across fjords and time, errors were calculated individually for each bathymetric estimate.

To verify the method, bathymetry estimates derived using the freeboard method were compared with gridded datasets of sonar-derived bathymetry. The bathymetry measurements used for the comparison were collected using multibeam echosounding and gridded to 20 m-by-20 m and 25 m-by-25 m resolution, for Ilulissat and Naajarsuit Fjords, respectively (*Schumann et al.*, 2012; *OMG Mission*, 2016b, respectively). Given that the shape of the submerged portion of the iceberg cannot be inferred from surface observations, this comparison allowed us to determine the

most representative iceberg draft value (e.g. mean, median, maximum) for inferring water depths at stranding locations. To develop these metrics, each stranded iceberg outline was overlaid on the corresponding bathymetric grid and the water depth at each covered gridpoint extracted. The horizontal uncertainty in ASP produced DEMs using WorldView images is <3–5 m (*Shean et al.*, 2016), which is close to the pixel size of the DEMs used for the analysis (2 m by 2 m) and much smaller than the horizontal extents of the icebergs (minimum iceberg width of all icebergs delineated was 71 m, with a median width of 336 m). Thus, the georeferencing accuracy of our iceberg polygons is well under the grid spacing of the measured datasets, making it unlikely that any gridded points were included/excluded as a result of georeferencing errors. Since there is no physical reason why the water depths extracted from the gridded bathymetric datasets should follow a normal distribution, we use the median, rather than the mean, of the sonar-measured bathymetry values to represent the "true" water depth for each iceberg's location.

3.2.2.2 Water Depths from Depth–Width Ratios

A particular challenge of the freeboard method of estimating water depth lies in its dependence on the temporal overlap between iceberg stranding and the collection of WorldView stereo image pairs. This is especially problematic in regions where the bathymetry and/or iceberg drafts are such that there is not a perpetual abundance of stranded icebergs. However, even in locations with a continual fleet of stranded icebergs (e.g. Ilulissat Isfjord), the number of bathymetry points derived using this method is limited by the availability of high resolution freeboard observations derived from cloud-free WorldView stereo image pairs. To overcome this limitation and increase the spatial coverage of our inferred bathymetry dataset, we used the available iceberg DEMs to derive fjord-specific depth–width ratios. Then, we

applied these ratios to the measured widths of stranded icebergs from Landsat 8 and Sentinel-2 panchromatic images to infer water depths.

We derived depth–width ratios for each fjord using iceberg width and median iceberg depth. Iceberg width was taken as the minor axis of a minimum bounding ellipse fit to each iceberg polygon. In Ilulissat Isfjord, the depth–width relationship was derived using the 27 stranded iceberg DEMs (Figure 3.3a, green squares). In Naajarsuit Fjord, to supplement the small number (ten) of stranded iceberg DEMs available, additional DEMs of eight non-stranded icebergs were constructed and included in establishing the depth–width relationship (Figure 3.3b, green diamonds). The ratio was calculated as the slope of a best fit line with a forced intercept of (0,0) (*Enderlin et al.*, 2016). To check the robustness of our ratios given the sparseness of our datasets, we also computed depth–width relationships for the much larger DEM-derived iceberg datasets used to establish iceberg melt rates in *Enderlin et al.* (2016, hereafter referred to as Enderlin2016) (Figure 3.3, brown circles). Their data were extracted from DEMs and provided as median drafts and total planar areas for each iceberg. Planar area was assumed to represent a circular iceberg and used to calculate iceberg width as two times the radius of a circle covering that area. Then, this width was compared to the median draft for each iceberg, where draft was derived as in this study using the assumption of hydrostatic equilibrium for iceberg freeboards extracted from a DEM.

We identified and manually outlined a total of 50 (Ilulissat) and 34 (Naajarsuit) stranded icebergs using Landsat 8 and Sentinel-2 imagery, calculated their widths, and then applied the fjord-specific depth–width relationship to estimate water depth. Vertical uncertainties on these bathymetry estimates stem from the same sources as the vertical uncertainties described above for the freeboard method, including unquantifiable uncertainties in the submerged iceberg shape and the propagation of uncertainties in iceberg width. Since the vertical uncertainties

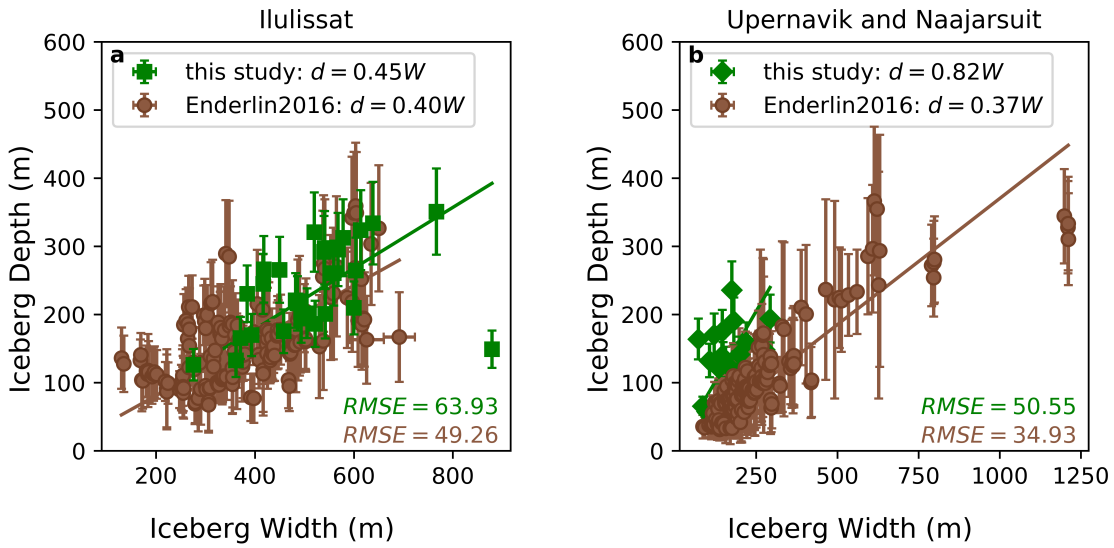

Figure 3.3: Depth–width ratios in Ilulissat and Naajarsuit Fjords. Green squares/diamonds show the results from this study, while brown circles show results from Enderlin2016. Best fit lines are used to determine the depth–width ratio, with RMSE values as shown. a) Results in Ilulissat Isfjord. b) Results from the Upernavik region, where the icebergs comprising the two datasets were derived from different parent glaciers.

stemming from tidal height are asymmetric, we provide conservative uncertainties by assigning the maximum magnitude vertical uncertainty to each iceberg DEM used in establishing the depth–width ratio. The median of these individual vertical uncertainties provides overall water depth uncertainties of 42 m and 26 m (Ilulissat and Naajarsuit Fjords, respectively) for values derived using the depth–width ratio. Uncertainties in iceberg widths stem from operator bias and image resolution and influence the vertical errors associated with inferring water depths. Errors resulting from image resolution are subjective because there is no way to determine the true iceberg width within the pixel resolution. For icebergs outlined in WorldView images and/or DEMs (pixel resolution $\leq$2 m-by-2 m), operators outlined icebergs conservatively to ensure all pixels within the outline were within the iceberg margins. For icebergs outlined in Landsat and Sentinel images (pixel resolution of 15 m-by-15 m and 10 m-by-10 m, respectively), the larger pixel size resulted in

abundant mixed ice–water border pixels around each iceberg. Operators outlined icebergs assuming that the actual iceberg edge was towards the iceberg center relative to this zone of mixed pixels. To quantify operator bias, all operators outlined the same two icebergs in Ilulissat Isfjord at several points in time throughout the data collection period. Widths ranged from 578–612 m and 384–441 m for the two icebergs, respectively. Applying our depth–width ratios to the range of the widths (34 and 57 m) translates to vertical uncertainties of $\leq$26 m. Since the operator bias in determining iceberg widths results in a vertical uncertainty component less than that stemming from the establishment of the depth–width ratio, we use the larger of the vertical uncertainties on our depth–width derived water depths (42 m and 26 m for Ilulissat and Naajarsuit Fjords). As noted above for the freeboard method, image georeferencing accuracy is not relevant given the georeferencing accuracy of the imagery relative to the iceberg size and gridded dataset resolution.

3.3 Results and Evaluation of Methods

3.3.1 Qualitative Bathymetry

Figure 3.1 shows the results of our qualitative examination of relative bathymetry inferred from iceberg movement overlaid on the BedMachine v3 bathymetry product (*Morlighem et al.*, 2017b). The BedMachine output is forced by observations in the areas shown, with errors close to 0 m for most parts of the fjords and larger errors (>150 m) near glacier termini and land boundaries where observational coverage is limited (not shown). Thus, BedMachine provides reasonably accurate bathymetry for assessing our qualitative method in these fjords.

Examination of the overlays suggests that regions of stranding and drifting correspond with relative bathymetric highs and lows (i.e. shallower and deeper water), respectively. In basins without measured bathymetry for confirmation,

deeper regions inferred by rapid iceberg transport may indicate the presence of deep troughs that channel subsurface water on the shelf towards the glacier terminus. An investigation of relative iceberg drifting speeds and pathways, while beyond the scope of this study, may provide additional insight into the fjord's bathymetric shape in these locations. Regions where icebergs were observed to recirculate without becoming stranded indicate areas with a more complicated bathymetry and tend to occur proximal to land features, particularly those associated with non-linear fjord geometries.

Because this is a qualitative method, errors cannot be quantified; however, the overlaid maps indicate a good agreement between relative bathymetry as suggested by our method and the actual relationships established by measured datasets. Although crude, these qualitative observations provide a robust first order approximation of bathymetry in basins with few or no bathymetric measurements at little to no cost. This information is helpful for: 1) providing context for point and centerline datasets, where a few high bathymetric points may be interpreted as outliers rather than detections of key features; 2) identifying the presence and probable extent of large features such as sills; 3) prioritizing locations for *in situ* measurements by ship or aircraft.

3.3.2 Quantitative Bathymetry

Quantifying water depth in shallow regions requires the presence of icebergs with drafts in excess of water depth (i.e. stranded icebergs) as well as sufficient WorldView stereo image pairs to construct DEMs of icebergs. Sermilik Fjord showed no regions of stranding within the fjord, as corroborated by ship-based seafloor mapping (*Straneo et al.*, 2010), and no WorldView stereo image pairs containing stranded icebergs were available for Karrat Fjord. Ilulissat and Naajarsuit Fjords contained stranded icebergs and had sufficient WorldView stereo

image pairs to estimate water depths in shallow regions. Thus, although we included four sites in our qualitative analysis, quantitative analysis was only performed in Ilulissat Isfjord and Naajarsuit Fjord.

3.3.2.1 Freeboard Method

Figure 3.4 compares water depths taken from gridded bathymetry datasets to those derived from iceberg freeboards in both study regions. The freeboard-inferred median (maximum) draft tends to under- (over-)estimate the sonar-measured water depth. This result makes sense when the complex submerged geometry of icebergs is considered. Icebergs are unlikely to have smooth, level bottoms. Thus, the iceberg will likely become stranded where its draft exceeds the median. It is also unlikely that the iceberg's mass is perfectly distributed below the surface such that each freeboard elevation is exactly balanced by a proportional mass directly beneath it, as is suggested by the assumption of hydrostatic equilibrium on a pixel-by-pixel basis. Thus, drafts inferred from freeboard maxima may exceed the true maximum iceberg draft, resulting in an overestimation of water depth. Taken together, the data suggest that the median and maximum values can be used to place bounds on the bathymetry for a particular location.

The MAD provides the uncertainty for sonar-derived water depths, ranging from 0.6 m to 12.8 m (median 2.8% of the measured water depth). Error for each inferred water depth is propagated as described in Section 3.2.2, and uncertainties range from 10 m to 63 m (median 18% of the inferred water depth). The use of median and maximum water depth values inherently captures propagated variations in iceberg freeboard. Thus, we suggest that propagated tidal uncertainties, rather than freeboard MAD values, provide a more appropriate measure of bathymetric uncertainty.

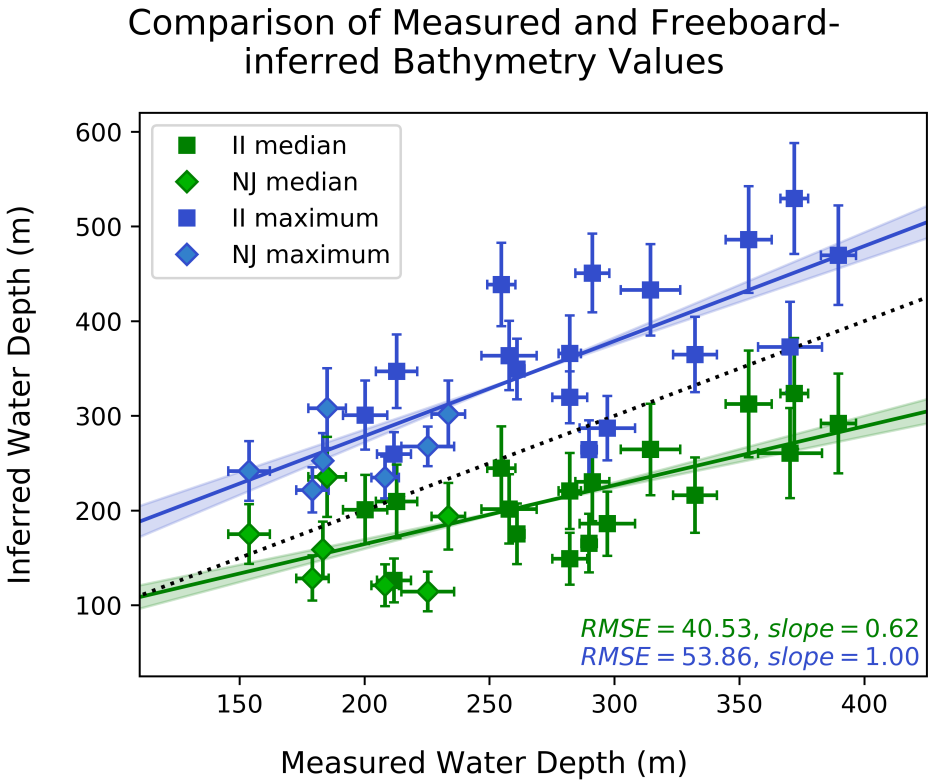

Figure 3.4: Measured and freeboard-inferred water depths for stranded icebergs in Ilulissat and Naajarsuit Fjords. Depths are in meters relative to 0 msl of the local geoid. Inferred depths are derived using the freeboard method, as described in the text. The blue (green) points compare the maximum (median) inferred and measured values. The slope and RMSE value for the best fit line for each parameter is shown in the corresponding color. Squares (diamonds) correspond to icebergs stranded in Ilulissat Isfjord-II (Naajarsuit Fjord-NJ). The black dotted line shows a 1-1 relationship.

The median and maximum inferred water depths provide important constraints on actual water depth in a given location. However, most applications (e.g. gravimetry processing inputs, circulation models, and bathymetric maps) require input of a single water depth value for each location rather than a range of possible values. To assess whether there is a more representative metric to approximate water depth, we constructed a cumulative distribution function (CDF) for each iceberg's pixel-by-pixel draft estimates and then found the percentile at which the CDF intersected the median sonar-derived depth. For Ilulissat (Naajarsuit) Fjord,

percentiles ranged from 50–100% (14–93%), where the 100th percentile indicates that the median sonar-derived water depth was greater than the maximum inferred water depth. In both locations, we found that 82% of pixel drafts were shallower than the median sonar-derived water depth. To test the utility of this representative value for inferring a single water depth, we extracted the 82nd percentile inferred water depth from each CDF. Then, we compared this inferred water depth to the median measured water depth (not shown). Although this approach produced reasonable water depths, we completed our analyses using median inferred values because of the broad range of matched percentiles for any given iceberg (14–100%) and the lack of compelling physical rationale for the similar median percentile values in the two fjords.

3.3.2.2 Depth–Width Ratio Method

The depth–width relationships established in this study are presented along with previously published median ratios in Table 3.1. A comparison of the values presented suggests our depth–width ratios are reasonable and represent stable iceberg geometries. Small differences in the depth–width ratio for Ilulissat Isfjord derived from data in this study and Enderlin2016 are likely driven by differences in assumptions about iceberg shape and stranding of our icebergs. The use of best fit ellipses will tend to overestimate iceberg width relative to a circle, in turn causing a decrease in depth–width ratio. This would tend to drive the ratios closer together. Thus, the differences in depth–width ratios presented herein are minimized with respect to our assumed iceberg shapes, suggesting that the observed differences are driven by other factors. Because they are grounded on a bathymetric feature and cannot remain floating throughout the tidal cycle, stranded icebergs may have artificially high freeboards relative to floating icebergs with the same width. This overestimation of freeboard would result in too-large draft estimates, in turn raising

the depth–width ratio. Further, the stranded nature of the icebergs will result in different proportional rates of mass loss relative to floating icebergs, resulting in different depth–width ratios. Specifically, water shear and wave action along the iceberg's lateral margins will tend to promote the formation of waterline notches and subsequent calving (e.g. *Savage*, 2001; *Scambos et al.*, 2008; *Moon et al.*, 2018), reducing iceberg width and driving an increase in an iceberg's depth–width ratio. Simultaneously, its contact with the bed will serve to stabilize the iceberg and reduce the likelihood of overturning even as the depth–width ratio increases (*Wagner et al.*, 2017). Because rates of relative water shear are likely to be higher for stranded icebergs relative to floating ones, we would expect to see higher depth–width ratios for stranded icebergs. In addition, the stranded icebergs have had longer to decay relative to the icebergs floating within the fjord, which could also drive a change in iceberg geometry and result in different depth–width ratios with distance from the calving front. Thus, we suggest that while sample size likely plays an indeterminate role, the primary cause of our higher depth–width ratio in Ilulissat Isfjord relative to that calculated using the Enderlin2016 dataset is driven by the stranded nature and older age of our icebergs and the associated differences in iceberg shape. The much larger differences between the two ratio values in the Upernavik region are likely the result of differences in the calving processes of the source glaciers (Sermeq and Naajarsuit Sermiat), though our value's similarity to that calculated by *Hotzel and Miller* (1983) suggests it is within the expected range of iceberg depth–width ratios. Among the other studies of Arctic icebergs and their size characteristics (e.g. *El-Tahan and El-Tahan*, 1982; *Dowdeswell et al.*, 1992) we were unable to find additional published median depth–width (or height–width) ratios with which to compare our data, though *El-Tahan and El-Tahan* (1982) provided potential upper and lower bounds for establishing a depth–width relationship.

Location	Depth–width ratio	Source
Ilulissat Isfjord	0.45	this study
	0.40	*Enderlin et al.* (2016)
Upernavik region	0.82	this study
	0.37	*Enderlin et al.* (2016)
Grand Banks	0.81	*Hotzel and Miller* (1983)
Sermilik Fjord	0.68/1.41*	*Sulak et al.* (2017)
Rink Isbræ	0.66/1.41*	*Sulak et al.* (2017)

*mean value for block/cone shaped iceberg

Table 3.1: Median iceberg depth–width ratios

3.3.2.3 Combining Quantitative Methods

As seen in Figure 3.5 and in agreement with the freeboard method, the median water depths estimated by the depth–width method tend to fall below the 1-1 line. This result is unsurprising given the depth–width relationships are derived using median iceberg draft values. An independent application of best fit linear trendlines (not shown) results in RMSE, slope values of 92.3 m, 0.78 (61.7 m, 0.08) and 73.8 m, 0.40 (72.9 m, 1.05) for the freeboard and depth–width methods, respectively, in Ilulissat (Naajarsuit) Fjord. The trendline RMSEs suggest that the methods can be used to infer water depths to within ±92 m of measured water depths. Combining the methods enables us to take advantage of their individual strengths. First we use the freeboard method to infer as many water depths as possible and establish a fjord-specific depth–width relationship. Then we employ the depth–width method, which requires significantly less person hours and computing power to derive each water depth estimate, to capture the full spatial extent of shallow regions.

A comparison of the results between the two fjords yields several important insights. First, the establishment of a fjord specific depth–width ratio is critical to the success of inferring water depths from stranded icebergs for which only widths are available (i.e. non-stereo images). Whether or not this relationship can

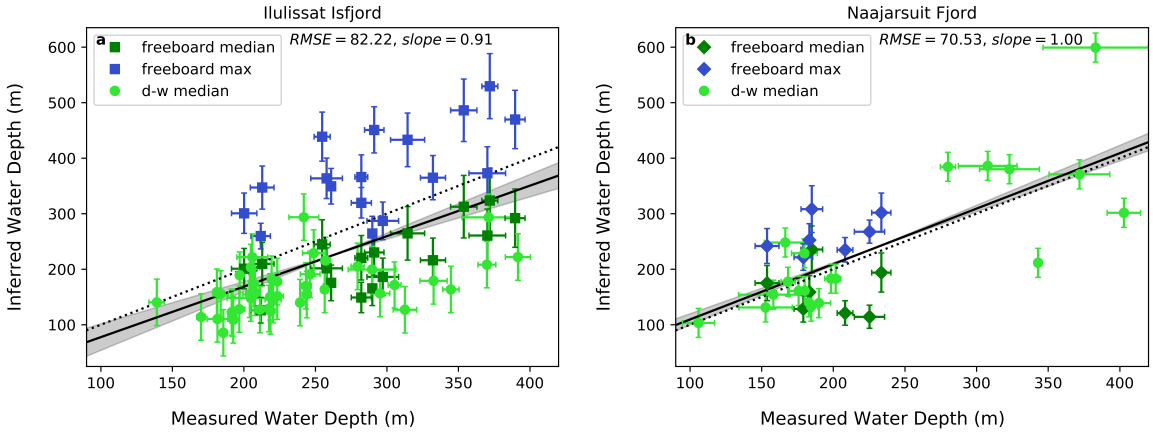

Figure 3.5: Measured versus remote sensing-inferred water depths for stranded icebergs. Depths are in meters relative to 0 msl of the local geoid. Inferred depths are derived using the freeboard (squares/diamonds) and depth–width ratio (circles) methods. a) Results from Ilulissat Isfjord. b) Results from Naajarsuit Fjord. The black dotted line shows a 1-1 relationship, while the black solid line and shading shows the best fit line to the data with a 95% confidence interval. The RMSE and slope of the best fit line are shown at the top of each figure.

successfully be inferred based on known features of the parent glacier, such as ice thickness at the terminus, rather than through the generation of multiple iceberg DEMs, is beyond the scope of this study but presents an interesting avenue for future investigation. Second, although a range of iceberg sizes is preferred, even a relatively small (18 icebergs) dataset can be used to establish a depth–width relationship that will produce reasonable water depth estimates (<75 m uncertainty) for stranded icebergs across a much broader range of iceberg sizes. Third, using remote sensing data to infer bathymetry, and in particular quantify water depth, may be a method best suited for application to regions with a high abundance of stranded icebergs (e.g. regions with sills blocking the path of all large icebergs from exiting the fjord), because this increases the likelihood of the presence of a large number of stranded icebergs that are fairly well spatially distributed and visible in multiple imagery sources.

The water depths derived using both methods illustrate that we can use these remote sensing-based methods to estimate water depths within ±92 m of measured water depth, with the typical uncertainties less than this amount (median error: 34 m). The linear fits to the data suggest that the methods estimate water depth accurately enough to provide useful information about the local water depth of previously uncharted sills and shallow regions. Although these uncertainties are likely too large to use the methods to determine the ability of AW masses to reach an individual glacier terminus, they still provide a useful metric for indicating regions where sills are present and further observations are needed to better constrain bathymetry.

3.4 Applications: Deriving Bathymetry in Unmapped Regions

To illustrate the utility of our method, we used it to obtain bathymetry estimates in several fjords. Specifically, we applied our method to extend observational coverage in two regions, illustrating the outcome by contouring the resulting combined datasets (Figure 3.6).

In Ilulissat Isfjord (Figure 3.6a–b) the extension of the dataset farther into the fjord clearly improves the contouring, effectively illustrating the presence of shallow portions of the known sill not readily visible in the observations from *Schumann et al.* (2012). At the southern portion of the fjord entrance into Disko Bay, there is a lack of measurements extending from the south-central (relative to the extent of our figure) shallow region to the peninsula that comprises the northeastern most land tip here. *Schumann et al.* (2012) suggested that this bathymetric high is a continuation of the land tip, which is supported by our extension of observational coverage. Further observations are needed, however, to fully resolve this feature.

In Naajarsuit Fjord (Figure 3.6c–d), the deepest portions of the fjord are well mapped. However, water depths inferred using remote sensing in the shallow regions

between the measured transects provides added detail on the nature of shallowing towards small islands situated within the fjord. This is illustrated well in the northern extent of Figure 3.6c–d, where four stranded icebergs indicate water depths in excess of those derived from interpolation between sonar-based measurements and land.

Water depths inferred using these remote sensing methods provide important constraints on water depth in shallow regions where no measurements are available. Applying the methods to quantify water depths requires deep-drafted icebergs, relatively shallow waters, and sufficient satellite imagery to both detect iceberg stranding and construct iceberg DEMs. Many suitable areas for application of the methods have recently been mapped as observational coverage around Greenland has expanded in the last several years (*Fenty et al.*, 2016). The techniques described herein provide a means to expand the spatial coverage of bathymetry maps, including in regions where glaciers are retreating beyond the coverage of ice penetrating radar-derived glacier bed topography maps. Many of Greenland's marine-terminating outlet glaciers currently have termini resting on shallow pinning points, including sills (e.g. *Nick et al.*, 2009; *Morlighem et al.*, 2017a; *Millan et al.*, 2018). As these glaciers retreat, their termini may calve large, full thickness icebergs that will become stranded on the now-exposed sills. The methods demonstrated herein can be used to estimate the height of these sills, enabling more accurate predictions of the future presence and impacts of AW masses on continued glacier evolution without the need for continual ship-based remapping of bathymetry at glacier termini.

3.5 Conclusions

Warm ocean waters circulating off the coast of Greenland have the potential to drive significant ice mass loss from the continent through their interactions with the

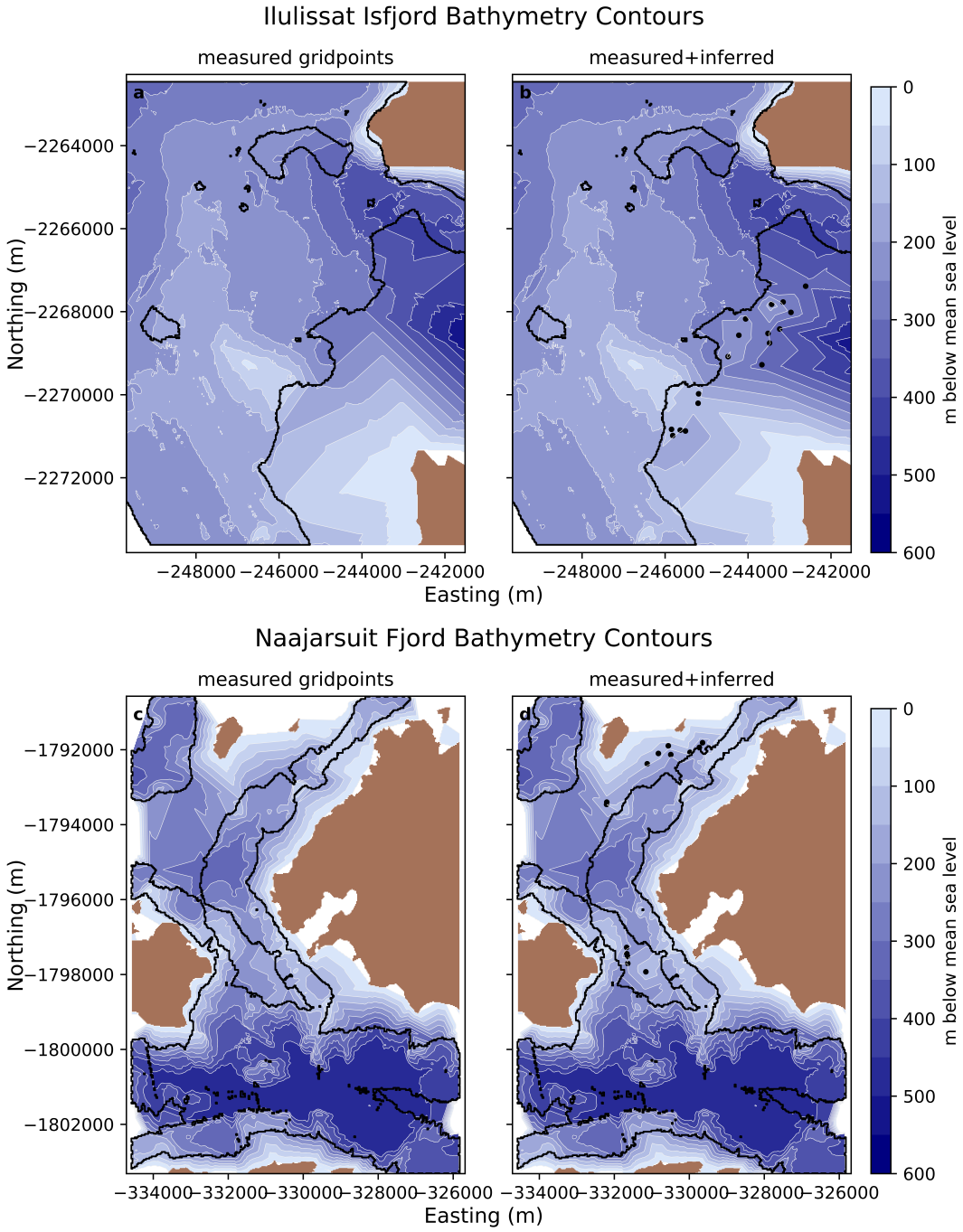

Figure 3.6: Bathymetric contours showing the utility of remote sensing inferred water depths in unmeasured areas. The top and bottom rows show the results from Ilulissat Isfjord and Naajarsuit Fjord, respectively. The left panels (a,c) illustrate contour lines (white, 50 m) using only multibeam observations. The right panels (b,d) show the improvements made by including our water depth estimates in portions of fjords where no observations exist. The black outline shows the extent of the measured datasets, where interior outlines within the outermost extent indicate holes in coverage (showing individual gridpoints would obscure the contours). Black circles indicate the location of remotely sensed data points added in the panels on the right.

ice sheet's marine-terminating outlet glaciers. The presence and movement of these warm waters at depth in glacial fjords are topographically steered by the bathymetric features between the shelf and glacier termini. However, despite recent advances in the number of observations and spatial resolution of bathymetric datasets (e.g. BedMachine, RTopo, IBCAO), changes in glacier termini positions and the high resource intensity of ship- and air-based bathymetric data collection methods means that bathymetry in many of Greenland's fjords will remain unmapped.

The central premise of our remotely-sensed iceberg-based bathymetry mapping methods stems from the fact that full thickness icebergs calved from many of Greenland's large outlet glaciers have drafts that exceed the water depth of shallow regions located within the fjords into which they calve. Thus, icebergs that can be identified as stranded on bathymetric highs can be used to qualitatively infer the presence of shallow regions and sills. In order to quantify water depths in these shallow regions, we used two related methods. DEMs of icebergs produced from very high-resolution stereo image pairs were used to convert observations of iceberg freeboard to iceberg draft estimates. Because the icebergs were stranded, the inferred draft values were used to constrain water depths. Based on a comparison between our freeboard inferred water depths and measured water depths, the mean and maximum draft values produced using this method provide a robust constraint on actual water depth, with an uncertainty on inferred water depths of ~18%. However, this method was limited by the availability of stereo image pairs of stranded icebergs. To expand the spatial extent for which we inferred water depths, we calculated a characteristic depth–width ratio for each parent glacier source and inferred water depths through application of the depth–width ratio to iceberg widths from optical satellite imagery.

To test the accuracy with which icebergs can be used to infer water depths and illustrate their utility, we applied our methods in Ilulissat Isfjord and Nujaarsuit Fjord (part of the Upernavik Fjord complex). Where measured bathymetry values were available, we compared our inferred water depths with measured water depths. Where our inferred water depths were outside the spatial extent of measurements, we regridded our data with the previously existing datasets to produce more realistic bathymetric contour maps. Overall, we found that although the uncertainties on inferred water depths may be upwards of 90 m (based on our combined results for all icebergs), individual uncertainties are generally <40 m. These large uncertainties make the inferred water depths unsuitable for constraining bathymetric features with high enough vertical resolution to determine the ability of warm subsurface ocean waters to reach marine glacier termini. However, the methods successfully identify shallow regions and provide useful first-order constraints on fjord water depths. These constraints on the water depths in unmapped regions contribute to the interpretation and processing of profile based datasets as well as provide critical information to prioritize locations where ship-based measurements are most needed and expand existing datasets where glacier terminus position has changed subsequent to initial mapping efforts.

CHAPTER 4
ICEBERG GEOMETRY AND SIZE DISTRIBUTIONS

4.1 Introduction

The previous two chapters have focused on the development of methods to derive iceberg datasets from remotely sensed optical imagery, including validation of these datasets and potential future applications. These types of broad temporal and spatial scale iceberg datasets are critical for furthering our understanding of ice–ocean interactions. Further, they contain the potential to enable detailed insight into iceberg environments as well as provide information about the parent glaciers. In an effort to connect the transition from observed power law iceberg size distributions near calving fronts to lognormal iceberg size distributions in the open ocean, *Kirkham et al.* (2017) present seismic data from icebergs decaying in Vaigat Strait (one of two pathways for icebergs to exit Disko Bay to the open ocean) and suggest this transition in size distributions may be due to changes in the underlying physics. Specifically, as iceberg properties change, the dominant decay mechanisms shift, ultimately driving the change in iceberg size distributions. Here we discuss in greater detail the importance of assumptions about iceberg geometry and size distributions and combine all of our datasets to probe the spatial patterns of iceberg decay from glacier terminus to open ocean in an effort to test the ideas presented by *Kirkham et al.* (2017).

4.2 Idealized Iceberg Geometries

An important observation made while perusing the literature for previously established iceberg depth–width relationships concerns the possibility for derivation of different ratios and relationships based solely on the character of the observations being input, rather than on any particular physical or regional attribute. In

particular, terms such as “width”, “length”, “height”, and “volume” are not always clearly defined or the methods of their derivation well documented, making comparison between datasets difficult. In the case of observations made from ship, horizontal dimensions are based on the observed length at the waterline which is undoubtedly impacted by the vantage point from which the measurement was made. For aerial and satellite based imagery studies, length and width are frequently treated as obviously derived parameters without explanation of the assumptions made in determining iceberg length and width. This omission is important because the methods used to determine length, width, and area may impact the conclusions drawn when the parameters are used in subsequent computations of volume, draft, and ratios (*Sulak et al.*, 2017).

To test the role of different assumptions about shape on observed datasets, we analyzed the variations in length, width, and area that resulted from using several different methods of estimating these parameters for a set of 77 manually outlined iceberg polygons in Ilulissat Isfjord. This dataset was derived to infer bathymetry using the freeboard and depth–width methods described in Chapter 3. Iceberg area was computed for each polygon using the Python gdal library’s built-in method and taken as a measure of the true planimetric area for each iceberg. A best fit rectangle and ellipse was fitted to each polygon and the major and minor axes of these simplified geometries used as length and width, respectively, with areas recalculated according to their respective shapes. These best fit rectangles and ellipses tend to overestimate the iceberg area by a median of 45% and 58% of the polygon area, respectively. Another approach to determining iceberg width, in line with previous investigations (*Hotzel and Miller*, 1983; *Enderlin et al.*, 2016), instead treats the iceberg area as fixed and assumes a circular or square iceberg geometry with width (=length) calculated based on the polygon area. We computed iceberg lengths and widths using both the best fit shape and fixed area methods and compared the

resulting lengths and widths to evaluate the impact of these assumptions. The widths computed using the best fit shape method are similar to those derived using the area preserving method, with circle/ellipse median widths of 390/398 m and square/rectangle median widths of 345/338 m, suggesting that the choice of shape type (ellipse versus rectangle) is more important than whether or not an area preserving shape is selected, assuming the plan view area is known. This conclusion does not hold, however, if the longer dimension, length, is used for the best fit methods. This makes physical sense, as an iceberg's stability is determined by the relationship between the smaller horizontal dimension (width) and draft, the length being less relevant here.

Depending on the method used to determine them, the range of median iceberg widths for our dataset is 338–398 m, where the 60 m difference represents roughly 16% of the width. For a given set of icebergs with depths all determined the same way, this range in iceberg widths results in a range of draft–width ratios. Of the 77 icebergs considered above, 27 had corresponding DEMs and thus draft estimates. Here, median draft was computed on a pixel-by-pixel basis from iceberg freeboards based on the assumption of hydrostatic equilibrium. For each shape, we calculated a draft–width relationship using linear regression on the width and median draft. As with the widths themselves, ratios vary by ~16% and range from 0.45–0.53, with smaller ratio values resulting from the use of a circle or best fit ellipse (0.47 and 0.45, respectively) than from a square or best fit rectangle (0.53 and 0.50, respectively). The area preserving methods have RMSE values that are lower than those of the best fit methods by 10–15 m.

The above analysis provides an important insight regarding comparisons of iceberg dimensions and properties calculated based on those dimensions. It suggests that assumptions about shape are important to consider when selecting and analyzing iceberg geometries (*Hotzel and Miller*, 1983; *Sulak et al.*, 2017). Method

selection depends on what information is most feasible to obtain, which depends on the dataset source (e.g. ship-based or aerial observations), and the purposes for which the geometries are going to be used. For applications that depend on area, the area preserving squares and circles are recommended. When width or length are being carried through calculations, the use of best fit rectangles and ellipses will more accurately capture the variations in these dimensions.

4.3 Iceberg Size and Decay

4.3.1 Mechanisms of Iceberg Decay

The mechanisms of iceberg decay can be broadly categorized as either melt- or mechanically-based. These mechanisms have been explored in varying levels of detail (a helpful review is provided by *Savage*, 2001) and are summarized briefly below. Subsequently, each category and the relative importance of each mechanism is explored.

Melt-based iceberg decay mechanisms are:

- Subaerial melting of the iceberg surface due to solar radiation
- Buoyancy driven convection
- Forced convection resulting from iceberg motion relative to the fluids surrounding it
- Convection induced by iceberg overturning
- Waterline wave erosion

Mechanically-based iceberg decay mechanisms are:

- Subaerial calving, particularly above waterline notches
- Calving due to buoyancy acting on submerged iceberg skirts (the "footloose" mechanism, *Wagner et al.*, 2014)

4.3.1.1 Melt-based Mechanisms

Solar radiation causes melting of the subaerial portions of an iceberg. *Savage* (2001) estimated melt rates of 1.7 cm/day for an iceberg located in the Labrador Sea based on incoming solar radiation in the month of July and the latent heat of melting ice. This rate is remarkably small relative to other mechanisms of iceberg mass loss and is probably overestimated for much of the year when the incoming solar radiation is reduced from its July maximum (*Moon et al.*, 2018).

Three types of convection-driven melting act on icebergs. Buoyancy driven convection occurs along the iceberg–ocean interface as a result of the input of cold, fresh meltwater from the iceberg into a comparatively warm, saline environment. The exception to this net upward flow is a small region along the bottom of the iceberg (*Savage*, 2001), where insufficient fresh water has been produced to generate considerable buoyancy effects (*FitzMaurice et al.*, 2017). Melt rates due to buoyancy driven convection have been approximated as parabolically related to the water temperature and are larger than subaerial melt rates but of a similar magnitude for the relatively low water temperatures found circulating in Greenland's coastal waters (*Enderlin et al.*, 2018; *Moon et al.*, 2018). Forced convection, or turbulent, melting occurs due to the relative motion of the iceberg in its surrounding media (air and water). These melt rates depend on differences in temperature, relative velocity, and surface area. Subaerial melt rates due to forced convection are of the same order of magnitude as solar radiation melt rates, rendering subaerial forced convection melt negligible relative to submarine forced

convection melting. Iceberg motion within a fjord is largely driven by the iceberg draft and its depth relative to ocean currents, rather than wind forcing (*FitzMaurice et al.*, 2016). Thus, side and basal submarine melt rates due to forced convection largely depend on the relative velocities that result from the force of water shear past the iceberg, integrated over the entire submerged area. These relative velocities are heavily influenced by the stratified shear flow of water past the iceberg (*FitzMaurice et al.*, 2016; *Moon et al.*, 2018), with melt rates further influenced by the velocity of the associated meltwater plume (*FitzMaurice et al.*, 2017). Iceberg melt rates have been shown to range from ~0.01 to 1.2 m/day (*Enderlin and Hamilton*, 2014; *Enderlin et al.*, 2016; *FitzMaurice et al.*, 2016; *Moon et al.*, 2018), with maximum relative contributions from basal melt and side melt parameterized in models at 1 m/day and 0.2 m/day, respectively (*Bigg*, 2016 as cited in *FitzMaurice et al.*, 2016). Convection induced by iceberg overturning is minimal relative to buoyancy-driven and forced convection given that it only acts when an iceberg overturns. Further, although rolling may induce convection-driven melting in the short term, over the longer term rollover increases an iceberg's lifespan due to the decrease in submerged surface area (*Wagner et al.*, 2017).

The formation of waterline notches due to wave erosion is often considered the most important mechanism for iceberg decay (*White et al.*, 1980 as cited in *Savage*, 2001). Here, several processes collude to enhance melt rates and promote the formation of notches. The physical controls on wave erosion are similar to those of forced convection-driven melting, with wave action driving high relative water–ice velocities and seasonally warm sea surface temperatures, particularly where vertical mixing of the surface layer is minimal, governing rapid mass loss (*Savage*, 2001; *Wagner et al.*, 2014). The resulting waterline melt rates are up to 1 m/d/°C (*Savage*, 2001; *Scambos et al.*, 2008). These rates vary by over a factor of three, however, depending on the season, with cold water and air temperatures and the

presence of sea ice in winter limiting forced convection and wave erosion (*Moon et al.*, 2018). Further, although waterline melt rates are frequently the highest localized melt rates, their overall contribution to iceberg mass loss is generally limited by the small portion of the iceberg's surface area over which they occur (*Moon et al.*, 2018). Rather, the large contribution to iceberg mass loss from waterline notch formation is likely due to the key role it plays in driving mechanical failure (*Wagner et al.*, 2014).

4.3.1.2 Mechanically-based Mechanisms

The fracture-based mechanisms outlined (subaerial calving, submarine calving) describe means of mechanical failure that result in portions of an iceberg calving off into multiple smaller pieces. These processes are similar to those that result in the formation of icebergs and ice islands from Greenland's marine-terminating outlet glaciers, and they are governed by similar physics that depend on the stress state of the iceberg and associated physical properties such as damage accumulation, ice thickness, and abundance and distribution of impurities such as meltwater. Subaerial calving generally results when a critical length of overhang is reached subsequent to the carving of a waterline notch and the tensile failure strength of the ice is reached (*Savage*, 2001). Similarly, submarine calving of iceberg skirts – the footloose mechanism – occurs when buoyancy forces overcome the tensile stress of the ice. The length scale on which submarine calving of skirts occurs depends on the damage accumulation, length of the foot relative to the length of the entire iceberg, and ice thickness (*Wagner et al.*, 2014). In both cases, the process can be modeled as a beam with a predetermined tensile failure stress (e.g. *Savage*, 2001; *Scambos et al.*, 2005; *Wagner et al.*, 2014).

The contributions of these mechanical failure mechanisms to iceberg decay depend on the iceberg's local environment, particularly the rate of waterline notch

erosion, and the strength of the iceberg. *Scambos et al.* (2008) noted for several Antarctic icebergs that these decay mechanisms (waterline notch erosion and subsequent mechanical failure) onset only after the iceberg had drifted into relatively ice-free, above freezing waters, resulting in iceberg length reduction rates that ranged from a few to tens of meters per day. However, the likelihood of the iceberg to fracture even after the formation of a waterline notch depends heavily on its tensile strength. Specifically, *Wagner et al.* (2014) find that in cases of sufficiently strong ice, an iceberg will not always fracture regardless of the foot length, instead adjusting so that the foot is floating at its natural buoyancy level.

4.3.2 Size Distributions

Previous characterizations of iceberg size distributions around Antarctica and Greenland have been described using power law, lognormal, and Weibull distributions (e.g. *Savage et al.*, 2000; *Tournadre et al.*, 2012; *Enderlin et al.*, 2016; *Kirkham et al.*, 2017; *Sulak et al.*, 2017). The application of different statistical models to describe iceberg size distributions suggests that the physics of iceberg decay plays an important role in determining the size distribution of ice pieces (*Savage*, 2001). Rates and patterns of iceberg melt and fracture vary based on local ice and climatological properties, resulting in different iceberg weathering regimes across and between study sites. For example, a recent analysis by *Kirkham et al.* (2017) suggests that at the time of calving icebergs follow a power law distribution which transitions to a lognormal distribution with distance from the calving location as different and increasingly fewer physical processes dominate the decay process.

The shape of any distribution function describing iceberg sizes (e.g. area, length, volume/mass) can be broadly described as highly skewed or heavy-tailed. As such, the data becomes easier to interpret when viewed in log-log space (Figure 4.1). The selection of bin sizes to describe frequency data in log-log space inevitably plays

a role in our interpretation of the data. Specifically, a probability density function (PDF) with linearly spaced bins (Figure 4.1a) clearly displays an inflection point in the data. The location of the inflection point, here at iceberg surface areas of ~10,000 m^2, depends completely on the choice of bin size and has no physically-based interpretation. Thus, using a PDF with linearly spaced bins to describe iceberg size distributions makes it difficult to fit size distributions to the entire dataset unless a maximum x value is defined (*Alstott et al.*, 2014), resulting in the unnecessary exclusion of a portion of the dataset. A PDF with logarithmically spaced bins (Figure 4.1b) effectively includes the larger icebergs in the distribution and smooths the inflection point, but the shape and slope of the curve are still influenced by the number of bins used. Alternatively, a complimentary cumulative density function (CCDF) (Figure 4.1c) provides a means of objectively fitting a size distribution without the need for determining ideal bin sizes (*Alstott et al.*, 2014). This approach is commonly taken in available computational libraries designed for testing power law and other similar heavy-tailed distributions.

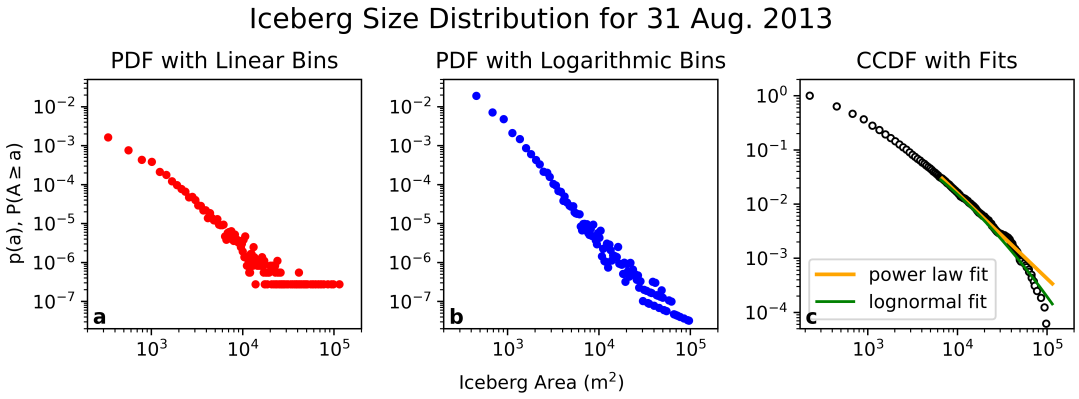

Figure 4.1: Size distribution of icebergs delineated by the automated algorithm for the Landsat scenes collected 31 August 2013. a) Iceberg area PDF in log-log space with linearly spaced bins. b) As in (a) with logarithmically spaced bins. c) CCDF for the dataset with modeled power law (yellow) and lognormal (green) fits. $n = 16145$, $n_{tail} = 492$.

The large number of methods employed in the literature for fitting iceberg size distributions suggests the non-trivial nature of fitting theoretical distributions to

natural phenomenon. Unfortunately, it is all too common that the preferred model used to fit size distributions is chosen based primarily on a qualitative inspection of the data rather than robust statistical methods (*Clauset et al.*, 2009). In the case of supposed power law distributions, the fitted parameters are often computed using a least squares fit to the data in log-log space, alternative distributions are not rigorously evaluated, and the statistical validity of the model for describing the dataset is not tested (*Clauset et al.*, 2009). However, the limitations imposed by statistical rigor have the potential to effectively eliminate large portions of a measured dataset, in turn making it difficult to characterize a natural system and suggesting that a compromise between pure and applied mathematics is necessary to describe the stochasticity of natural phenomena in a consistent framework.

As a starting point to determine the best fit models to describe our data, we use the poweRlaw package (*Gillespie*, 2015) for the open-source statistical software R (*R Core Team*, 2018). The package contains easy-to-implement methods for testing power law, lognormal, and exponential fits of the form:

$$power\ law : f(x) = x^{-\alpha}$$

$$lognormal : f(x) = \frac{1}{x} exp\left[-\frac{(ln(x) - \mu)^2}{2\beta^2}\right]$$

$$exponential : f(x) = e^{-\lambda x}$$

where α, μ, β, and λ are their respective fit parameters. It includes methods for determination of the best minimum x (x_{min}) value based on the Kolmogorov-Smirnov (KS) fit statistic, measures of model fit and estimates of parameter uncertainty using bootstrapping, and model intercomparisons using log likelihood-ratio testing (Vuong's method) to compare alternative distributions (*Clauset et al.*, 2009). The process of fitting and testing a statistical model using the package is outlined in detail in *Clauset et al.* (2009) and in the package's documentation. An iceberg size distribution from 31 August 2013 with potential

Power Law		**Lognormal**			**Comparison (power law x_{min})**		**Comparison (lognormal x_{min})**	
x_{min}	α	x_{min}	μ	β	R	p	R	p
6750	2.58	6525	5.59	1.67	−1.48	0.14	−1.64	0.101

Table 4.1: Iceberg size distribution fit parameters from poweRlaw for 31 August 2013.

model fits and relevant statistical parameters is shown in Figure 4.1 and Table 4.1. In this example case and for one other case tested (not shown), the exponential curve showed a visually poor fit to the data and exhibited very high x_{min} values with associated poor goodness of fit values for the x_{min} estimation. When compared to other models, the non-exponential models suggested a statistically significant better fit. As a result, the exponential model was not considered further as a potential curve for the iceberg size distribution data.

A key step in fitting a model distribution to a dataset begins with the determination of x_{min} values for each model. x_{min} is determined using the KS statistic as detailed in *Clauset et al.* (2009) and identifies the starting point beyond which the data can most accurately be described by a given distribution; over- or underestimation of x_{min} quickly influences the value of fit parameters, with a too-high x_{min} value being preferred to a too-low value. Although the minimum iceberg size is 225 m^2, the x_{min} values suggested by the software for the example size distribution are an order of magnitude larger, though they are similar for both the power law and lognormal models. In order to compare two distributions, they must have equivalent x_{min} values. Thus, we compared the power law and lognormal models using both x_{min} values. In both cases the p value was >0.1, suggesting we cannot reject the null hypothesis that one model is a better fit to the data. For future interpretations wherein R is statistically significant ($p \leq 0.1$), negative R values would indicate the lognormal model is a better fit. A visual inspection of the power law and lognormal curves fitted to the data provides qualitative confirmation

that the distribution could readily be described by either model. Acknowledging that neither model necessarily provides a better fit to the data but in pursuit of a quantitative description of the shape of the iceberg size distribution curve, we ran a bootstrapping procedure with 1,000 iterations using the power law model to determine the statistical significance of a power law fit and the uncertainty on the parameter estimate. The results of this bootstrapping suggest that a power law fit to the data is statistically significant (p=0.181>0.1). The fitted parameter (α), which is the slope of the power law fit, has a value of 2.58 $\pm$ 0.10. This value is notably higher than previously estimated values (*Enderlin et al.*, 2016; *Sulak et al.*, 2017) and the theoretically expected value of 3/2 (*Aström et al.*, 2014), suggesting that either the values determined here are slightly high, previous investigations have underestimated the fit parameter, and/or size distributions are influenced by an additional physical process that preferentially decreases the relative abundance of large icebergs and/or increases the relative abundance of small icebergs. The portion of the dataset fitted by the statistical model contains enough values (n ~500) to suggest the obtained parameter estimates are reliable, though the number of observations in the data tail is small enough (<1,000) that the algorithm's selection of x_{min} may be compromised in this case (*Clauset et al.*, 2009).

As noted above and qualitatively confirmed in Figure 4.1, here neither the power law nor lognormal distributions could be statistically determined to provide a better fit to the data, although the power law fit itself was able to provide a statistically valid representation of the data. The data spans a very large area over which multiple iceberg decay mechanisms are likely to dominate depending on the age of the iceberg, whether or not it is stranded, and how far it is from the calving front. Thus, based on the analysis by *Kirkham et al.* (2017) in Disko Bay and observations from *Dowdeswell et al.* (1992) in Scoresbysund Fjord System, one

might expect that dividing the iceberg dataset regionally will result in a clearer determination of the appropriate size distribution model(s).

4.4 Spatial Dependence of Size Distributions for Icebergs Calved from Sermeq Kujalleq

Relative iceberg age can be loosely inferred based on the iceberg's distance from the parent glacier, with the youngest icebergs nearest the calving front and the icebergs becoming progressively older with increasing distance from the calving front. In order to test the impact of iceberg age on the shape of iceberg size distributions, icebergs delineated semi-automatically and manually as described in Chapters 2 and 3 from the time period 2013–2015 were binned into four regions spanning Disko Bay and the mouth of Ilulissat Isfjord (Figure 4.2). The three bay regions were designed to isolate icebergs entering the open ocean through the Vaigat Strait (Region 0) versus those exiting south of Disko Island (Region 1) from those located east of the island (Region 2). The mouth (Region 3) captures icebergs likely to be stranded, previously stranded, or calved from icebergs stranded on the sill. Each iceberg centroid was calculated and used to sort the iceberg into the proper region; thus, icebergs found near the region edges may technically be partially within two regions. The use of the iceberg centroid assumes that a majority of the iceberg's subaerial area is within the region into which it is categorized. Given the number of icebergs and somewhat arbitrary divisions between boundaries, these border icebergs are unlikely a substantial enough percentage of the final datasets to impact our results.

Binned iceberg size distribution data from seven dates in 2011 and 2014 (Enderlin2016) were used to assess iceberg size distributions within Ilulissat Isfjord (Region 4) from the time of calving until they had traversed the fjord to reach the sill at the mouth into Disko Bay. Because the poweRlaw package requires

abundance data, rather than already binned data, as input for distribution fitting, an artificial dataset of iceberg areas was constructed from the binned iceberg size distribution data in order to analyze the Enderlin2016 iceberg size distributions. First, the seven binned datasets were combined into one large dataset with sixteen logarithmically spaced bins, where sixteen was the number of bins used during binning by Enderlin2016. Then, an artificial dataset of iceberg areas was built using the bin centers as iceberg areas and adding as many icebergs with each area as were in the total count for that bin. This data was ultimately used as the input for determining the iceberg size distribution for this region.

The poweRlaw package was used to test for power law and lognormal fits for each region. For regions 0–3, the x_{min} values used for the comparison were taken as the lower x_{min} values determined by the algorithm using the KS statistic to estimate power law and lognormal fits. Although this potentially results in a misestimation of fitted parameters (*Clauset et al.*, 2009), using the larger of the two values would provide a fit to such a small portion of the dataset as to render it meaningless. As it is, the x_{min} values determined by the algorithm result in a substantial reduction of the total number of values included in the fitted model (n_{tail}). The results of the parameter estimation and model comparison for each region are shown in Table 4.2, with the fitted parameters from the model comparison (not shown) depicted in Figure 4.2. Even in constructing an artificial dataset for region 4 from the already binned data provided by Enderlin2016, a lot of information is missing, particularly in the lower portions of the area range, resulting in a CCDF with large gaps. This makes it difficult to accurately model the shape of the size distribution, despite there being more than the critical number of samples (n ~10^5) required for a statistically significant analysis in the relevant parameter space (*Virkar and Clauset*, 2014). Hence, if the x_{min} value indicated by the power law parameter fitting is used, the result is a nearly vertical line that fits only the overwhelming majority of the

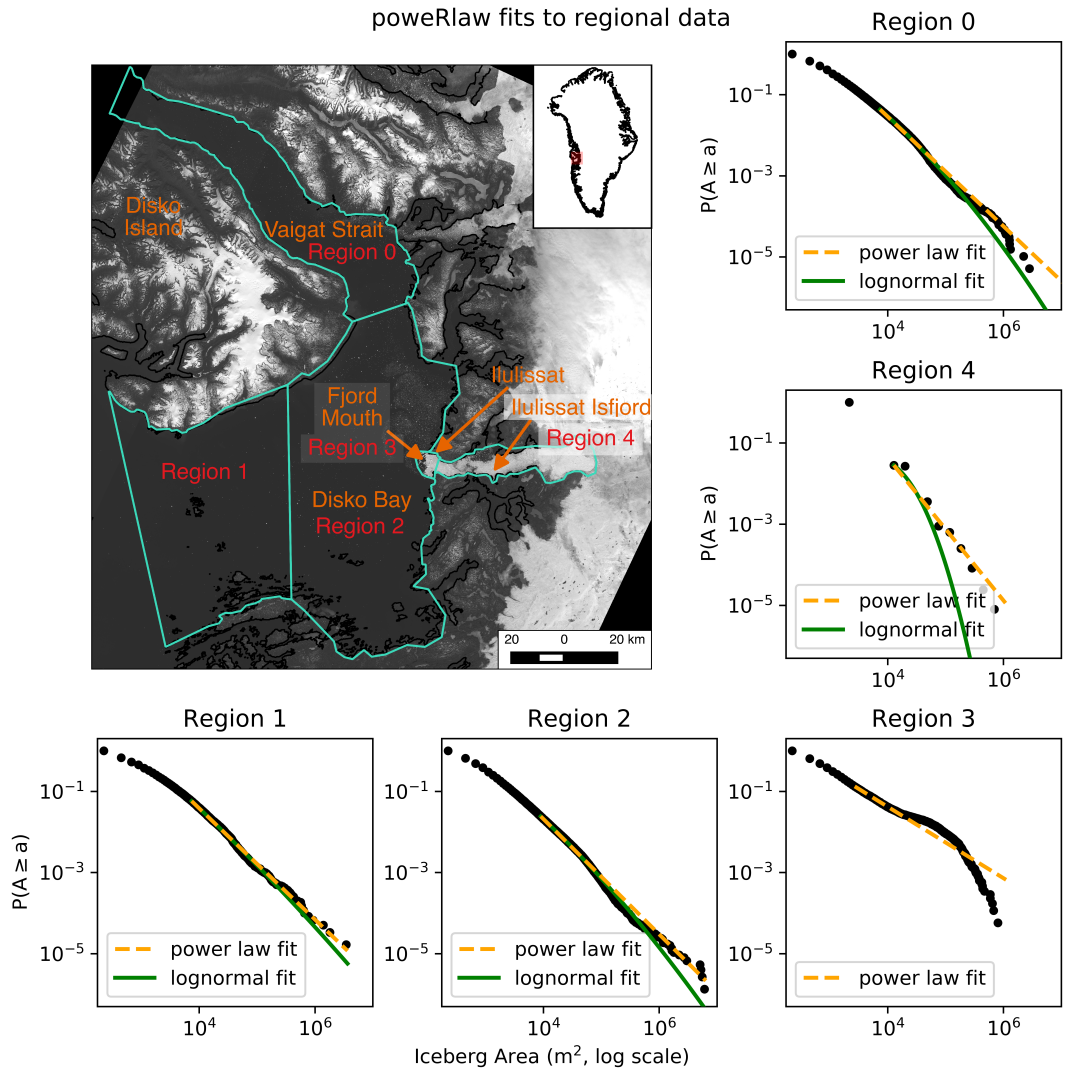

Figure 4.2: Size distribution of icebergs by region. The top left panel shows the regions overlaid on a Landsat panchromatic image mosaic from several dates in 2015. Each plot shows the CCDF for the associated regional dataset with the modeled power law (dashed yellow) and lognormal fits (solid green). See the text for a discussion of which fits are statistically significant and details on the derivation of the dataset used for region 4.

Region	**Power Law**		**Lognormal**			**Observations**		**Comparison**	
	x_{min}	α	x_{min}	μ	β	n	n_{tail}	R	p
0	7425	2.35	99450	−148.14	11.27	193343	8531	−2.78	0.005
1	7425	2.37	99225	−1217.46	33.10	59550	3545	−0.64	0.52
2	9000	2.42	99900	−1021.16	28.03	747372	18682	−2.95	0.003
3	2700	1.88	99900	−1123.04	30.91	17325	2487	2.09	0.04
4	2172	17.10	75851	−75.99	6.63	498494	14026*	−13*	$2.1*10^{-8}$*

*values for model comparison with x_{min} of 12837; see text for more details

Table 4.2: Regional iceberg size distribution fit parameters. Parameters calculated using the R-based poweRlaw package.

dataset that is in the first bin. Thus, to achieve more realistic fits, the models were forced with a slightly higher x_{min} value, and these are the results shown for the comparison statistics in Table 4.2 and fitted curves in Figure 4.2.

In only three of the five regions did the analysis indicate one model provided a better fit. Of these three regions, one (two) followed a power law (lognormal) distribution (regions 3 (0 and 2)). Neither model provided a superior fit in the other regions (1 and 4). The segmented nature of the artificial dataset for region 4 likely explains why neither the power law nor lognormal model had a statistically superior fit, though visual inspection and proximity to the calving front would suggest a power law fit should be preferred over a lognormal fit. The lack of a preferred model for region 1 is puzzling given that the surrounding regions both suggest a lognormal fit. However, none of the significant R values are very far from 0, suggesting that although one model may be superior in those cases, subtle variations in decay processes may readily change the shape of the distribution towards the other model.

The above analysis suffers from several important limitations. First, only three models are considered; these models were chosen based on their previous use in the literature, qualitative inspection of the data, and ease of comparison. However, alternative models not tested in the poweRlaw implementation might provide a superior fit to the data and/or be able to explain a larger portion of the dataset.

Second, the x_{min} values calculated by the algorithm eliminate an overwhelmingly large proportion of the iceberg areas measured (often >50% of the data). This has the important consequences of reducing the likelihood of statistically significant outcomes that generally arise from a large dataset and failing to characterize the full range of data, thereby posing a challenge for the assessment of changes in characteristic iceberg size distributions through space. Third, where lognormal was the preferred model, the software does not enable computation of the statistical significance of the model fit. Thus, it is impossible to determine using these methods whether or not the lognormal fit is statistically valid, even if the parameter uncertainty is small. Together, these limitations suggest that perhaps the power law and lognormal models are too simplistic to represent the proportions of icebergs present across the full range of iceberg sizes. The large number of rare events model may provide a suitable distribution, especially to capture the tail portions of the size distribution curve, which includes the comparatively rare but largest icebergs present in many regions. An alternative approach to fitting one model to the data would be to apply breakpoint regression or a related statistical technique that iteratively tests different models on portions of the data to determine a series of breakpoints within the dataset and fit the most appropriate model to each section of the data. Determining a more robust way to statistically model iceberg size distributions represents an important avenue for future work but is beyond the scope of this dissertation.

In an attempt to address some of the limitations discussed, the iceberg size distributions were also compared using the powerlaw library for Python (*Alstott et al.*, 2014), which is designed to implement the same statistical solutions as the R version but allows the comparison of additional distributions. The companion paper by *Alstott et al.* (2014) also provides a more nuanced discussion for using the package to fit measured size distributions. A comparison of outputs from the

poweRlaw and powerlaw packages for the 31 August 2013 iceberg size distributions confirms the dependence of the fitted parameters on the chosen x_{min} value but otherwise produces similar results. An inspection of the KS values for each possible x_{min} value shows that the absolute minimum chosen by the software is very similar to several other local minima and thus choosing a smaller x_{min} value that includes more of the data is not unreasonable (*Alstott et al.*, 2014). The use of a smaller x_{min} value also does not change the conclusion that neither a power law nor a lognormal distribution provides a better fit to the data. Further, the application of the Python powerlaw library confirms that a stretched exponential (i.e. Weibull) nor an exponential distribution provide a better fit to the data. Carrying this analysis forward to the regional datasets, we arrive at the same conclusions provided the same or similar x_{min} values are used. Namely, regions 0 and 2 (3) are statistically lognormal (power law) fits while regions 1 and 4 are not statistically significantly one model or the other. If instead smaller x_{min} values are used (x_{min}<2,000), regions 1 and 2 effectively swap, with region 2 showing no model preference and region 1 favoring a power law fit. Together, these analyses suggest that the differentiation between power law and lognormal distributions is tenuous and depends not only on the dataset but on the exact methods and x_{min} values used to fit a theoretical function to the data. Further, all of the methods described tend to emphasize characterizing the tail of the distribution, limiting their utility for describing the smallest icebergs in any size distribution, which is arguably where the greatest change in distribution shape occurs.

The challenges associated with finding statistically significant representations of the full range of iceberg sizes in a distribution notwithstanding, inspection of the measured distributions and the models most likely to describe their shape are important indicators of the physical processes governing iceberg decay. *Aström et al.* (2014) describes iceberg calving as a self-organized critical system (SOCS),

wherein instabilities accumulate until the point of failure and these instabilities can be relaxed either through multiple smaller/local events (e.g. calving of a few small pieces of ice) or fewer larger/system-wide events (e.g. ice shelf rifting or large iceberg calving). The behavior of a SOCS is characterized by a perfect power law and these systems exhibit scale invariance, aiding in their identification in natural systems. *Kirkham et al.* (2017) expands on this idea to suggest that the SOCS nature of calving results in a power law iceberg size distribution proximal to the calving front, but as icebergs decay they exhibit a shift towards a lognormal distribution resulting from fracture-based decay mechanisms following the law of proportionate effect. They summarize this law as the result of repeated fracturing and breakage and note that each change in the variable of interest is a random proportion of its prior value, ultimately resulting in an asymptotic lognormal distribution (*Kirkham et al.*, 2017, and references therein). Ultimately, as iceberg size decreases, fracturing decreases, the surface area to volume ratio increases, and melt becomes a more dominant mechanism of mass loss. This results in a proportionately smaller number of the smallest size icebergs relative to near the calving front and supports the aforementioned shift to a non-power law (e.g. lognormal or Weibull) distribution.

An open and interesting avenue for future investigations concerns the extent to which it is possible to use the observed differences in iceberg size distribution and geometric relationships to infer useful properties about the parent glacier and its calving behavior. The fjord/glacier specific draft–width ratio of icebergs indicates the importance of the parent glacier ice thickness and water depth at the terminus, though exactly which geometric parameters are correlated and how that varies among systems remains to be rigorously evaluated. Subsequent to their formation, icebergs are impacted by a number of decay processes that tend to follow varying size distribution models. Thus, the size distribution of icebergs is based on which processes dominate. How quickly the transition from one distribution to another

occurs may provide insight on the various ice and ocean properties driving iceberg decay, including ocean temperatures, bathymetry, and damage accumulation. If changes, including the rate of change, in iceberg size distributions are indicative of damage accumulation in the ice, then this information would also provide valuable insight into the parent glacial ice. Specifically, it provides a relatively easy, inexpensive means to infer damage properties for a large number of marine-terminating tidewater glaciers using remote sensing data. Further, variations in damage accumulation through time, as evidenced by changes in the spatial and temporal patterns of iceberg size distributions, could provide insight on changes in the stress regime of the source glacier due to climatically driven changes such as thinning, acceleration, and meltwater storage.

4.5 Conclusions

The geometry of each iceberg is unique, making broad characterizations of iceberg properties challenging. Despite this uniqueness, iceberg shapes are governed by the physical processes through which they form, making it possible to generate source specific relationships among geometric parameters and pointing towards characteristic size distributions for a collection of icebergs. The subaerial portion of an iceberg lends itself reasonably well to observation, enabling the measurement of iceberg length, width, and freeboard. Although plan view imagery and modern computing techniques enable relatively easy calculation of area for irregularly shaped icebergs, an analysis of the areas and widths obtained by assuming various shapes suggests that iceberg width (area) can vary by as much as 16 (58)% depending on the assumed shape. This indicates the importance of choosing a representative shape based on the parameters of interest, preserving either area (by assuming a square or circle) or variations in width (by assuming a rectangle or ellipse).

Once formed, icebergs decay through a variety of melt and mechanical processes which are dominated by waterline erosion and consequent submarine and subaerial calving. These decay mechanisms result in a collection of icebergs that exhibit characteristic size distributions. Here we find a weak agreement with previous investigations suggesting that icebergs follow a power law distribution near the glacier terminus with a gradual shift towards lognormal distributions as fracture and then melt processes dominate. However, the statistical significance of this relationship is weak, and prior investigations do not provide robust statistical analysis of fitted iceberg size distributions. Thus, alternative models may provide more robust fits to observed iceberg size distributions. Ultimately, the accurate determination of iceberg size distributions and their spatial and temporal variations may provide further insight into the processes governing iceberg decay as well as provide valuable information on the source glaciers and environments in which they break down.

CHAPTER 5
CONCLUSIONS, BROADER IMPLICATIONS, AND FUTURE WORK

Icebergs are an important form of mass loss from the Greenland Ice Sheet and pose a hazard for navigation, infrastructure, and livelihood in the nearshore environment. Additionally, icebergs make the acquisition of *in situ* observations, particularly close to glacier termini, dangerous and in many cases impossible. However, rather than view them as an impediment to observation and navigation, we view icebergs as an underutilized tool to gain insight into the fjords in which they drift and decay, thereby improving our understanding of ice–ocean interactions. Here we presented iceberg-derived datasets that shed insight on the coastal environment and patterns of iceberg presence in coastal waters. The datasets were produced using newly developed methods, which were validated and applied to several fjords around Greenland with a focus on the Ilulissat Isfjord/Disko Bay system in West Greenland.

A primary gap in knowledge concerns the lack of temporally and spatially extensive records of icebergs, including their size, location, and abundance, and how this has changed through time. To address this gap, we developed a semi-automated algorithm to delineate icebergs in optical satellite imagery from the Landsat archive. Clouds are a common occurrence in the Arctic, and their spectral signature in the visible through thermal wavelengths is quite similar to that of snow and ice (i.e. highly reflective and cold). The broad range of possible reflectance values of the two media makes automated discrimination difficult. The novel application of a machine learning technique called multinomial logistic regression resulted in development of a cloud masking scheme that successfully eliminated clouds, even very bright ones missed by other techniques, while mistaking very few icebergs for clouds. This enabled the subsequent extraction of iceberg size distributions from both cloudy and cloud-free imagery, significantly expanding the temporal resolution of the derived

iceberg dataset. The algorithm was applied to six years (2000–2002 and 2013–2015) of the Landsat archive for Disko Bay, a period selected to span important changes in the calving dynamics of the parent glacier, Sermeq Kujalleq (Jakobshavn Isbræ). With the disintegration of its floating ice tongue in the early 2000s, the calving style and energy of Sermeq Kujalleq transitioned from the production of large, tabular icebergs in low energy calving events towards the production of smaller, full thickness icebergs in higher energy calving events. The time series of iceberg size distributions indicates that the change in calving style resulted in an increase in the number of icebergs present in Disko Bay, with a significant portion of those icebergs in the smallest size ranges (~1,800 m^2). As a result of this change, the proportion of ice-covered to open water increased, posing a challenge to navigation. Given the successful application of this algorithm for deriving an iceberg dataset in Disko Bay, future efforts should focus on the application of the algorithm to larger portions of the Landsat archive. This will provide a more complete spatial and temporal record of iceberg size distributions and contribute to our understanding of how iceberg size distributions have changed through time and space as a result of changes in ocean conditions, changes in calving, and ice sheet mass flux.

Bathymetry plays a critical role in controlling the ability of warm waters circulating at depth around Greenland to reach marine glacier termini, driving iceberg, mélange, and terminus melt rates and ultimately influencing fjord circulation and ice dynamics through a series of feedbacks. Despite recent increases in the collection of bathymetry observations, the high resource requirements for collecting these measurements through air- and ship-based means will result in data gaps in present and future bathymetry maps. As a result, it is impossible to assess the influence of changes in subsurface ocean water properties on glacier mass loss due to the presence or absence of bathymetric sills. Icebergs observed in remote sensing datasets are used as drifters to infer both qualitative and quantitative water

depth in order to expand the spatial coverage of available bathymetry data. Relative bathymetric lows and highs are inferred by identifying deep-drafted icebergs as either drifting or stranded, respectively, in sequential satellite imagery. The draft of icebergs stranded in shallow regions places quantitative bounds on the water depth at the stranding site, where draft is calculated based on the assumption of hydrostatic equilibrium applied to iceberg freeboards extracted from DEMs made from very high-resolution stereo image pairs. To expand the spatial coverage of inferred water depths where DEMs of stranded icebergs are limited, fjord specific depth–width ratios are applied to iceberg widths derived from non-stereo optical imagery. Unfortunately, the lack of present knowledge about the shape of the submerged portions of icebergs and their overall mass distribution results in large uncertainties in inferred water depths (on the order of <100 m), limiting the utility of the method in regions where sonar measurements with a higher degree of accuracy are available. However, the method shows promise for constraining gridded bathymetry products, including detecting the presence of bathymetric sills and approximating their height, in previously uncharted fjords or in fjords where terminus retreat has exposed unmapped regions of the seafloor. Thus, future applications of the method in regions unconstrained by observations will provide valuable insight for evaluating asynchronous behavior between neighboring glaciers as well as a means for prioritizing locations where *in situ* observations are still needed.

Iceberg size distributions are driven by the physics governing their formation. Thus, the analysis of iceberg sizes combined with a theoretical understanding of the melt and fracture-based mechanisms of iceberg decay provides insight into the environment in which icebergs decay. Statistically rigorous characterization of the size distribution of icebergs is challenging because of the continual nature of iceberg decay, the probable shift between multiple appropriate model distribution shapes,

the limitations and uncertainties of the available datasets, particularly for the smallest and largest observable icebergs, and the stochasticity contained within this natural system. Despite these challenges, recent efforts have drawn connections between the characteristics of these size distributions and the dominant decay mechanisms. Specifically, the shift from a power law distribution to a lognormal distribution with increasing distance from the calving front is attributed to a shift in decay mechanism dominance from fracture-based to melt-based. A spatial analysis of the datasets derived using the methods presented in this dissertation for the Ilulissat Isfjord–Disko Bay system (i.e. icebergs sourced primarily from Sermeq Kujalleq) generally confirms this pattern. However, challenges associated with differentiating between power law and lognormal distributions in a statistically rigorous way, rather than through visual inspection of fitted curves, makes firm conclusions on any spatial patterns contained in the dataset elusive. Future work to improve characterizations of iceberg size distributions, as well as examination of multiple similar datasets from a larger number of iceberg sources, will likely provide vital information for examining these theories. Ultimately, analysis of spatial and temporal patterns of iceberg size distributions may enable unique insights into the physics governing iceberg decay as well as properties of the parent glacier ice such as damage accumulation.

Although the particulars of this work focus on the coastal environment into which icebergs calve, the implications of the ice–ocean processes discussed have important broader implications that are global in reach. First, the Greenland Ice Sheet contains roughly six meters of global sea level rise equivalent. The rate of mass loss fluctuates on an annual basis, with an overall increase in rates of mass loss in recent decades. A significant proportion of the world's population lives along coastlines, with many regions already severely impacted by rapid sea level rise. Understanding the oceanic forcings on rates of mass loss, including the associated

feedbacks with marine-terminating glacier thinning, acceleration, and retreat, are crucial to improving our predictions of future rates of sea level rise, thereby enabling appropriate adaptation strategies and regional planning. Second, geopolitical interest in Arctic development, including natural resource development and the establishment of trans-Arctic shipping lanes, is increasing as more of the Arctic remains ice free for substantial portions of each year. Icebergs, particularly those large enough to cause damage to infrastructure and vessels but difficult to detect, track, and predict the movements of, pose a critical hazard to any Arctic operations. This risk applies to both human life and delicate, changing Arctic ecosystems, and care must be taken to develop effective communication and risk mitigation systems at a pace that matches the scale of increased shipping and development. Third, and most likely of direct relevance to Maine, is the influence of icebergs on distributed freshwater flux and the subsequent impacts to ocean circulation and ecosystems. The waters circulating in the Gulf of Maine are impacted by the Atlantic Meriodional Overturning Circulation (AMOC), which is driven in part by freshwater fluxes from Greenland. Changes in AMOC thus have implications for the water properties in the Gulf, which in turn influences the local ecosystems and fisheries upon which the state relies.

Icebergs are a critical component of the ice–ocean system. The work presented herein developed several important methods and illustrated their application for using icebergs observed in remote sensing imagery as a means to derive valuable datasets and provide insights into the ice–ocean environment. Specifically, we automatically extracted iceberg size distributions for several years and linked changes in size distributions to changes in calving style of the parent glacier, inferred bathymetry using icebergs as depth sounders, and explored the use of spatial changes in size distribution as a means to investigate processes of iceberg decay and parent glacier properties.

REFERENCES

Alstott, J., E. Bullmore, and D. Plenz (2014), powerlaw: A python package for analysis of heavy-tailed distributions, *PLOS ONE*, *9*(1), doi:10.1371/journal.pone.0085777.

Amundson, J. M., M. Truffer, M. P. Lüthi, M. Fahnestock, M. West, and R. J. Motyka (2008), Glacier, fjord, and seismic response to recent large calving events, Jakobshavn Isbræ, Greenland, *Geophys. Res. Lett.*, *35*(22), L22,501, doi:10.1029/2008GL035281.

Asiaq, Greenland Survey (2014), Coastline, personal communication.

Aström, J. A., D. Vallot, M. Schäfer, E. Z. Welty, S. O'Neel, T. C. Bartholomaus, Y. Liu, T. I. Riikilä, T. Zwinger, J. Timonen, and J. C. Moore (2014), Termini of calving glaciers as self-organized critical systems, *Nat. Geosci.*, *7*, 874–878, doi:10.1038/ngeo2290.

Bamber, J., M. van den Broeke, J. Ettema, J. Lenaerts, and E. Rignot (2012), Recent large increases in freshwater fluxes from Greenland into the North Atlantic, *Geophys. Res. Lett.*, *39*(19), doi:10.1029/2012GL052552.

Bassis, J. N., and S. Jacobs (2013), Diverse calving patterns linked to glacier geometry, *Nat. Geosci.*, *6*(10), 833–836, doi:10.1038/ngeo1887.

Benn, D. I., C. R. Warren, and R. H. Mottram (2007), Calving processes and the dynamics of calving glaciers, *Earth-Sci. Rev.*, *82*(3-4), 143–179, doi:10.1016/j.earscirev.2007.02.002.

Benn, D. I., J. Åström, T. Zwinger, J. Todd, F. M. Nick, S. Cook, N. R. J. Hulton, and A. Luckman (2017), Melt-under-cutting and buoyancy-driven calving from tidewater glaciers : new insights from discrete element and continuum model simulations, *J. Glaciol.*, *63*(240), 691–702, doi:10.1017/jog.2017.41.

Bigg, G. R., M. R. Wadley, D. P. Stevens, and J. A. Johnson (1997), Modelling the dynamics and thermodynamics of icebergs, *Cold Reg. Sci. Technol.*, *26*, 113–135.

Bigg, G. R., H. L. Wei, D. J. Wilton, Y. Zhao, S. A. Billings, E. Hanna, and V. Kadirkamanathan (2014), A century of variation in the dependence of Greenland iceberg calving on ice sheet surface mass balance and regional climate change, *P. Roy. Soc. A-Math. Phy.*, *470*(2166), doi:10.3189/002214311796905631.

Bindschadler, R. (1998), Monitoring ice sheet behavior from space, *Rev. Geophys.*, *36*(1), 79–104.

Bondzio, J. H., M. Morlighem, H. Seroussi, T. Kleiner, M. Rückamp, J. Mouginot, T. Moon, E. Y. Larour, and A. Humbert (2017), The mechanisms behind

Jakobshavn Isbræ's acceleration and mass loss: A 3-D thermomechanical model study, *Geophys. Res. Lett.*, *44*(12), 6252–6260, doi:10.1002/2017GL073309.

Burton, J. C., J. M. Amundson, D. S. Abbot, A. Boghosian, L. M. Cathles, S. Correa-Legisos, K. N. Darnell, N. Guttenberg, D. M. Holland, and D. R. MacAyeal (2012), Laboratory investigations of iceberg capsize dynamics, energy dissipation and tsunamigenesis, *J. Geophys. Res.-Earth*, *117*(1), 1–13, doi:10.1029/2011JF002055.

Carroll, D., D. A. Sutherland, E. L. Shroyer, J. D. Nash, G. A. Catania, and L. A. Stearns (2017), Subglacial discharge-driven renewal of tidewater glacier fjords, *J. Geophys. Res.-Oceans*, *122*, 6611–6629, doi:10.1002/2017JC012962.

Cassotto, R., M. Fahnestock, J. M. Amundson, M. Truffer, and I. Joughin (2015), Seasonal and interannual variations in ice melange and its impact on terminus stability, Jakobshavn Isbræ, Greenland, *J. Glaciol.*, *61*(225), 76–88, doi:10.3189/2015JoG13J235.

Chauché, N., A. Hubbard, J. C. Gascard, J. E. Box, R. Bates, M. Koppes, A. Sole, P. Christoffersen, and H. Patton (2014), Ice-ocean interaction and calving front morphology at two west Greenland tidewater outlet glaciers, *The Cryosphere*, *8*(4), 1457–1468, doi:10.5194/tc-8-1457-2014.

Christoffersen, P., R. I. Mugford, K. J. Heywood, I. Joughin, J. A. Dowdeswell, J. P. M. Syvitski, A. Luckman, and T. J. Benham (2011), Warming of waters in an East Greenland fjord prior to glacier retreat: mechanisms and connection to large-scale atmospheric conditions, *The Cryosphere*, *5*(3), 701–714, doi:10.5194/tc-5-701-2011.

Chu, V. W., L. C. Smith, A. K. Rennermalm, R. R. Forster, J. E. Box, and N. Reeh (2009), Sediment plume response to surface melting and supraglacial lake drainages on the Greenland Ice Sheet, *J. Glaciol.*, *55*(194), 1072–1082, doi:10.3189/002214309790794904.

Clauset, A., C. R. Shalizi, and M. E. J. Newman (2009), Power-law distributions in empirical data, *SIAM Review*, *51*, 661–703, doi:10.1109/ICPC.2008.18.

Dowdeswell, J. A., and C. F. Forsberg (1992), The size and frequency of icebergs and bergy bits derived from tidewater glaciers in Kongsfjorden, northwest Spitsbergen, *Polar Res.*, *11*(2), 81–91.

Dowdeswell, J. A., R. J. Whittington, and R. Hodgkins (1992), The sizes, frequencies, and freeboards of east Greenland icebergs observed using ship radar and sextant, *J. Geophys. Res.*, *97*, 3515–3528.

Dozier, J. (1989), Spectral signature of alpine snow cover from the Landsat Thematic Mapper, *Remote Sens. Environ.*, *28*, 9–22.

Echelmeyer, K., T. S. Clarke, and W. D. Harrison (1991), Surficial glaciology of Jakobshavns Isbræ, West Greenland: Part I. surface morphology, *J. Glaciol.*, *37*(127), 368–382, doi:10.3189/S0022143000005803.

El-Tahan, M., and H. El-Tahan (1982), Estimation of iceberg draft, *IEEE*, pp. 689–695.

Enderlin, E. M., and G. S. Hamilton (2014), Estimates of iceberg submarine melting from high-resolution digital elevation models: application to Sermilik Fjord, east Greenland, *J. Glaciol.*, *60*(224), 1084–1092, doi:10.3189/2014JoG14J085.

Enderlin, E. M., I. M. Howat, S. Jeong, M.-J. Noh, J. H. van Angelen, and M. R. van den Broeke (2014), An improved mass budget for the Greenland ice sheet, *Geophys. Res. Lett.*, *41*, 1–7, doi:10.1002/2013GL059010.

Enderlin, E. M., G. S. Hamilton, F. Straneo, and D. A. Sutherland (2016), Iceberg meltwater fluxes dominate the freshwater budget in Greenland's iceberg-congested glacial fjords, *Geophys. Res. Lett.*, *43*(11), 287–294, doi:10.1002/2016GL070718.

Enderlin, E. M., C. J. Carrigan, W. H. Kochtitzky, A. Cuadros, T. Moon, and G. S. Hamilton (2018), Greenland iceberg melt variability from high-resolution satellite observations, *The Cryosphere*, *12*, 565–575, doi:10.5194/tc-12-565-2018.

Fenty, I., J. Willis, A. Khazendar, S. Dinardo, R. Forsberg, I. Fukumori, D. Holland, M. Jakobsson, D. Moller, J. Morison, A. Münchow, E. Rignot, M. Schodlok, A. Thompson, K. Tinto, M. Rutherford, and N. Trenholm (2016), Oceans Melting Greenland: Early results from NASA's ocean-ice mission in Greenland, *Oceanography*, *29*(4), 72–83, doi:10.5670/oceanog.2016.100.

Fichefet, T., C. Poncin, H. Goosse, P. Huybrechts, I. Janssens, and H. Le Treut (2003), Implications of changes in freshwater flux from the Greenland ice sheet for the climate of the 21st century, *Geophys. Res. Lett.*, *30*(17), doi:10.1029/2003GL017826.

FitzMaurice, A., F. Straneo, C. Cenedese, and M. Andres (2016), Effect of a sheared flow on iceberg motion and melting, *Geophys. Res. Lett.*, *43*, 1–8, doi:10.1002/2016GL071602.

FitzMaurice, A., C. Cenedese, and F. Straneo (2017), Nonlinear response of iceberg side melting to ocean currents, *Geophys. Res. Lett.*, *44*(11), 5637–5644, doi:10.1002/2017GL073585.

Foga, S., P. L. Scaramuzza, S. Guo, Z. Zhu, R. D. Dilley, Jr, T. Beckmann, G. L. Schmidt, J. L. Dwyer, M. J. Hughes, and B. Laue (2017), Cloud detection algorithm comparison and validation for operational Landsat data products, *Remote Sens. Environ.*, *194*(C), 379–390, doi:10.1016/j.rse.2017.03.026.

Gillespie, C. (2015), Fitting heavy tailed distributions: the poweRlaw package, *Jo. Stat. Softw.*, *64*(2), 257–266.

Gladish, C. V., D. M. Holland, A. Rosing-Asvid, J. W. Behrens, and J. Boje (2015), Oceanic boundary conditions for Jakobshavn Glacier. Part I: variability and renewal of Ilulissat Icefjord waters, 2001–14, *J. Phys. Oceanogr.*, *45*(1), 3–32, doi:10.1175/JPO-D-14-0044.s1.

Gladstone, R. M., G. R. Bigg, and K. W. Nicholls (2001), Iceberg trajectory modeling and meltwater injection in the Southern Ocean, *J. Geophys. Res.-Oceans*, *106*(C9), 19,903–19,915.

Greene, C. H., A. J. Pershing, T. M. Cronin, and N. Ceci (2008), Arctic climate change and its impacts on the ecology of the North Atlantic, *Ecology*, *89*(sp11), S24–S38, doi:10.1890/07-0550.1.

Hall, D. K., G. A. Riggs, and V. V. Salomonson (1995), Development of methods for mapping global snow cover using moderate resolution imaging spectroradiometer data, *Remote Sens. Environ.*, *54*(2), 127–140, doi:10.1016/0034-4257(95)00137-P.

Holland, D. M., R. H. Thomas, B. de Young, M. H. Ribergaard, and B. Lyberth (2008), Acceleration of Jakobshavn Isbræ triggered by warm subsurface ocean waters, *Nat. Geosci.*, *1*(10), 659–664, doi:10.1038/ngeo316.

Hotzel, S. I., and J. D. Miller (1983), Icebergs: their physical dimensions and the presentation and application of measured data, *Ann. Glaciol.*, *4*, 116–123.

Hughes, M. J., and D. J. Hayes (2014), Automated detection of cloud and cloud shadow in single-date Landsat imagery using neural networks and spatial post-processing, *Remote Sensing*, *6*(6), 4907–4926, doi:10.3390/rs6064907.

Irish, R. R., J. L. Barker, S. N. Goward, and T. Arvidson (2006), Characterization of the Landsat-7 ETM Automated Cloud-Cover Assessment (ACCA) algorithm, *Photogramm. Eng. Rem. S.*, *72*, 1179–1188, doi:10.14358/PERS.72.10.1179.

Jakobsson, M., L. Mayer, B. Coakley, J. A. Dowdeswell, S. Forbes, B. Fridman, H. Hodnesdal, R. Noormets, R. Pedersen, M. Rebesco, H. W. Schenke, Y. Zarayskaya, D. Accettella, A. Armstrong, R. M. Anderson, P. Bienhoff, A. Camerlenghi, I. Church, M. Edwards, J. V. Gardner, J. K. Hall, B. Hell, O. Hestvik, Y. Kristoffersen, C. Marcussen, R. Mohammad, D. Mosher, S. V. Nghiem, M. T. Pedrosa, P. G. Travaglini, and P. Weatherall (2012), The

International Bathymetric Chart of the Arctic Ocean (IBCAO) Version 3.0, *Geophys. Res. Lett.*, *39*(12), doi:10.1029/2012GL052219.

Jedlovec, G. (2009), Automated detection of clouds in satellite imagery, in *Advances in Geoscience and Remote Sensing*, edited by G. Jedlovec, Intech.

Johnson, H. L., A. Münchow, K. K. Falkner, and H. Melling (2011), Ocean circulation and properties in Petermann Fjord, Greenland, *J. Geophys. Res.*, *116*(C01003), doi:10.1029/2010JC006519.

Joughin, I., W. Abdalati, and M. Fahnestock (2004), Large fluctuations in speed on Greenland's Jakobshavn Isbræ glacier, *Nature*, *432*(7017), 608–610.

Joughin, I., I. M. Howat, M. Fahnestock, B. Smith, W. Krabill, R. B. Alley, H. Stern, and M. Truffer (2008), Continued evolution of Jakobshavn Isbrae following its rapid speedup, *J. Geophys. Res.*, *113*(F04006), doi:10.1029/2008JF001023.

Joughin, I., B. E. Smith, I. M. Howat, D. Floricioiu, R. B. Alley, M. Truffer, and M. Fahnestock (2012), Seasonal to decadal scale variations in the surface velocity of Jakobshavn Isbræ, Greenland: observation and model-based analysis, *J. Geophys. Res.*, *117*(F2), F02,030, doi:10.1029/2011JF002110.

Joughin, I., B. E. Smith, D. E. Shean, and D. Floricioiu (2014), Brief Communication: Further summer speedup of Jakobshavn Isbræ, *The Cryosphere*, *8*(1), 209–214, doi:10.5194/tc-8-209-2014.

Kirkham, J. D., N. J. Rosser, J. Wainwright, E. C. V. Jones, S. A. Dunning, V. S. Lane, D. E. Hawthorn, M. C. Strzelecki, and W. Szczuciński (2017), Drift-dependent changes in iceberg size-frequency distributions, *Nature*, *7*(15991), 1–10.

Kjeldsen, K. K., J. Mortensen, J. Bendtsen, D. Petersen, K. Lennert, and S. Rysgaard (2014), Ice-dammed lake drainage cools and raises surface salinities in a tidewater outlet glacier fjord, West Greenland, *J. Geophys. Res.-Earth*, *119*, 1310–1320, doi:10.1002/(ISSN)2169-9011.

König, M., J. G. Winther, and E. Isaksson (2001), Measuring snow and glacier ice properties from satellite, *Rev. Geophys.*, *39*(1), 1–27.

Krimmel, R. M., and M. F. Meier (1975), Glacier applications of ERTS images, *J. Glaciol.*, *15*(72), 391–402.

Kustiyo, Dianovita, H. Ismaya, M. I. Rahayu, and E. S. Adiningsih (2012), New automated cloud and cloud-shadow detection using Landsat imagery, *International Journal of Remote Sensing and Earth Sciences*, *9*, 100–111.

Lee, J., R. C. Weger, S. K. Sengupta, and R. M. Welch (1990), A neural network approach to cloud classification, *IEEE T. Geosci. Remote*, *28*(5), 846–855.

Luckman, A., and T. Murray (2005), Seasonal variation in velocity before retreat of Jakobshavn Isbræ, Greenland, *Geophys. Res. Lett.*, *32*(L08501), 1–4, doi:10.1029/2005GL022519.

McFadden, E. M., I. M. Howat, I. Joughin, B. E. Smith, and Y. Ahn (2011), Changes in the dynamics of marine terminating outlet glaciers in west Greenland (2000–2009), *J. Geophys. Res.*, *116*(F02022), doi:10.1029/2010JF001757.

McGuire, P., A. Younan, Y. Wang, J. Bruce, M. Gandi, T. King, K. Keeping, and K. Regular (2016), OTC 27473 Smart Iceberg Management System – Rapid Iceberg Profiling System, *Tech. rep.*

McKenna, R. (2005), Refinement of iceberg shape characterization for risk to Grand Banks installations, *Tech. Rep. 20-77*, doi:10.4224/12328384.

Millan, R., E. Rignot, J. Mouginot, M. Wood, A. A. Bjørk, and M. Morlighem (2018), Vulnerability of Southeast Greenland glaciers to warm Atlantic water from Operation IceBridge and Ocean Melting Greenland data, *Geophys. Res. Lett.*, *45*, 2688–2696, doi:10.1002/2017GL076561.

Moon, T., and I. Joughin (2008), Changes in ice front position on Greenland's outlet glaciers from 1992 to 2007, *J. Geophys. Res.*, *113*(F02022), doi:10.1029/2007JF000927.

Moon, T., D. A. Sutherland, D. Carroll, D. Felikson, L. Kehrl, and F. Straneo (2018), Subsurface iceberg melt key to Greenland fjord freshwater budget, *Nat. Geosci.*, doi:10.1038/s41561-017-0018-z.

Morlighem, M., C. N. Williams, E. Rignot, L. An, J. E. Arndt, J. L. Bamber, G. Catania, N. Chauché, J. A. Dowdeswell, B. Dorschel, I. Fenty, K. Hogan, I. Howat, A. Hubbard, M. Jakobsson, T. M. Jordan, K. K. Kjeldsen, R. Millan, L. Mayer, J. Mouginot, B. P. Y. Noël, C. O'Cofaigh, S. Palmer, S. Rysgaard, H. Seroussi, M. J. Siegert, P. Slabon, F. Straneo, M. R. van den Broeke, W. Weinrebe, M. Wood, and K. B. Zinglersen (2017a), BedMachine v3: Complete bed topography and ocean bathymetry mapping of Greenland from multibeam echo sounding combined with mass conservation, *Geophys. Res. Lett.*, *44*(21), 11,051–11,061.

Morlighem, M., et al. (2017b), IceBridge BedMachine Greenland, Version 3. Bathymetry., doi:10.5067/2CIX82HUV88Y, dataset accessed [2018-06-07].

Mortensen, J., K. Lennert, J. Bendtsen, and S. Rysgaard (2011), Heat sources for glacial melt in a sub-Arctic fjord (Godthåbsfjord) in contact with the Greenland

ice sheet, *J. Geophys. Res.*, *116*(1), 1–13, doi:10.1029/2010JC006528.

Mugford, R. I., and J. A. Dowdeswell (2010), Modeling iceberg-rafted sedimentation in high-latitude fjord environments, *Journal of Geophysical Research*, *115*(F3), 1–21, doi:10.1007/978-3-662-04439-1_11.

Münchow, A., L. Padman, and H. A. Fricker (2014), Interannual changes of the floating ice shelf of Petermann Gletscher, North Greenland, from 2000 to 2012, *J. Glaciol.*, *60*(221), 489–499, doi:10.3189/2014JoG13J135.

Murray, T., N. Selmes, T. D. James, S. Edwards, I. Martin, T. O'Farrell, R. Aspey, I. Rutt, M. Nettles, and T. Baugé (2015), Dynamics of glacier calving at the ungrounded margin of Helheim Glacier, southeast Greenland, *J. Geophys. Res.-Earth*, *120*(6), 964–982, doi:10.1002/2015JF003531.

Nick, F. M., A. Vieli, I. M. Howat, and I. Joughin (2009), Large-scale changes in Greenland outlet glacier dynamics triggered at the terminus, *Nat. Geosci.*, *2*(2), 110–114, doi:10.1038/ngeo394.

O'Leary, M., and P. Christoffersen (2013), Calving on tidewater glaciers amplified by submarine frontal melting, *The Cryosphere*, *7*, 119–128, doi:10.5194/tc-7-119-2013.

OMG Mission (2016a), Conductivity, temperature and depth (ctd) data from the ocean survey. Ver. 0.1, doi:10.5067/OMGEV-AXCTD, dataset accessed [2018-05-23].

OMG Mission (2016b), Bathymetry (sea floor depth) data from the ship-based bathymetry survey. Ver. 0.1., doi:10.5067/OMGEV-BTYSS, dataset accessed [2017-09-29].

Oreopoulos, L., M. J. Wilson, and T. Várnai (2011), Implementation on Landsat data of a simple cloud-mask algorithm developed for MODIS land bands, *IEEE Geosci. Remote S.*, *8*(4), 597–601, doi:10.1109/LGRS.2010.2095409.

Orheim, O. (1980), Physical characteristics and life expectancy of tabular Antarctic icebergs, *Ann. Glaciol*, *1*, 11–18.

Padman, L., and S. Erofeeva (2004), A barotropic inverse tidal model for the Arctic Ocean, *Geophys. Res. Lett.*, *31*(2), doi:10.1029/2003GL019003.

Pedregosa, F., G. Varoquaux, A. Gramfort, V. Michel, B. Thirion, O. Grisel, M. Blondel, P. Prettenhofer, R. Weiss, V. Dubourg, J. Vanderplas, A. Passos, D. Cournapeau, M. Brucher, M. Perrot, and E. Duchesnay (2011), Scikit-learn: machine learning in Python, *J. Mach. Learn. Res.*, *12*, 2825–2830.

Pizzolato, L., S. E. L. Howell, C. Derksen, J. Dawson, and L. Copland (2014), Changing sea ice conditions and marine transportation activity in Canadian Arctic waters between 1990 and 2012, *Climatic Change*, *123*(2), 161–173, doi:10.1007/s10584-013-1038-3.

Podrasky, D., M. Truffer, M. Lüthi, and M. Fahnestock (2014), Quantifying velocity response to ocean tides and calving near the terminus of Jakobshavn Isbrae, Greenland, *J. Glaciol.*, *60*(222), 609–621, doi:10.3189/2014JoG13J130.

QGIS Development Team (2017), *QGIS Geographic Information System*, Open Source Geospatial Foundation Project.

R Core Team (2018), *R: A Language and Environment for Statistical Computing*, R Foundation for Statistical Computing, Vienna, Austria.

Racoviteanu, A. E., F. Paul, B. Raup, S. J. S. Khalsa, and R. Armstrong (2009), Challenges and recommendations in mapping of glacier parameters from space: results of the 2008 Global Land Ice Measurements from Space (GLIMS) workshop, Boulder, Colorado, USA, *Ann. Glaciol.*, *50*(53), 53–69, doi:10.3189/172756410790595804.

Raup, B. H., H. H. Kieffer, T. M. Hare, and J. Kargel (2000), Generation of data acquisitions requests for the ASTER satellite instrument for monitoring a globally distributed target: glaciers, *IEEE T. Geosci. Remote*, *38*(2), 1–10.

Riggs, G. A., and D. K. Hall (2002), Reduction of cloud obscuration in the MODIS snow data product, in *59th Eastern Snow Conference*, pp. 205–212, Stowe, VT.

Rignot, E., and P. Kanagaratnam (2006), Changes in the Velocity Structure of the Greenland Ice Sheet, *Science*, *311*(5763), 986–990, doi:10.1126/science.1121381.

Rignot, E., I. Velicogna, M. R. van den Broeke, A. Monaghan, and J. T. M. Lenaerts (2011), Acceleration of the contribution of the Greenland and Antarctic ice sheets to sea level rise, *Geophys. Res. Lett.*, *38*(5), doi:10.1029/2011GL046583.

Rignot, E., I. Fenty, D. Menemenlis, and Y. Xu (2012), Spreading of warm ocean waters around Greenland as a possible cause for glacier acceleration, *Ann. Glaciol.*, *53*(60), 257–266, doi:10.3189/2012AoG60A136.

Rignot, E., I. Fenty, Y. Xu, C. Cai, I. Velicogna, C. O. Cofaigh, J. A. Dowdeswell, W. Weinrebe, G. Catania, and D. Duncan (2016), Bathymetry data reveal glaciers vulnerable to ice-ocean interaction in Uummannaq and Vaigat glacial fjords, west Greenland, *Geophys. Res. Lett.*, *43*, 2667–2674, doi:10.1002/(ISSN)1944-8007.

Romanov, Y. A., N. A. Romanova, and P. Romanov (2011), Shape and size of Antarctic icebergs derived from ship observation data, *Antarct. Sci.*, *24*(01),

77–87, doi:10.1017/S0954102011000538.

Rosenau, R., M. Scheinert, and R. Dietrich (2015), A processing system to monitor Greenland outlet glacier velocity variations at decadal and seasonal time scales utilizing the Landsat imagery, *Remote Sens. Environ.*, *169*, 1–19, doi:10.1016/j.rse.2015.07.012.

Savage, S. (2001), *Aspects of Iceberg Deterioration and Drift*, chap. 12, pp. 279–318, Springer Berlin Heidelberg, Berlin, Heidelberg, doi:10.1007/3-540-45670-8.

Savage, S. B., G. B. Crocker, M. Sayed, and T. Carrieres (2000), Size distributions of small ice pieces calved from icebergs, *Cold Reg. Sci. Technol.*, *31*(2), 163–172.

Scambos, T., O. Sergienko, A. Sargent, D. MacAyeal, and J. Fastook (2005), ICESat profiles of tabular iceberg margins and iceberg breakup at low latitudes, *Geophys. Res. Lett.*, *32*(23), 1–4, doi:10.1029/2005GL023802.

Scambos, T., R. Ross, R. Bauer, Y. Yermolin, P. Skvarca, D. Long, J. Bohlander, and T. Haran (2008), Calving and ice-shelf break-up processes investigated by proxy: Antarctic tabular iceberg evolution during northward drift, *J. Glaciol.*, *54*(187), 579–591, doi:10.3189/002214308786570836.

Scambos, T. A., M. J. Dutkiewicz, J. C. Wilson, and R. A. Bindschadler (1992), Application of image cross-correlation to the measurement of glacier velocity using satellite image data, *Remote Sens. Environ.*, *42*, 177–186, doi:10.1016/0034-4257(92)90101-O.

Scaramuzza, P. L., M. A. Bouchard, and J. L. Dwyer (2012), Development of the Landsat Data Continuity Mission Cloud-Cover Assessment algorithms, *IEEE T. Geosci. Remote*, *50*(4), 1140–1154, doi:10.1109/TGRS.2011.2164087.

Schaffer, J., R. Timmerman, J. E. Arndt, S. S. Kristensen, C. Mayer, M. Morlighem, and D. Steinhage (2016), A global, high-resolution data set of ice sheet topography, cavity geometry, and ocean bathymetry, *Earth Syst. Sci. Data*, *8*, 543–557, doi:10.1594/PANGAEA.856844.

Schumann, K., D. Völker, and W. R. Weinrebe (2012), Acoustic mapping of the Ilulissat Ice Fjord mouth, West Greenland, *Quaternary Sci. Rev.*, *40*(C), 78–88, doi:10.1016/j.quascirev.2012.02.016.

Schumann, K., et al. (2011), Gridded results of swath bathymetric mapping of Disko Bay, western Greenland, 2007-2008, doi:10.1594/PANGAEA.770250, dataset accessed [2016-11-29].

Shean, D. E., O. Alexandrov, Z. M. Moratto, B. E. Smith, I. R. Joughin, C. Porter, and P. Morin (2016), An automated, open-source pipeline for mass production of

digital elevation models (DEMs) from very-high-resolution commercial stereo satellite imagery, *ISPRS J. Photogramm.*, *116*(C), 101–117, doi:10.1016/j.isprsjprs.2016.03.012.

Silva, T. A. M., G. R. Bigg, and K. W. Nicholls (2006), Contribution of giant icebergs to the Southern Ocean freshwater flux, *J. Geophys. Res.*, *111*(C03004), doi:10.1029/2004JC002843.

Sneed, W. A., and G. S. Hamilton (2007), Evolution of melt pond volume on the surface of the Greenland Ice Sheet, *Geophys. Res. Lett.*, *34*(3), 4–7, doi:10.1029/2006GL028697.

Storey, J., M. Choate, and K. Lee (2014), Landsat 8 operational land imager on-orbit geometric calibration and performance, *Remote Sensing*, *6*(11), 11,127–11,152, doi:10.3390/rs61111127.

Straneo, F., and P. Heimbach (2013), North Atlantic warming and the retreat of Greenland's outlet glaciers, *Nature*, *504*(7478), 36–43, doi:10.1038/nature12854.

Straneo, F., G. S. Hamilton, D. A. Sutherland, L. A. Stearns, F. Davidson, M. O. Hammill, G. B. Stenson, and A. Rosing-Asvid (2010), Rapid circulation of warm subtropical waters in a major glacial fjord in East Greenland, *Nat. Geosci.*, *3*(3), 182–186, doi:10.1038/ngeo764.

Straneo, F., R. G. Curry, D. A. Sutherland, G. S. Hamilton, C. Cenedese, K. Våge, and L. A. Stearns (2011), Impact of fjord dynamics and glacial runoff on the circulation near Helheim Glacier, *Nat. Geosci.*, *4*(5), 322–327, doi:10.1038/ngeo1109.

Straneo, F., D. A. Sutherland, D. Holland, C. Gladish, G. S. Hamilton, H. L. Johnson, E. Rignot, Y. Xu, and M. Koppes (2012), Characteristics of ocean waters reaching Greenland's glaciers, *Ann. Glaciol.*, *53*(60), 202–210, doi:10.3189/2012AoG60A059.

Sulak, D. J., D. A. Sutherland, E. M. Enderlin, L. A. Stearns, and G. S. Hamilton (2017), Iceberg properties and distributions in three Greenlandic fjords using satellite imagery, *Ann. Glaciol.*, pp. 1–15, doi:10.1017/aog.2017.5.

Sutherland, D. A., F. Straneo, and R. S. Pickart (2014a), Characteristics and dynamics of two major Greenland glacial fjords, *J. Geophys. Res.-Oceans*, *119*(6), 3767–3791, doi:10.1002/2013JC009786.

Sutherland, D. A., G. E. Roth, G. S. Hamilton, S. H. Mernild, L. A. Stearns, and F. Straneo (2014b), Quantifying flow regimes in a Greenland glacial fjord using iceberg drifters, *Geophys. Res. Lett.*, *41*, 8411–8420, doi:10.1002/(ISSN)1944-8007.

Thomas, R., and M. Studinger (2010), Pre-IceBridge ATM L2 Icessn elevation, slope, and roughness, Version 1. elevation., doi:10.5067/6C6WA3R918HJ, date accessed [2018-09-12].

Todd, J., P. Christoffersen, T. Zwinger, P. Råback, N. Chauché, D. Benn, A. Luckman, J. Ryan, N. Toberg, D. Slater, and A. Hubbard (2018), A full-Stokes 3-D calving model applied to a large Greenlandic glacier, *J. Geophys. Res.-Earth*, *123*, 410–432, doi:10.1002/2017JF004349.

Tournadre, J., F. Girard-Ardhuin, and B. Legrésy (2012), Antarctic icebergs distributions, 2002–2010, *J. Geophys. Res.*, *117*(C05004), doi:10.1029/2011JC007441.

Van den Broeke, M., J. Bamber, J. Ettema, E. Rignot, E. Schrama, W. J. van de Berg, E. van Meijgaard, I. Velicogna, and B. Wouters (2009), Partitioning recent Greenland mass loss, *Science*, *326*(5955), 984–986, doi:10.1126/science.1178176.

van der Veen, C. J. (1998), Fracture mechanics approach to penetration of surface crevasses on glaciers, *Cold Reg. Sci. Technol.*, *27*(1), 31–47.

Vieli, A., and F. M. Nick (2011), Understanding and modelling rapid dynamic changes of tidewater outlet glaciers: Issues and implications, *Surv. Geophys.*, *32*, 437–458, doi:10.1007/s10712-011-9132-4.

Virkar, Y., and A. Clauset (2014), Power-law distributions in binned empirical data, *Ann. Appl. Stat.*, *8*(1), 89–119, doi:10.1214/13-AOAS710.

Wagner, T. J. W., P. Wadhams, R. Bates, P. Elósegui, A. Stern, D. Vella, E. P. Abrahamsen, A. Crawford, and K. W. Nicholls (2014), The "footloose" mechanism: Iceberg decay from hydrostatic stresses, *Geophys. Res. Lett.*, *41*(15), 5522–5529.

Wagner, T. J. W., A. A. Stern, R. W. Dell, and I. Eisenman (2017), On the representation of capsizing in iceberg models, *Ocean Model.*, *117*, 88–96, doi:10.1016/j.ocemod.2017.07.003.

Warren, S. G. (1982), Optical properties of snow, *Rev. Geophys.*, *20*(1), 67–89.

Williams, C. N., S. L. Cornford, T. M. Jordan, J. A. Dowdeswell, M. J. Siegert, C. D. Clark, D. A. Swift, A. Sole, I. Fenty, and J. L. Bamber (2017), Generating synthetic fjord bathymetry for coastal Greenland, *The Cryosphere*, *11*(1), 363–380, doi:10.5194/tc-11-363-2017.

Zhu, Z., and C. E. Woodcock (2012), Object-based cloud and cloud shadow detection in Landsat imagery, *Remote Sens. Environ.*, *118*(C), 83–94, doi:10.1016/j.rse.2011.10.028.

BIOGRAPHY OF THE AUTHOR

Jessica Scheick was born in Trenton, NJ. She attended Ewing High School and in May 2009 graduated with an A.B., *magna cum laude*, in geology and mathematics from Bryn Mawr College in Pennsylvania. After graduation she worked for an environmental consulting firm, conducting remedial investigations and ongoing monitoring at a variety of contaminated sites. The most notable of these sites saw her boating in the phragmites and mud filled marshes of North Jersey, where she was well known as an eager participant in winter fieldwork given her love of all things snow and ice (and cold). Prior to and since beginning her graduate studies, she regularly travels the world and has conducted fieldwork in Peru, Antarctica, and Greenland. After graduation she plans to figure out how to save the glaciers and otherwise continue contributing to making the world a better place. Jessica Scheick is a candidate for the Doctor of Philosophy degree in Earth and Climate Sciences from the University of Maine in December 2018.